國 立 交 通 大 學

機 械 工 程 學 系

博 士 論 文

平行化耦合氣體放電與氣流模擬的發展與其於含雜質常壓氦氣介電質電漿束模擬應用的研究

Development of Parallel Hybrid Simulation of Gas Discharge and Gas Flow and Its Application in the Modeling of Atmospheric-Pressure Helium Dielectric Barrier Discharge Jet Considering Impurities

研 究 生：林昆模

指導教授：吳宗信　教授

西 元 2012 年 六 月

平行化耦合氣體放電與氣流模擬的發展與其於含雜質常壓氦氣介電質電漿束模擬應用的研究

Development of Parallel Hybrid Simulation of Gas Discharge and Gas Flow and Its Application in the Modeling of Atmospheric-Pressure Helium Dielectric Barrier Discharge Jet Considering Impurities

研 究 生：林昆模　　Student：Kun-Mo Lin

指導教授：吳宗信　　Advisor：Dr. Jong-Shinn Wu

國 立 交 通 大 學

機 械 工 程 學 系

博 士 論 文

A Thesis

Submitted to Department of Mechanical Engineering

National Chiao Tung University

in partial Fulfillment of the Requirements for the Degree of

Doctor of Philosophy in Mechanical Engineering

June 2012

Hsinchu, Taiwan

西元 2012 年六月

平行化耦合氣體放電與氣流模擬的發展與其於含雜質常壓氦氣介電質電漿束模擬應用的研究

學生： 林昆模　　指導教授： 吳宗信 博士

交通大學 機械工程學系

摘要

本論文報告使用平行化耦合氣體放電與氣流模擬的發展與其於含雜質常壓氦氣介電質電漿束模擬應用的研究。其中氣體放電模擬採用流體模型，利用有限體積法離散所有方程式，並使用區域分解法 (domain decomposition) 及訊息傳輸介面 (message passing interface, MPI) 將程式平行化，成功的在分散式記憶體的個人電腦叢集系統中執行程式並且有效地減少運算時間。同時，本文結合前人[Hu *et al.*, 2011]所發展的平行化可壓縮氣流場模擬程式研發出耦合式模擬運算法則進行含雜質常壓氦氣介電質電漿束模擬。電漿流體模型所需要的計算時間通常是模擬常壓介電質電漿束的瓶頸。本文提出多尺度時間法 (temporal multi-scale method, TMSM)，利用電子與重粒子的特徵時間尺度差異特性，進一步有效地縮短包含許多氣體種類的電漿流體模型所需要的計算時間。本論文所完成的工作建立了模擬真實常壓介電質電漿束應用的基礎。

論文的第一章介紹研究背景以及論文回顧，而第二章則是描述使用的數值方法與演算法。第三章使用一維的模擬結果討論雜質對於氦氣常壓介電質電漿束的影響。第四章與第五章則分別介紹二維電漿流體模型程式的發展與使用耦合式演算法模擬常壓介電質電漿束。以下將逐一描述各章的重要內容。

由於常壓氦氣介電質電漿於應用上具有其重要性，本文第三章討論使用一維流體模型模擬得到的結果。文中探討使用氣相色譜法 (gas chromatography) 所量得存在於氦氣(99.99%)內雜質對於電漿的影響，並且發現氦氣內所含的雜質對於

電漿化學有顯著的改變。無論是否考慮雜質，都沒有在最大電流的瞬間觀察到電中性 (quasi-neutral) 的區域。模擬結果顯示無論氦氣內的雜質對電子密度的影響不大。然而原本 He_2^+ 為不含雜質的氦氣電漿中最主要的離子的角色，在含雜質的氦氣電漿中被 N_2^+ 所取代。而在不含雜質的氦氣電漿中最主要的中性氣體 He_2^* 則被含雜質的氦氣電漿中的基態氧原子取代為最主要的中性氣體。文中亦探討不同水氣含量對於氦氣電漿的影響。結果顯示不同水氣含量的氦氣電漿電子密度差異不大。隨著水氣含量的增加，H_2O^+取代 N_2^+成為氦氣電漿中最主要的離子。儘管基態氧原子依舊是最主要的中性氣體，氫原子與氫氧根 (hydroxyl) 的密度隨著水氣含量的增加而急劇增加。雖然氦氣內雜質均為少許 ppm 的含量，模擬的結果顯示雜質的存在對氦氣電漿的重要性。

本文第四章使用有限體基法發展平行化二維電漿流體模型程式及其在分散式記憶體的個人電腦叢集系統上的實作。為探討模擬氦氣介電質電漿的平行效率，吾人使用各種矩陣預處理 (preconditioning) 方法 (如 ASM; additive Swartz method)與矩陣迭代解法 (如 GMRES; generalized minimal residual method) 針對不同型別的統御方程式進行數值實驗，測試使用最多達 128 顆處理器。對於網格數較多的測試問題，在使用 128 顆處理器的情況下幾乎可以得到線性加速的效果。最後，藉由模擬二維真實常壓介電質電漿束的問題說明所發展的程式具備處理包含複雜電漿化學反應之低溫電漿的應用。

為正確地模擬常壓介電質電漿束，本論文第五章提出耦合數值演算法結合電漿流體模型與氣體模型，並且使用兩種方法加速其計算所需的時間。背景氣體與電漿間藉由交換氣流場模擬所得到的穩態解與電漿流體模型所得到平均源項(source terms)的結果來達到結合兩模型的目的。節省整體計算時間的方法包含於電漿流體模型與氣體模型運用平行計算，以及應用於電漿流體模型的多尺度時間法。兩個模型均使用區域分解法 (domain decomposition) 及訊息傳輸介面 (MPI) 將程式平行化並執行於分散式記憶體的個人電腦叢集系統。多尺度時間法利用電子與重粒子的特徵時間尺度差異特性，於求解重粒子連續方程式的每個時間步

(time step)時，僅考慮化學反應而忽略傳輸項；而所忽略的傳輸項將在每隔一定大小的時間步數回補。在研究的範例中使用多尺度時間法模擬常壓介電質電漿可節省 47%的計算時間。文中所提出的耦合數值演算法藉由模擬平板式常壓氦氣介電質電漿束證明其可行性，並且展現第 200 個週期所得到的結果。由結果發現各種氣體密度分布的情形與背景氣流場分佈息息相關，因此凸顯出常壓介電質電漿束的模擬考慮背景流體的重要性。

論文最後歸納本論文主要的發現，並對相關研究未來的工作方向提出建議。

Development of Parallel Hybrid Simulation of Gas Discharge and Gas Flow and Its Application in the Modeling of Atmospheric-Pressure Helium Dielectric Barrier Discharge Jet Considering Impurities

Student: Lin, Kun-Mo Advisor: Dr. Wu, Jong-Shinn

Department of Mechanical Engineering

National Chiao Tung University

Abstract

The development of a hybrid algorithm of plasma fluid model (PFM) and gas flow model (GFM) for simulating the atmospheric-pressure dielectric barrier discharge jet (APDBDJ) is reported in this thesis. The gas discharge is modeled by plasma fluid model, discretized through finite-volume method, and parallelized with domain decomposition using message passing interface (MPI) and employed on distributed-memory PC cluster that reduces runtime significantly. The hybrid numerical algorithm is proposed by combining a previously developed parallelized compressible flow equation solver [Hu *et al.*, 2011] to simulate the helium APDBDJ considering impurities in this thesis. A temporal multi-scale method (TMSM), taking advantage of the difference of characteristic timescale between electron and heavy particles, is proposed to further reduce the runtime of PFM dramatically in simulations involving with a large amount of species. The effort of this thesis establishes the foundation in simulating realistic APDBDJs.

Chapter 1 of the thesis introduces the research background and motivation, and review of previous studies, and Chapter 2 describes the numerical methods and

developed algorithm in detail. The results of one-dimensional simulation considering the impurities on the helium APDBDJ are presented in Chapter. 3. Chapter 4 and 5 depict the development of 2D parallel PFM code and the hybrid numerical algorithm of PFM and GFM for simulating APDBDJ respectively. The major findings of the thesis and some recommendations for future work are summarized in Chapter 6. More details of each chapter from Chapter 3 are described as follows in turn.

In Chapter 3, the effect of helium impurities (trace amounts of O_2, N_2 and H_2O), measured by the gas chromatography, have been explored and found that the discharge chemistry changes dramatically by considering the impurities. Results have found that the discharges with and without impurities have no quasi-neutral region at the instant of maximum current density. Both discharges with and without impurities have similar levels of electron densities; however, N_2^+ is found to be the most dominant ion with considering impurities, instead of He_2^+ in helium discharge without impurities in the breakdown region. In addition, ground-state atomic oxygen is the most dominant neutral species (except the background species) when considering impurities, instead of He_2^* without considering impurities. The influence of different levels of water vapor is also investigated. The electron densities of helium discharges with various levels of water vapor (1, 5 and 10 ppm) remain at essentially the same level as the amount of water vapor changes. However, the H_2O^+ replaces the N_2^+ as the dominant ion as the water vapor increases. Although the ground-state atomic oxygen is still the dominant neutral species, the densities of atomic hydrogen and hydroxyl increase significantly as the water vapor increases. The results show the importance of considering impurities in the helium discharges though the levels of impurities are typical several to tens ppm.

In Chapter 4, the thesis reports the development of a two-dimensional plasma fluid modeling code using the cell-centered finite-volume method and its parallel

implementation on a distributed-memory PC cluster. Parallel performance of simulating helium APDBDJ resulting from using different degrees of overlapping in the additive Schwarz method (ASM) with preconditioned generalized minimal residual method (GMRES) for different modeling equations is investigated for a small and a large test problem, respectively, employing up to 128 processors. For the large test problem, almost linear speedup can be obtained using 128 processors. Finally, a large-scale realistic two-dimensional APDBDJ problem is employed to demonstrate the capability of the developed fluid modeling code for simulating the low temperature plasma with complex chemical reactions.

In Chapter 5, this thesis proposes a hybrid numerical algorithm which couples weakly the PFM and GFM, and two acceleration approaches for simulating the APDBDJ. The weak coupling between gas flow and discharge is introduced by transferring between the results obtained from the steady-state solution of the GFM and cycle-averaged source terms of the PFM respectively. Approaches of reducing the overall runtime include parallel computing of the GFM and the PFM solvers, and employing a TMSM for PFM. Parallel computing of both solvers is realized using the domain decomposition method with message passing interface (MPI) on distributed-memory PC cluster. The TMSM considers only the source and sink terms of chemical reactions by ignoring the transport terms when integrating temporally the continuity equations of heavy species at each time step, and the ignored transport terms are restored only at an interval of several time marching steps. The total reduction of runtime is 47% by applying the TMSM to the example of APDBDJ as presented in this study. Application of the proposed hybrid algorithm is demonstrated by simulating a parallel-plate helium APDBDJ impinging onto a substrate, in which the cycle-averaged properties of the 200^{th} cycle are presented. The distribution patterns of species densities are strongly correlated by the background gas flow

pattern, which shows that consideration of gas flow in APDBDJ simulations is critical.

In Chapter 6, major findings of this thesis are summarized and recommendations for the future work are outlined.

誌　　謝

這是段漫長的道路，感謝路途上陪伴的各位師長、朋友與家人。

學生要感謝論文指導老師 吳宗信教授在學術研究上的指導，以及生活上的關懷。與老師的知識交流實感獲益匪淺，讓學生能順利踏入研究的領域並且於學問上得以精進。內心由衷的感激老師所提供的研究環境，讓昔為機械系熱流背景的我們能夠研習廣泛應用於工業界與半導體製造產業最為關鍵的電漿技術。

感謝口試委員謝曉星教授、劉通敏教授、寇崇善教授、王啟川教授、徐振哲副教授、黃楓南副教授、與劉耀先助理教授對於研究成果與論文撰寫的指導與建議。非常感謝各位老師能夠在百忙之中遠道而至，不吝予以討論並且提供許多寶貴的意見。

在研究的路途上，學生需要特別感謝洪捷粲博士。洪博士對於電漿物理與數值模擬細膩精闢的見解與扎實的實作基礎所提供許多具建設性的意見，是學生能夠在最短時間內發展程式的重要關鍵。另外也要感謝即將畢業的邱沅明博士所發展功能強大完善兼備許多功能的化學模組，縮短學生發展程式所需要的時間。還要感謝也是即將畢業的胡孟樺博士所發展可適用於可壓縮和不可壓縮熱流場程式所得到的許多結果，用以討論熱流場對於大氣電漿束應用的耦合現象。

還要感謝參與實驗量測的學弟宜偉、志東、育安、志華、國淳、駿平，謝謝你們對於實驗資料的協助。

感謝這段時間與學生陪伴成長的雅茹、即將畢業的鄭凱文博士、正勤、穎志、俊傑、逸民、其璋、皓遠、志良、子豪、古必、冠融、垂青、芳安、明忠、仁寶、世昕、不讀 paper 的康旻、易軒、哲緯。希望已經畢業的各位事業順利，尚未畢業的諸位順利通過考驗。

最後僅將本文獻給親愛的家人，沒有你們的支持我做不到。謝謝小女筠茜總是在工作忙碌的時候調皮搗蛋。謝謝儘量少抱怨的老婆郡瑛，總是默默的度過許多看電視的周末。你們的鼓勵是我前進最重要的動力。

Table of Contents

List of Tables

List of Figures

Nomenclature

m	mass
P	pressure
q	charge
k_B	Boltzmann constant
n	number density
Γ	particle flux
v_{th}	thermal velocity
γ	factor of secondary electron emission
S	source/sink of continuity equation
T_e	electron temperature
ε	energy loss for inelastic electron collision
ϕ	potential
ε_0	vacuum permittivity
ε_d	dielectric permittivity
E	electric field
f	electron energy distribution function
k	reaction rate coefficient
μ	mobility
D	diffusivity
ν_m	momentum exchange collision frequency between electron and background neutral particles
Δx	space interval in x direction
Δy	space interval in y direction

Δt	time interval
B	Bernoulli function

Chapter 1 Introduction

1.1 Classification of Plasmas

Plasma is generally considered as the fourth state of matter with the collective behavior of charged and neutral particles. Specifically, plasmas are a collection of quasi-neutral particles containing charged and neutral particles in the form of gaseous or fluid-like mixtures. The plasma state can be produced by heating the substance to the temperature high enough to ionize the neutral atoms, or it can be created by applying the sufficiently high electric field to cause ionizations by energetic free electrons absorbing the electric energy from the applied external electric field.

The scales of plasmas observed may be as huge as the intergalactic nebula of cosmic plasmas, or plasmas can be generated in the small devices such as the microplasmas with their scale down to few mm in the laboratory [1]. The plasmas found cover a wide range of electron densities and temperatures as shown in Fig. 1-1 [2]. The plasma density can be as low as 10^4 cm^{-3} as that of ionosphere, which stretches from a height of about 50 km to more than 1,000 km of earth's surface, and the plasma density can be as high as 10^{18} cm^{-3} for the thermonuclear reactors. The energy level of electron temperature varies from 0.1 eV of ionosphere to more than 10^4 eV in the thermonuclear reactors.

Plasmas are frequently classified as low- (LTP) and high-temperature plasmas (HTP) as shown in Table 1-1 [3]. The HTP (for example, fusion plasmas) are in their thermal equilibrium, meaning that the temperature of ions is about equal to that of electrons, with the temperature is up to 10^7 K. The LTP can be subdivided into states in thermal equilibrium and non-thermal equilibrium. The LTP in thermal equilibrium (or thermal LTP) are produced mostly in atmospheric pressure with their temperature

of ions, electrons and neutrals are at the level of 10^4 K. The thermal LTP, such as arc plasmas and plasma torches, are used in welding, cutting hard materials, and material processing like melting and dissociation of minerals in industries [4]. For LTP with the thermal equilibrium not reached between the electrons and the heavy particles (ions and neutrals) are classified as non-thermal LTP. The temperature of heavy particles of non-thermal LTP is typically close to room temperature, whereas the electron temperature is much greater than that of heavy particles and is as high as 10^4 ~ 10^5 K. The non-thermal LTPs are especially important for the industrial applications because the low temperature of heavy particles has no (or tolerable) damage on the materials and the electron temperature is high enough to generate essential reactive species for applications. The non-thermal LTP contribute much to the major processes of microelectronics fabrication such as sputtering; plasma enhanced chemical vapor deposition, plasma etching, ashing, implantation, and surface cleaning. Besides, the non-thermal LTP can also be used for surface modification to improve the surface properties, such as the hardness, resistance of corrosion, dielectric properties of materials, without changing the bulk properties because of the low temperature of heavy particles. Recently, the non-thermal LTP have also been used for many biomedical applications such as sterilization, bio-compatibility of materials, and wound healing as a promising enabling technology [5].

1.2 Non-Thermal Low Temperature Plasmas (LTP)

Non-thermal LTP can be further classified using the frequency of applied power as direct current (DC) discharges, dielectric-barrier discharges (DBD), radio frequency (RF) discharges, and microwave frequency discharges. Each type of discharge is introduced next in turn.

1.2.1 Direct Current Discharges

The DC discharges are the backbone for understanding the discharge characteristics of different types of non-thermal LTP because the well understood behaviors of DC discharges have been used as analogies for different types of non-thermal LTP. A DC discharge is produced by applying a DC voltage across the parallel-plate system in the low-pressure gas as shown in Fig. 1-2 [2]. The sustaining glow discharge is controlled by the emission of secondary electrons generated mainly by ion impact on the cathode. The structure of DC discharge is characterized with distinct regions exhibiting several bright and dark regions along the discharge tube as shown in Fig. 1-3 [6]. The structures such as negative glow, Faraday dark space, and positive column are usually taken as the analogies to analyze different types of discharges. Details of both bright and dark regions are explained by the variation of electron temperature, electron density, and potential. Fig. 1-4 [2] shows a typical I-V characteristic of a DC discharge. The DC discharge can be operated from the Townsend discharge, characterized by very low current and very high voltage, to the thermal arc discharge results from the thermionic emission.

1.2.2 Dielectric-Barrier Discharges (DBD)

The DBD are generated by using two electrodes of which at least one is covered by a dielectric material. The DBD have been known for more than a century since reported by Siemens (in 1857) concentrating on the generation of ozone [7]. The presence of dielectric serves as the current limiter to avoid formation of sparks and current growth. The typical frequency of applied power of DBD is in the range of 1 ~ 100 KHz. Fig. 1-5 [8] shows various types of arrangement of the DBD. The important advantages of the DBD include the simplicity of their arrangements, stable operation conditions, and scalability from small laboratory reactors to large industrial

installations.

1.2.3 Radio Frequency (RF) Discharges

The RF power can interact with plasmas either inductively or capacitively as shown in Fig. 1-6 [2][9]. The frequency of RF discharges ranges from 1 ~ 100 MHz. Both positive and negative charges are retained between electrodes in the RF discharges rather than quenched at the electrodes as that of DC discharges; therefore, the RF discharges require less breakdown voltage as compared to the DC discharges. RF discharges can be sustained with internal and external electrodes, which is important for some cases with corrosive gases or to reduce contamination of the plasmas with the material of the electrodes, whereas DC discharges require the electrodes to be placed inside the reactor because of the generation of secondary electron emission which is an important factor to sustain the DC discharges. In RF plasmas, the energy of ion bombardment on the substrate can be controlled by another external bias, whereas the DC discharge are exposed to the bombardment of high-energy ions that are accelerated at voltages across the cathode fall leading to the damage on the sensitive substrates. The RF discharges are successfully applied to thin film deposition and etching as well as to the sputtering of insulating materials. A matching box is required to adjust the impedance of the plasma reactor for higher efficiency of power transferred to the discharge.

1.2.4 Microwave Discharges

Microwave discharges are sustained by applied power operating in the range of 300 MHz ~ 10 GHz. The excitation of microwave discharges is similar to the excitation of RF discharges. Microwaves are easily absorbed or reflected by most materials and can not be transmitted by cables without significant losses. The applied

microwave transmits in the waveguide with proper design. The microwave discharges generate usually higher density of plasma than that of RF discharges. However, the wavelength of applied electric power shortens as the frequency increases, which causes to the standing wave problem leading to the serious uniformity issue in practical applications.

Many applications of non-thermal LTP, especially in semiconductor fabrication industry, are operated at low pressure for reasons such as to reduce the contaminant of impurities or to eliminate the disturbance of impurities during operation (for example, etching and deposition). Recently, the atmospheric-pressure (AP) non-thermal LTP attract tremendous attention because they do not require the expensive vacuum system for applications, for example, ozone production, pollution control, surface modification, sterilization, and wound healing [5][7] which are less sensitive to the impurities of background gases. Among the sources of non-thermal LTP previously introduced, APDBDJ have been used popularly because of: 1) low cost due to no need of the expensive vacuum pumping system, 2) its simple implementation and stable operation conditions, and 3) being a stand-alone module. In this thesis, we are interested in investigating helium APDBDJ numerically and its importance is introduced next.

1.3 Importance of Helium Discharges

Many gases (argon, helium, nitrogen, oxygen, air, etc.) have been used as the working gas to generate discharges. Among these working gases, helium is a commonly selected and studied as the working gas for the APDBDJ because it can be operated in a wide stable operating window at atmospheric pressure [10]. Moreover, helium discharges with addition of other gases for specific purposes are not uncommon for applications. For example, oxygen (up to ~ 2%) are widely added in

the helium discharges to generate the oxygen reactive species such as O, O*, and O_2* which are believed that those species are important for applications like etching [11], surface modification [12][13], surface cleaning [14], and sterilization [15], among others. Therefore, this thesis focuses on the fundamental study of helium APDBDJ.

1.4 Numerical Simulation of Gas Discharges

Despite the gas discharges are the promising technology adopted in many modern applications, the underlying physics and chemistry of many practical discharges have not been understood thoroughly due to their complexity. The design of these discharge devices and process controls of manufacturing mainly depends on time-consuming and expensive trial-and-error approach, which is economically inefficient. It may be limited and difficult, if possible, to comprehend completely these complex physics and chemistry associated with the discharges through the experimental methods. Therefore, numerical simulation provides an alternative approach in revealing the complex physics and chemistry of discharges.

Two major approaches, Particle-in-Cell with Monte-Carlo collision (PIC/MCC) and plasma fluid modeling (PFM hereafter), have been widely used for low-temperature discharge simulations. Although the PIC/MCC approach solves the Boltzmann equation directly and statistically, it is very time-consuming for higher pressure condition because of large amount of pseudo particles is needed for obtaining an accurate solution. PFM, which assumes the plasma as a continuum, is often employed to model gas discharges and requires less computational time than the PIC/MCC approach, should the pressure be not too low. Nevertheless, the applications accompanied with large-scale (computational) domain and/or complex chemistry (species and reactions), which is not uncommon in practice, could lead to unacceptable computational time even using PFM. Acceleration of the fluid modeling

is thus strongly required in simulating realistic gas discharges. Fortunately, this difficulty can be resolved by the rapid advance in computer hardware and the development on the parallel computing. The implementation of parallel computing is capable of reducing the runtime dramatically as discussed in this thesis.

1.5 Literature Survey

1.5.1 Simulation of Helium Discharges with Impurities

APDBDJ with pure helium has been studied for a long time. However, it is very difficult to conduct the experiment with 100 % pure helium because of the limit of industrial production. Different grades of helium gas may be used to conduct the experiments by different research groups. It was shown that discharge current calculated from pure helium data does not quantitatively agree with experimental results [16]. Although the impurity level is typically less than 0.01 %, it was reported that the impurity plays an important role in "pure" helium discharges [16]-[20]. Effect of impurity was generally modeled with nitrogen because of good agreement with experimental results under reasonable level of impurity (~100 ppm). The simulation indicates that metastable helium atoms generated during a discharge breakdown contribute significantly to the pre-ionization of the gas before the next breakdown through Penning ionization of nitrogen impurity.

Although the importance of impurity in the helium APDBDJ has been noticed, there is no report focusing on the study of realistic composition of helium impurities. The existence of impurities change the discharge species chemistry significantly as presented later (Chapter 3) though the impurity level is as low as several to tens ppm for high grade helium gas. Practically, it is important to realize the detailed species of discharge chemistry for deducing the correct conclusion from the experimental observation of applications; therefore, the difference between helium discharge with

and without the realistic impurities is discussed in this thesis.

1.5.2 Parallel Computing of Fluid Modeling

One-dimensional plasma fluid model is a good tool to investigate the temporal and spatial variations of plasma physics and chemistry for a homogeneous discharge. However, one-dimensional simulations are not capable of revealing the species distributions associated with the flow dynamics in the discharge and afterglow region which determines the effect of discharge treatment for applications. This difficulty can be resolved by using two-dimensional simulations for most of the applications if the discharge behavior can be simplified as two-dimensional planar or axisymmetric simulations.

Fluid modeling generally requires less computational time as compared to PIC/MCC approach. Nevertheless, it is still an issue for large-scale two-dimensional problems with many species and complex chemistry, which could lead to unacceptable computational time. Fortunately, the development of parallel computing has been proved to be able to reduce effectively the computational runtime dramatically for simulations. Recently, a representative plasma simulation package *Plasimo* using the finite-volume method, developed by van Dijk *et al.* [21], has been demonstrated as a parallel version using symmetric multi-processing (SMP) with OpenMP protocol. However, OpenMP allows only data to be shared within a single node with multi-processor, which limits the problem size or chemistry complexity of simulations. To speed up the computation of large-scale plasma fluid modeling, parallel computing using very popular distributed memory machines with message passing interface (MPI) is required.

In the past, there are very few studies focusing on parallel implementation of low-temperature plasma fluid modeling on distributed memory machines, albeit the

importance of reduced computational time cannot be overemphasized for practical applications. Among the very few, the parallel fully implicit Newton-Krylov-Schwarz (NKS) algorithm was employed to solve the coupled large sparse, algebraic nonlinear system of the discrete governing equations of fluid modeling derived from the fully implicit scheme [22]-[23]. Although the speedup of parallel computing is scalable up to hundreds of processors, the overall computational time is too large for realistic large-scale multidimensional problems. This obstacle could be overcome by the so-called semi-implicit method, which solves the fluid modeling equations independently with proper linearization of the source terms of the Poisson equation [24] and the electron energy density equation [25]. In this approach, the coupled nonlinear system of plasma fluid modeling equations become linear and decoupled so that they can be solved sequentially. It was shown that much larger time step could be employed to greatly shorten the computational time in sequential implementation.

Thus, one of the major objectives of this thesis is to develop a parallel two-dimensional plasma fluid modeling code using the cell-centered finite-volume method with the semi-implicit approach. The resulting linear systems of discretized equations are solved by the parallel generalized minimal residual method (GMRES) [26] in conjunction with the parallel additive Schwarz method (ASM) [27] as the preconditioner to accelerate its convergence. The Schwarz type methods have been proved to be theoretically optimal for many types of problems, and practically powerful for solving large problems on computers with thousands of processors. The preconditioner is decomposed into several sub-domains by domain decomposition for parallel computing. The computational time could be dramatically reduced with the combination of preconditioning and linear matrix solvers for various modeling equations as presented in Chapter 4.

1.5.3 Parallel Hybrid Numerical Algorithm for Simulating APPJ

Gas discharge simulation considering diffusion without convection for heavy species (i.e., ignoring fluid dynamics effect) is considered to be valid at the low-pressure condition. However, fluid dynamics is expected to have a strong impact on the gas discharge at high pressure condition such as the atmospheric-pressure plasma jet (APPJ). Thus, it is necessary to properly model and integrate the gas flow and gas discharge simultaneously for a better understanding the APPJ. However, it is found that only very few studies in the literature have focused on this subject [21][28][29]. This is mainly because that a complete simulation of the APPJ coupling the fluid dynamics and gas discharge often takes from weeks up to months of runtime. Specifically speaking, simulation of gas discharge often takes generally about 90% of the overall runtime for the simulation of the APPJ because of the very small time step limited by the very light electron. In other words, the bottleneck for speeding up the APPJ simulation is to shorten the runtime consumed by the modeling of gas discharge.

For the PFM employed in this study, the evolution of gas discharge is modeled by the self-consistent solution of the Poisson equation, the charged and neutral species continuity equations, and the electron energy density equation. It is known that electrons respond extremely fast to the temporal variation of the electric field, leading to very large transport properties (i.e., mobility and diffusivity), whereas ions respond relatively slow to the temporal variation of the electric field. The neutrals transported by diffusion are even slower if compared with the drift of charged species induced by the electric field. The time step size used in solving the PFM is generally constrained by the electron motion, in the order of 10^{-10} seconds, and must be small enough to resolve the electron dynamics for a faithful simulation of gas discharge. This leads to the possibility of neglecting the transport of heavy species as compared to chemical

reaction at each time step without losing numerical accuracy of the simulation. Realization of this concept can further shorten the runtime for solving the PFM by using the temporal multi-scale method (TMSM) as presented in Chapter 5.

1.6 Objectives and Organization of This Thesis

The major objective of this thesis is to develop an efficient hybrid numerical algorithm to couple the PFM and GFM utilizing parallel computing for simulating the helium APDBDJ with impurities. To achieve this objective, several specific goals are summarized as follows:

1. To study the impact on chemistry of the helium APDBDJ with and without impurities by one-dimensional fluid modeling;
2. To develop a parallel semi-implicit two-dimensional plasma fluid modeling code using finite-volume method;
3. To develop a hybrid numerical algorithm to simulating gas flow and gas discharge of the APPJ.

The thesis is organized as follows:

Chapter 2 describes the modeling and numerical method developed in this thesis including the governing equations of PFM and GFM, discretization of equations, the hybrid algorithm for coupling the PFM and GFM solvers, and the development of TMSM for PFM.

Chapter 3 studies the helium APDBDJ with and without considering impurities simulated by one-dimensional PFM. The distribution of species of helium APDBDJ with and without considering impurities are compared, and the reaction paths for generating dominant species are presented and discussed. The effect of different levels of water vapor as impurities is also presented and discussed at the end of this chapter.

Chapter 4 investigates the parallel performance of the developed PFM code

through a small and a large problem with the configuration of numerical domain and size equivalent to the experimental setup performed by our group. The detailed performance of different types of equations is discussed, and a demonstration of helium APDBDJ without including the flow dynamics is given at the end of this chapter.

Chapter 5 addresses on the development of an efficient hybrid numerical algorithm to couple the developed PFM and GFM solvers for simulating a realistic parallel-plate APDBDJ. It is shown that the runtime of PFM can be reduced tremendously for the problem tested using the proposed TMSM. The cycle-averaged species distributions at 200^{th} cycle are presented which shows that it is important to consider fluid dynamics for the APPJ simulation.

Chapter 6 concludes by summarizing the major findings found in this thesis and outlining the recommendations for the future work.

Fig. 1-7 shows the research structure of the thesis.

Chapter 2 Modeling and Numerical Methods

2.1 Governing Equations of Fluid Modeling

Fluid modeling is suitable for low-temperature plasmas in a wide range of pressures (from low pressure to atmospheric pressure). Generally, there are two types of approximations used in the fluid modeling: 1) local field approximation (LFA) and 2) local-mean-energy approximation (LMEA). The former assumes the locally absorbed electric power is fully balanced by the power dissipated through ionization, while the latter solves the electron energy density equation to obtain the electron temperature which is related to the evaluation of reaction rate constants and other transport properties associated with electrons. LMEA has been shown to be more accurate than LFA in fluid modeling of low-pressure gas discharges [30]. For wider future applications, the LMEA is adopted in the current study to consider non-local effect of electron energy distribution that LFA generally lacks. The governing equations of fluid modeling with LMEA include the continuity equations of each species, the Poisson equation for calculating the electric field, and the electron energy density equation for evaluating the electron temperature subject to the non-local effect of electron kinetic energy.

The general continuity equation for ion species can be written as

$$\frac{\partial n_p}{\partial t} + \vec{\nabla} \cdot \vec{\Gamma}_p = \sum_{i=1}^{r_p} S_{p_i} \qquad p=1,\ldots,K \tag{2-1}$$

where n_p is the number density of ion species p, K is the number of ion species, r_p is the number of reaction channels that involve the creation and destruction of ion species p and $\vec{\Gamma}_p$ is the particle flux that is expressed, based on the drift-diffusion approximation, as

$$\vec{\Gamma}_p = sign(q_p)\mu_p n_p \vec{E} - D_p \vec{\nabla} n_p \tag{2-2}$$

$$\vec{E} = -\vec{\nabla}\phi \tag{2-3}$$

where q_p, $\vec{E}$, ϕ, μ_p, and D_p are the ion charge, the electric field, the electric potential, the ion mobility, and the ion diffusivity respectively. Note that the form of the source term S_{p_i} can be modified according to the modeled reactions describing how the ion species *p* is generated or destroyed in reaction channel *i*.

The continuity equation for electron species can be written as

$$\frac{\partial n_e}{\partial t} + \vec{\nabla} \cdot \vec{\Gamma}_e = \sum_{i=1}^{r_e} S_{e_i} \tag{2-4}$$

where n_e is the number density of electrons, r_e is the number of reaction channels that involve the creation and destruction of electrons and $\vec{\Gamma}_e$ is the corresponding particle flux that is expressed, based on the drift-diffusion approximation, as

$$\vec{\Gamma}_e = -\mu_e n_e \vec{E} - D_e \vec{\nabla} n_e \tag{2-5}$$

where μ_e and D_e are the electron mobility and electron diffusivity, respectively. These two transport coefficients can be readily obtained as a function of the electron temperature from the solution of a publicly available computer code for the Boltzmann equation, named BOLSIG$^+$ [31]. Similar to S_{P_i}, the form of S_{e_i} can also be modified according to the modeled reactions that generate or destroy the electron in reaction channel *i*.

The continuity equation for neutral species can be written as

$$\frac{\partial n_{uc}}{\partial t} + \vec{\nabla} \cdot \vec{\Gamma}_{uc} = \sum_{i=1}^{r_{uc}} S_{uc_i} \qquad uc=1,\ldots,L \tag{2-6}$$

where n_{uc} is the number density of uncharged neutral species *uc*, *L* is the number of neutral species, r_{uc} is the number of reaction channels that involve the generation

and destruction of uncharged species *uc* and $\vec{\Gamma}_{uc}$ is the corresponding particle flux which can be expressed as

$$\vec{\Gamma}_{uc} = -D_{uc}\vec{\nabla}n_{uc} \tag{2-7}$$

where D_{uc} is the diffusivity of neutral species. It is noted that the convective effect is neglected in this study. Similarly, the form of S_{uc_i} can also be modified according to the modeled reactions that generate or destroy the neutral species in reaction channel *i*.

The electron energy density equation can be expressed as

$$\frac{\partial n_\varepsilon}{\partial t} + \vec{\nabla}\cdot\vec{\Gamma}_{n_\varepsilon} = -e\vec{\Gamma}_e\cdot\vec{E} - \sum_{i=1}^{S_c}\varepsilon_i k_i n_i n_e - 3\frac{m_e}{M}n_e k_B \nu_m\left(T_e - T_g\right) \tag{2-8}$$

where $n_\varepsilon\left(=\frac{3}{2}n_e k_B T_e\right)$ is the electron energy density, T_e is the electron temperature, ε_i and k_i are the energy loss and rate constant for the i^{th} inelastic electron collision respectively, n_i is the number density of species related to the i^{th} inelastic electron collision, S_c is the number of reaction channels of inelastic electron collision, k_B is the Boltzmann constant, ν_m is the momentum exchange collision frequency between the electron (mass m_e) and the background neutral (mass M), T_g is the background gas temperature. $\vec{\Gamma}_{n_\varepsilon}$ is the corresponding electron energy density flux and can be expressed as

$$\vec{\Gamma}_{n_\varepsilon} = \frac{5}{2}k_B T_e\vec{\Gamma}_e - \frac{5}{2}D_e n_e\vec{\nabla}\left(k_B T_e\right) \tag{2-9}$$

The second term on the right-hand side of Eq. (2-8) represents the sum of the energy losses of the electrons due to inelastic collision with other species. The last term on the right-hand side of Eq. (2-8) can be ignored for low-pressure gas discharges, while it is important for medium-to-atmospheric pressure discharges.

The Poisson equation for electrostatic potential can be expressed as

$$\vec{\nabla}\cdot(\varepsilon\vec{\nabla}\phi) = -\sum_{i=1}^{K}(qn)_i \tag{2-10}$$

where ϕ is the potential, K is the total number of charged species and the permittivity ε, is a function of position, is written as

$$\varepsilon = \varepsilon_r \varepsilon_0 \tag{2-11}$$

where ε_0 is the vacuum permittivity, and ε_r is the relative permittivity of each region. Several different regions including discharge, dielectric materials (such as alumina, substrate, and Teflon), and conductors are considered simultaneously in this study. All of these regions are meshed and solved to obtain the electrostatic potential distribution by using the Poisson equation.

2.2 Boundary Conditions

The flux-type boundary conditions for the ions, electrons, and neutral species are employed on the solid surfaces (dielectric or electrode) as

$$\vec{\Gamma}_p = a\cdot sign(q_p)\mu_p n_p \vec{E} - D_p\vec{\nabla}n_p \tag{2-12}$$

$$\vec{\Gamma}_e = -a\cdot\mu_e n_e \vec{E} - D_e\vec{\nabla}n_e + \frac{1}{4}n_e v_{th} \tag{2-13}$$

$$\vec{\Gamma}_{uc} = -D_{uc}\vec{\nabla}n_{uc} \tag{2-14}$$

where $a=1$ if drift velocity ($sign(q_p)\mu_p\vec{E}$) points toward the dielectric surface, and $a=0$ otherwise. We assume that the ions and electrons accumulate and the neutral species quench at the dielectric surface in the present study. The thermal velocity of electron is

$$v_{th} = \sqrt{\frac{8k_B T_e}{\pi m_e}} \tag{2-15}$$

where m_e is the electron mass. Note that the effect of secondary electron emission is neglected. For all species, the fluxes at the boundaries of computational domain

(except the dielectric surfaces) are assumed to be zero.

The boundary conditions of electron energy density flux at the dielectric surfaces are

$$\vec{\Gamma}_{n_\varepsilon} = 2k_B T_e \vec{\Gamma}_e \tag{2-16}$$

For the Poisson equation, the potentials of powered and grounded electrode are assigned with applied voltage and zero potential respectively. Neumann boundary conditions with zero gradients are applied to the other boundaries of the computational domain for the Poisson equation.

2.3 Implementation of Semi-Implicit Schemes

It was reported that explicit evaluation of the source term of the Poisson equation leads to a very small time step due to the restriction of dielectric relaxation time [24]. The so-called semi-implicit treatment is thus applied on the source term of the Poisson equation to expand the time step by a Taylor's series expansion (TSE) in time. With some derivations based on a TSE in time and approximations, the Poisson equation, Eq. (2-10), can be rewritten as

$$\vec{\nabla} \cdot \left[\left(\varepsilon + \Delta t \sum_{i=1}^{K} \left(|q| \mu n \right)_i \right) \vec{\nabla} \phi \right] = -\sum_{i=1}^{K} q_i n_i \tag{2-17}$$

Note the number densities and mobilities of semi-implicit term in equation (2-17) are approximated from the values of previous time level. Similar constraint on time step size can be found on the source term of the electron energy density equation, Eq. (2-8), and the energy source term is linearized by a TSE in electron energy with some approximations for increasing the time step size of the simulation [25]. Thus, the electron energy density equation can be rewritten as

$$\frac{\partial n_\varepsilon}{\partial t}+\vec{\nabla}\cdot\vec{\Gamma}_{n_\varepsilon}=-e\vec{\Gamma}_e\cdot\vec{E}-n_e\sum_{i=1}^{s_c}\varepsilon_i k_i n_i-3\frac{m_e}{M}n_e k_B v_m\left(T_e-T_g\right)$$
$$-\left[\frac{e}{n_e}\vec{E}\cdot\frac{\partial\vec{\Gamma}_e}{\partial\mu_e}\frac{\partial\mu_e}{\partial\bar{\varepsilon}}+\frac{e}{n_e}\vec{E}\cdot\frac{\partial\vec{\Gamma}_e}{\partial D_e}\frac{\partial D_e}{\partial\bar{\varepsilon}}+\sum_{i=1}^{s_c}\varepsilon_i\frac{\partial k_i}{\partial\bar{\varepsilon}}n_i+3\frac{m_e}{M}k_B\frac{\partial v_m}{\partial\bar{\varepsilon}}\left(T_e-T_g\right)\right]\left(n_\varepsilon-n_e\bar{\varepsilon}\right) \quad (2\text{-}18)$$

where $\bar{\varepsilon}=3/2\,k_B T_e$. The discretization form of $\frac{\partial\vec{\Gamma}_e}{\partial\mu_e}\frac{\partial\mu_e}{\partial\bar{\varepsilon}}+\frac{\partial\vec{\Gamma}_e}{\partial D_e}\frac{\partial D_e}{\partial\bar{\varepsilon}}$ has been derived by Hagelaar *et al.* [25], and the finite difference method is applied to evaluate $\frac{\partial k_i}{\partial\bar{\varepsilon}}$ and $\frac{\partial v_m}{\partial\bar{\varepsilon}}$. Details of the implementation can be found in references [24][25], and are not described here for brevity.

2.4 Discretization and Numerical Schemes

In the present study, the above equations are discretized using the collocated cell-centered finite-volume method [32] as

$$\frac{\partial\eta}{\partial t}+\frac{F_{i+1/2,j}-F_{i-1/2,j}}{\Delta x_{i,j}}+\frac{G_{i,j+1/2}-G_{i,j-1/2}}{\Delta y_{i,j}}=S_{i,j} \quad (2\text{-}19)$$

with $\eta=\begin{bmatrix}n_p\\ n_e\\ n_{uc}\\ n_\varepsilon\\ 0\end{bmatrix}_{i,j}$, $F=\begin{bmatrix}\Gamma_p\\ \Gamma_e\\ \Gamma_{uc}\\ \Gamma_\varepsilon\\ \Gamma_\phi\end{bmatrix}_x$, $G=\begin{bmatrix}\Gamma_p\\ \Gamma_e\\ \Gamma_{uc}\\ \Gamma_\varepsilon\\ \Gamma_\phi\end{bmatrix}_y$, $S=\begin{bmatrix}S_p\\ S_e\\ S_{uc}\\ S_\varepsilon\\ S_\phi\end{bmatrix}_{i,j}$

where the subscripts *i* and *j* represent the indices of cell in x- and y-direction respectively. For simplicity of presentation, the rectangular computational domain is assumed and a set of regular grids is considered. Δx and Δy are the cell width in x- and y-direction respectively. The fluxes in the continuity equations and the electron energy density equation are calculated with the Scharfetter–Gummel (SG) scheme [33]. After the backward Euler method is employed as a time-integrator, the discretized form of continuity equation can be written as

$$\frac{n_{i,j}^{k+1}-n_{i,j}^{k}}{\Delta t}+\frac{\Gamma_{i+1/2,j}^{k+1}-\Gamma_{i-1/2,j}^{k+1}}{\Delta x_{i,j}}+\frac{\Gamma_{i,j+1/2}^{k+1}-\Gamma_{i,j-1/2}^{k+1}}{\Delta y_{i,j}}=S_{i,j}^{k} \quad (2\text{-}20)$$

with

$$\Gamma^{k+1}_{i+1/2,j} = -\frac{D^k_{i+1/2,j}}{x_{i+1,j}-x_{i,j}}\left[B\left(-X_{i+1/2,j}\right)n^{k+1}_{i+1,j} - B\left(X_{i+1/2,j}\right)n^{k+1}_{i,j}\right] \qquad X_{i+1/2,j} = \frac{sign(q)\mu^k_{i+1/2,j}}{D^k_{i+1/2,j}}\left(\phi_{i+1,j}-\phi_{i,j}\right)^{k+1}$$

$$\Gamma^{k+1}_{i-1/2,j} = -\frac{D^k_{i-1/2,j}}{x_{i,j}-x_{i-1,j}}\left[B\left(-X_{i-1/2,j}\right)n^{k+1}_{i,j} - B\left(X_{i-1/2,j}\right)n^{k+1}_{i-1,j}\right] \qquad X_{i-1/2,j} = \frac{sign(q)\mu^k_{i-1/2,j}}{D^k_{i-1/2,j}}\left(\phi_{i,j}-\phi_{i-1,j}\right)^{k+1}$$

$$\Gamma^{k+1}_{i,j+1/2} = -\frac{D^k_{i,j+1/2}}{y_{i,j+1}-y_{i,j}}\left[B\left(-X_{i,j+1/2}\right)n^{k+1}_{i,j+1} - B\left(X_{i,j+1/2}\right)n^{k+1}_{i,j}\right] \qquad X_{i,j+1/2} = \frac{sign(q)\mu^k_{i,j+1/2}}{D^k_{i,j+1/2}}\left(\phi_{i,j+1}-\phi_{i,j}\right)^{k+1}$$

$$\Gamma^{k+1}_{i,j-1/2} = -\frac{D^k_{i,j-1/2}}{y_{i,j}-y_{i,j-1}}\left[B\left(-X_{i,j-1/2}\right)n^{k+1}_{i,j} - B\left(X_{i,j-1/2}\right)n^{k+1}_{i,j-1}\right] \qquad X_{i,j-1/2} = \frac{sign(q)\mu^k_{i,j-1/2}}{D^k_{i,j-1/2}}\left(\phi_{i,j}-\phi_{i,j-1}\right)^{k+1}$$

where the superscripts *k* and *k+1* represent properties of the previous and current time levels respectively and the Bernoulli function $B(X) = \frac{X}{e^X - 1}$.

Similarly, the discretized form of electron energy density equation (2-8) can be written as

$$\frac{n^{k+1}_{\varepsilon(i,j)} - n^k_{\varepsilon(i,j)}}{\Delta t} + \frac{\Gamma^{k+1}_{\varepsilon\left(i+1/2,j\right)} - \Gamma^{k+1}_{\varepsilon\left(i-1/2,j\right)}}{\Delta x_{i,j}} + \frac{\Gamma^{k+1}_{\varepsilon\left(i,j+1/2\right)} - \Gamma^{k+1}_{\varepsilon\left(i,j-1/2\right)}}{\Delta y_{i,j}} = S^k_{\varepsilon(i,j)} \qquad (2\text{-}21)$$

with

$$\Gamma^{k+1}_{\varepsilon\left(i+1/2,j\right)} = -\frac{5}{3}\frac{D^k_{i+1/2,j}}{x_{i+1,j}-x_{i,j}}\left[B\left(-X_{i+1/2,j}\right)n^{k+1}_{\varepsilon(i+1,j)} - B\left(X_{i+1/2,j}\right)n^{k+1}_{\varepsilon(i,j)}\right]$$

$$\Gamma^{k+1}_{\varepsilon\left(i-1/2,j\right)} = -\frac{5}{3}\frac{D^k_{i-1/2,j}}{x_{i,j}-x_{i-1,j}}\left[B\left(-X_{i-1/2,j}\right)n^{k+1}_{\varepsilon(i,j)} - B\left(X_{i-1/2,j}\right)n^{k+1}_{\varepsilon(i-1,j)}\right]$$

$$\Gamma^{k+1}_{\varepsilon\left(i,j+1/2\right)} = -\frac{5}{3}\frac{D^k_{i,j+1/2}}{y_{i,j+1}-y_{i,j}}\left[B\left(-X_{i,j+1/2}\right)n^{k+1}_{\varepsilon(i,j+1)} - B\left(X_{i,j+1/2}\right)n^{k+1}_{\varepsilon(i,j)}\right]$$

$$\Gamma^{k+1}_{\varepsilon\left(i,j-1/2\right)} = -\frac{5}{3}\frac{D^k_{i,j-1/2}}{y_{i,j}-y_{i,j-1}}\left[B\left(-X_{i,j-1/2}\right)n^{k+1}_{\varepsilon(i,j)} - B\left(X_{i,j-1/2}\right)n^{k+1}_{\varepsilon(i,j-1)}\right]$$

$$S^k_{\varepsilon(i,j)} = -e\vec{\Gamma}_e \cdot \vec{E} - \sum_{m=1}^{S_e}\varepsilon_m k^k_{m(i,j)} n^k_{m(i,j)} n^k_{e(i,j)} + 3\frac{m}{M}n_e\nu_m\left(T^k_{e(i,j)} - T_{g(i,j)}\right)$$

$$= -e\left(\Gamma^k_{e,x(i,j)} \cdot E^k_{x(i,j)} + \Gamma^k_{e,y(i,j)} \cdot E^k_{y(i,j)}\right) - \sum_{m=1}^{S_e}\varepsilon_m k^k_{m(i,j)} n^k_{m(i,j)} n^k_{e(i,j)} + 3\frac{m}{M}\left(n_e\nu_m\right)^k\left(T^k_{e(i,j)} - T_{g(i,j)}\right)$$

The Poisson equation (2-10) is discretized in a similar method as

$$\frac{1}{\Delta x_{i,j}}\left[\frac{\varepsilon'_{i,j}\varepsilon'_{i+1,j}}{\varepsilon'_{i,j}\Delta h_{x(i+1,j)}+\varepsilon'_{i+1,j}\Delta h_{x(i,j)}}\left(\phi^{k+1}_{i+1,j}-\phi^{k+1}_{i,j}\right)-\frac{\varepsilon'_{i-1,j}\varepsilon'_{i,j}}{\varepsilon'_{i-1,j}\Delta h_{x(i,j)}+\varepsilon'_{i,j}\Delta h_{x(i-1,j)}}\left(\phi^{k+1}_{i,j}-\phi^{k+1}_{i-1,j}\right)\right]+$$
$$\frac{1}{\Delta y_{i,j}}\left[\frac{\varepsilon'_{i,j}\varepsilon'_{i,j+1}}{\varepsilon'_{i,j}\Delta h_{y(i,j+1)}+\varepsilon'_{i,j+1}\Delta h_{y(i,j)}}\left(\phi^{k+1}_{i,j+1}-\phi^{k+1}_{i,j}\right)-\frac{\varepsilon'_{i,j-1}\varepsilon'_{i,j}}{\varepsilon'_{i,j-1}\Delta h_{y(i,j)}+\varepsilon'_{i,j}\Delta h_{y(i,j-1)}}\left(\phi^{k+1}_{i,j}-\phi^{k+1}_{i,j-1}\right)\right] \quad (2\text{-}22)$$
$$=-\left(\sum_{l=1}^{m}(qn)_l\right)^k$$

where $\Delta h_{x(i,j)}$ and $\Delta h_{y(i,j)}$ represents the half cell width of cell *(i,j)* in the x- and y-direction respectively. Note the effective local permittivity is defined as

$$\varepsilon'_{i,j}=\varepsilon_{i,j}+\Delta t\left(\sum_{l=1}^{m}\left(|q|\,\mu_{i,j}n_{i,j}\right)_l\right)^k \quad (2\text{-}23)$$

where the semi-implicit treatment is included.

2.5 Parallel Implementation of Fluid Modeling

At each time step, the resulting algebraic linear systems are solved equation by equation using parallel preconditioned Krylov subspace method provided by PETSc library [34] through domain decomposition technique on top of the MPI protocol. Fig. 2-1 shows the proposed flowchart of simulation. After the evaluation of transport properties and rate constants of reaction channels, the discretized governing equations are solved sequentially with acceptable time step size benefiting from the use of semi-implicit scheme.

The computational domain is decomposed with vertex-based partition [35] into several horizontal (or vertical) sub-domains along the y- (or x-) direction. In our implementation, each sub-domain is assigned to a single processor. Such partition does not distinguish different types of physical regions such as electrodes, dielectric materials, and discharge region. Hence, the sub-domain of each processor may or may not contain a region with multi-physics.

The Poisson equation is an elliptic partial differential equation (PDE) while the

continuity equations and the electron energy density equation are convection-diffusion-reaction equations either parabolic or hyperbolic types of PDE depending on the Peclet number (ratio of drift to diffusion fluxes). The continuity equations of species can be further classified into charged (such as electron and ions) and neutral species. The continuity equation of charged species consists of the mobility, the diffusivity, and the local distribution of electric field, which are varied both temporally and spatially. The coefficients of the matrices for these continuity equations need to be updated at each time step. It follows that the corresponding preconditioners of the continuity equation of charged species need to be reconstructed at each time step. On the other hand, the continuity equations of neutral species are diffusive equations and their diffusivities are treated as constant for most neutral species. Thus, the coefficients of these matrices are unchanged at each time step, leading to a constant preconditioning matrix for neutral species is sufficient.

2.6 Parallel Gas Flow Model (GFM)

The GFM employed in the present study is a two-dimensional planar and axisymmetric flow solver developed in our group [36], which simulates the background gas flow as a continuum by solving a set of governing equations including the continuity, Navier-Stokes (N-S), energy, species transport equations, and the equation of state for ideal gases. The general form of two-dimensional planar governing equations is written in the Cartesian tensor as

$$\frac{\partial(\rho\varphi)}{\partial t}+\frac{\partial}{\partial X_i}(\rho V_i\varphi)=\frac{\partial}{\partial X_i}\left(\mu_\varphi\frac{\partial\varphi}{\partial X_i}\right)+S_\varphi \tag{2-24}$$

where t is the time, $X_i=(x,y)$ is the position vector, $V_i=(u,v)$ is the velocity vector, μ_φ is an effective diffusion coefficient, S_φ is the source term, ρ is the

fluid density, and $\varphi = (1, u, v, h_t, Y_i)$ represents for the variables for the mass, momentum, energy, and mass fraction of i^{th} species, respectively. h_t $\left(h_t = \sum_i Y_i h_i + \frac{1}{2}\sum_{j=1}^{2} V_j^2 \text{ and } h_i = \int C_{p,i} dT \right)$ is the total enthalpy, where $C_{p,i}$ is the specific heat capacity of i^{th} species at constant pressure and T is the mixture temperature of the background gas flow.

The temperature distribution of solids (e.g., electrode and dielectric material) is obtained by solving the steady state heat conduction equation since we are simulating the experiment when the solids are in their steady states. The steady-state heat conduction equation is written as

$$\frac{\partial}{\partial X_i}\left(k \frac{\partial T}{\partial X_i} \right) + S_{th,solid} = 0 \qquad (2\text{-}25)$$

where k is the thermal conductivity, $S_{th,solid}$ is the heat source/sink term of the solid material. Conjugate heat transfer is considered by applying the heat flux continuity at the gas-solid interfaces.

The governing equations of the GFM are solved using a cell-centered finite-volume method, with an extended SIMPLE (Semi-Implicit Method for Pressure Linked Equations) scheme. A second-order upwind scheme with linear reconstruction is used to evaluate the inviscid flux across the cell interface. A flux limiter is used to prevent the occurrence of local extrema from being introduced by the data reconstruction. Pressure smoothing is employed to avoid the pressure oscillations on a collocation grid. The use of above numerical approaches allows the GFM solver to simulate both compressible and incompressible flows with a wide range of speeds. The computation performed by the flow solver is also parallelized using domain decomposition approach. Detailed numerical implementation and validations of the

GFM solver can be found in [36].

2.7 Hybrid Algorithm for Coupling the GFM and PFM Solvers

2.7.1 General Description

The simulation of APPJ consists of two parts, the GFM and the PFM. The GFM considers the background gas flow field including the momentum exchange with heavy charged species and gas heating produced by energy transfer due to electron-neutral elastic collisions and joule heating of ions. The PFM considers the plasma physics and chemistry accompanied with the convection of the background gas flow field. Theoretically, modeling the APPJ requires a strong coupling of the GFM and the PFM at each time step. For example, it is necessary to adopt the strong coupling of the GFM and the PFM to study the transition from non-thermal to thermal plasma with highly interaction between gas flow and discharge as reported [37]. However, the characteristic time scales of the GFM and the PFM are 1.0-10 μs and 0.01-1.0 ns respectively, in which very large timescale differences (3-6 orders of magnitude) exist. Strong coupling at each time step of the GFM and the PFM becomes unnecessary and unrealistic for a steady background gas flow; hence, these two models are integrated with a weakly coupling algorithm. The extension of PFM is added to include the convection effect, and then followed by the coupling algorithm.

2.7.2 Inclusion of Convection Effect in the PFM

The continuity equations of heavy species (i.e., ions and neutrals) introduced in earlier section do not include the convection effect due to fluid dynamics. To include the convective effect, the species flux vector $\vec{\Gamma}$ is expressed based on the drift-diffusion approximation including convection effect due to the background gas flow for heavy species as

$$\vec{\Gamma}_i = sign(q_i)\mu_i n_i \vec{E} - D_i \vec{\nabla} n_i + \vec{u} n_i \tag{2-26}$$

$$\vec{\Gamma}_{uc} = -D_{uc} \vec{\nabla} n_{uc} + \vec{u} n_{uc} \tag{2-27}$$

where $\vec{u}$ is the flow velocity vector. In addition, it is noted that the electron flux does not include the convection of the background gas flow since the speed of the electron induced by the drift of the electric field is much faster than that transported by the convection of background gas flow.

2.7.3 Details of Hybrid Algorithm for Coupling the GFM and PFM Solvers

Challenge in coupling the GFM and the PFM solvers lies in the fact that the large timescale difference of characteristic time between the background gas flow and the gas discharge. As mentioned earlier, strong coupling at each time step of discharge simulation is very time-consuming and unnecessary if transient gas flow field is not important. Thus, we adopt a weakly coupling algorithm in this study. Before describing the details of the coupling algorithm, we introduce the source terms of the momentum and energy equations, which appear in the GFM solver, due to gas discharge.

The cycle-averaged momentum source term considered in this study involves the electrohydrodynamic force [38] and can be written as

$$S_m = \frac{1}{t_p} \int_0^{t_p} \left(\sum_i q_i n_i \vec{E} - e n_e \vec{E} - \sum_i k_B T_g \vec{\nabla} n_i - k_B T_e \vec{\nabla} n_e \right) dt \tag{2-28}$$

where k_B is the Boltzmann constant, t_p is the period of the driving power source for the discharge. The elastic collision between the electron and background gas, and the summation of Joule heating of ions are integrated and averaged for each cycle and

outputted as the source term of the energy equation of the GFM. The cycle-averaged energy source can be written as

$$S_{h_t} = \frac{1}{t_p}\int_0^{t_p}\left(\sum_i q_i \Gamma_i \vec{E} + 3\frac{m_e}{M} n_e k_B \nu_m \left(T_e - T_g\right)\right)dt \tag{2-29}$$

where ν_m is the momentum exchange collision frequency between the electron (mass m_e) and the background gas (mass M), and T_g is the background gas mixture temperature.

Fig. 2-2 shows the concept of a weakly coupling algorithm of the PFM and GFM solvers, and Fig. 2-3 shows the flowchart of a complete APPJ simulation. The coupling starts from the PFM solver, and then passes cycle-averaged simulation data, such as the momentum and energy source terms, to the GFM solver. The cycle-averaged momentum and energy source terms generated from the PFM solver are passed to the GFM solver for every two discharge cycles (for the discharge driven by kHz level of power source). Next, the GFM solver takes the momentum and energy source term provided by the PFM solver and solves the governing equations to obtain the steady-state flow velocity, temperature, and number densities of the background gases. These flow properties are provided as the input for PFM solver to evaluate the convective flux, and the local plasma chemistry partly determined by the temperature and number densities of the background gases. The source terms calculated by the PFM solver and the flow properties obtained by the GFM solver are transferred back and forth to account for the effect of discharge-gas flow interactions. This process may take several iterations between the GFM and the PFM solvers to obtain a converged solution for the GFM solver. In the current study, it is observed that three iterations between the GFM solver and the PFM solvers are sufficient to obtain a converged solution for the GFM solver. For the GFM solver, the converged

solution represents the velocities, temperature, and the densities of background gases reach the steady level. The physical properties of gas flow obtained by the GFM solver do not change much after several iterations with the PFM once the converged solution is obtained.

It is noted that the PFM requires more time steps to achieve the physically quasi-steady state for the properties such as species number densities near the substrate surface even though the GFM solver has already reached the converged solution as shown in Fig. 2-3. The species generated from the discharge are then advected by the flow field obtained from the GFM solver.

2.8 Temporal Multi-Scale Method for the PFM

To capture the electron dynamics that determines plasma physics and chemistry, the simulation time step is constrained by the characteristic time scale of electron transport. As mentioned earlier, there is no need to consider the transport of heavy species, in addition to chemical reactions, during each electron time step. This motivates us to develop the temporal multi-scale method (TMSM) for the PFM solver to further reduce runtime as presented in the following.

The idea of TMSM is to ignore the transport terms of the continuity equations for heavy species when integrating them in time and restore the transport terms only at every certain (large) number of time steps. This simplifies the numerical solution of solving the continuity equations for heavy species and substantially reduces the computational time, since there is no need to solve the matrix equation during most time steps, which is very time-consuming.

Fig. 2-4 illustrates the TMSM idea in detail. It shows five typical equations (No. 1, 2, 4, 6, 7) that need to be solved at each time step in the original PFM along with those simplified equations (No. 3, 5) for ions and neutral species. Time scale factors

based on the electron time step are termed as "tf_i" and "tf_{uc}" for ions and neutral (uncharged) species respectively. For example, "tf_i=5" represents that, for every 5 time steps, a complete form of the continuity equation has to be solved for all ion species. In Fig. 2-4, the numbers above the ticks of each horizontal line represent the corresponding equations solved at certain specified time levels. The PFM is solved for all the equations in its original sequence at each time step. The Poisson equation, the electron continuity equation, and the electron energy density equation are always solved in their complete forms. For other heavy species (ions and neutrals), their continuity equations are solved in simplified forms by only considering the source terms at most of time steps. In doing so, there is no need to solve these simplified equations with matrix solvers which is time-consuming. Only at a preset time interval, controlled by the time scale factors (e.g., tf_i = 5 and tf_{uc} = 10 in Fig. 2-4), the ion and neutral continuity equations are then solved in the complete forms to restore the transport effects. In practice, these time scale factors can be as high as 1,000 found in the current study. Results of runtime reduction and the accuracy of the numerical solution using the TMSM will be presented later. Some details of the calculation procedure for restoring the transport effect are introduced next.

Each time when the time interval equals to the integral times of tf_i or tf_{uc} (i.e., $\Delta t_{i,uc} = tf_{i,uc} \times \Delta t$), the discretized continuity equations of ions and neutrals can be written as

$$\left(n_{i,uc}^{k+1} - n_{i.uc}^{k}\right) + \Delta t_{i,uc} \times \vec{\nabla} \cdot \vec{\Gamma}_{i,uc} = \Delta t \times S_{i,uc}^{k} \tag{2-30}$$

where the superscripts k and $k+1$ represent the previous and current time level respectively. It is noted that the time step size of the source term is different from that of the transport term since the source term is evaluated at every time step. The flux terms of neutrals are the same as Eq. (2-6), while those of ions can be written as

$$\vec{\Gamma}_i = sign(q_i)\mu_i n_i \vec{E}_{avg} - D_i \vec{\nabla} n_i + \vec{u} n_i \tag{2-31}$$

where $\vec{E}_{avg} = \sum_{j=1}^{tf_i} \vec{E}_j \big/ tf_i$. Note the electric field of Eq. (2-31) is averaged from the duration when solving the simplified continuity equations for ions.

Chapter 3 One-Dimensional Fluid Modeling of Helium Dielectric Barrier Discharge Considering Impurities

3.1 Background and Motivation

Helium discharge has been studied widely for a long time because of its extensive applications as introduced previously in Chapter 1. However, it is very difficult to perform the experiments with 100 % pure helium because of the limit of industrial production. Different grades of helium gas may be used to perform the experiments by different researchers. Although it was shown that helium discharge can not be predicted well with the data of pure helium chemistry and researchers indicated that the trace amount of impurity of helium gas plays an important role in the helium discharges; however, there is no report focusing on the study of helium discharge considering detailed composition of helium impurities. The existence of impurities changes the discharge species chemistry significantly as presented later though those impurity levels are as low as few to tens of ppm for helium gas with a high grade (99.99%). It is important to realize the details of the discharge chemistry to deduce the correct conclusion from the experimental observation for practical applications. Therefore, this chapter discusses the difference between helium discharge with and without considering the impurities. To reach this goal with a short turn-around time, one-dimensional fluid modeling is adopted in this chapter.

Recently, the impurity composition of high-grade commercial helium gas (purity level is 99.99%, produced by 建發氣體股份有限公司) was analyzed with a pulsed discharge helium ionization mode detector (PDHID) by gas chromatography (GC; YL 6100GC, Young Lin Instrument Co., Ltd) in our group to identify the

impurity levels (nitrogen and oxygen) and results are summarized in Table 3-1. The data of each bottle of each impurity gas in Table 3-1 was averaged from three measurements. The measured standard deviation of oxygen is 1.35 ppm, and that of nitrogen is 5.18 ppm. The relative intensity of measurement by optical emission spectroscopy (OES) does not change apparently from bottle to bottle, which explains the consistency of impurity level. Besides, the helium gas may also contain trace amount of water vapor according to the measurement of OES since the excited OH(A) has been observed with significant level in our experiments as shown in Fig. 3-1. To identify the source of OH(A), we conducted the flow simulation and showed that no entrainment occurs, which excludes the generation of OH(A) by the water vapor from ambient air. Moreover, the detector of OES has been placed close enough to the exit of discharge to forbid generation of OH(A) in the afterglow region. Therefore, it is highly suspected that helium gas contains trace amount of water vapor which is the source for OH(A) generation. However, the amount of water vapor can not be quantitatively determined by the GC because the level of water vapor is smaller than (or equal to) that of water vapor within the GC.

Therefore, the aim of this chapter is to present the effect of trace impurities of helium APDBDJ simulated by one-dimensional self-consistent PFM. The results of discharge current are compared quantitatively with measured data. The species generated from the helium discharge with and without impurities are compared. The chemistry of helium discharge with different ppm levels of water vapor has also been compared numerically to study the importance of water vapor.

3.2 Problem Description

Fig. 3-2 illustrates the schematic diagram of the planar APDBDJ along with a gas supply system and the instrumentation for electrical measurements, which is the

same as that used by Chiang *et al.* [39]. This DBD consists of two parallel copper electrodes (50×50×8 mm each) with embedded cooling water. Each of the electrodes is covered with a 70×70×1 mm ceramic plate with measured relative permittivity of 11.63. The distance between the two dielectric plates is kept as 1 mm. This DBD assembly is driven by a nearly sinusoidal power supply (DC-0505A, Taiwan Power Tech, Inc.) at a fixed frequency of 25 kHz. The input voltage and output current waveforms across the electrodes of the parallel-plate discharge are measured by a high-voltage probe (Tektronix P6015A) and a Rogowski coil (IPC CM-100-MG, Ion Physics Corporation Inc.), respectively, through a digital oscilloscope (Tektronix TDS1012B). Helium gas (99.99% purity) is used as the discharge gas that flows through the parallel plate. The flow rates are controlled by a manually adjustable flowmeter. The input voltage and output current waveforms across the electrodes of the parallel-plate discharge are measured by a current probe (Tektronix TCP312) and a high-voltage probe (Tektronix P6015A) through a digital oscilloscope (Tektronix TDS1012B).

3.2.1 Plasma Chemistry

In the plasma chemistry, we considered 36 species (e^-, He^+, He_2^+, O_2^+, O^+, O^-,O_2^-, N^+, N_2^+, N_4^+, OH^+, H_2O^+, H_3O^+, $H_5O_2^+$, $H_7O_3^+$, $H_9O_4^+$, He_m^*, He_{ex}^*, He_2^*, O_3, O, $O(^1D)$, $O(^1S)$, $O_2(a)$, NO, $N_2(A^3\Sigma_u^+)$, $N_2(B^3\Pi_g)$, $N_2(a'^1\Sigma_u^-)$, $N_2(C^3\Pi_u)$, $N(^2D)$, N, H, H_2, OH, OH(A), and H_2O_2) and 121 reaction channels as listed in Table 3-2. Reaction channels R0 to R26 consider chemistry for pure helium discharges. Reaction channels R27 to R42 describe the chemistry of oxygen and its interaction with helium, R43 to R63 model the chemistry of N_2 and its interaction with helium, R64 to R100 consider the interaction between O_2 and N_2, and R101 to R120 define the interaction

between helium and water vapor.

The transport coefficients and the rate constants related to the electrons are calculated by solving the Boltzmann equation using BOLSIG$^+$. Note that these coefficients are predicted and stored in a lookup table as a function of the electron temperature. The mobilities of the ions are taken from the literature [43][48]-[52], and the corresponding diffusivities are calculated using the Einstein relation. As for the diffusion coefficients of neutral species, such as He_m^*, He_{ex}^*, He_2^*, O_3, O, N, and OH, they are found from the literature wherever is available [43][49][53]. Those of NO, H_2, and H_2O_2 are calculated from the Chapman-Enskog equation for binary diffusion [54], in which the required parameters for calculating the diffusivity can be found from the reference [55]. The diffusivities of excited neutral species are assumed to be equal to those of the corresponding ground-state neutral species since these properties can be hardly found in the literature.

3.2.2 Simulation Conditions

The discharges between two parallel electrodes covered with ceramic plates are studied with one-dimensional fluid model under atmospheric condition as the schematic diagram shown in Fig. 3-3 with the coordinate used in this chapter. Fig. 3-4 shows the comparison of the simulated and measured discharge currents, which were sampled during the 5th cycle of the applied voltages in the simulation. It is observed that those simulated discharge currents with and without impurities are almost the same. Good agreement of discharge currents can also be found between simulations and measurements. The DBD problem investigated here is driven by nearly sinusoidal voltages with a frequency of 25 kHz. Input temporal voltages are fitted using a Fourier series expansion of 25 kHz as fundamental frequency with 15 terms in total. Two gas breakdowns during a cycle are reproduced in both phase and magnitude

accurately in the simulation.

Fig. 3-5 shows the discharge structure at the instant of maximum current density (~ 18.8 μ s in Fig. 3-4) for discharges with (10 ppm O_2, 25 ppm N_2, and 1 ppm H_2O) and without impurities. Both cases with and without impurities have similar discharge structure as shown. The "Positive" represents the density of all species with positive charge, and the "Negative" represents the density of all species with negative charge. At the instant, negative species move toward right, while positive species move toward left due to the polarity of electrodes. In most of the gap, the density of positive species is several orders of magnitude higher than that of negative species except for the region near the anode (the right electrode in this instant), which implies that the discharge can be classified as the Townsend-like discharge. However, the quasi-neutral region, which is the typical characteristic of glow-like discharge, can be observed under same conditions with larger gap distance (e.g., 2 mm). One can not observe the quasi-neutral region in Fig. 3-5 may be attributed to the short gas distance occupied by the development of cathode fall and anode fall. Hence, it requires more investigation to clarify the discharge structure.

The distributions of conduction, displacement, and total current density at the instant of maximum discharge current density are shown in Fig. 3-6. Negative species move toward right electrode, while the positive species move toward left electrode, which is same as that in Fig. 3-5. For the case considering no impurity, electrons and He_2^+ contribute to almost all amount of conduction current density since these two species are the dominant negative and positive species in the discharge without impurity as described in Section 3.3. For the case considering impurities, electrons still contribute to large amount of conduction current density. He_2^+ ions contribute to most of the conduction current density among all positive ions since they have highest density at that instant as shown later (Section 3.4). It is noted that the displacement

current densities are small in the discharges considered.

3.3 Helium Discharge without Considering Impurities

Fig. 3-7 shows the spatial-averaged distributions of number densities of helium discharge without considering impurities. There are only 6 species considered and they are electron, He^+, He_2^+, He_m^*, He_{ex}^*, and He_2^*. The number density of electron reaches approximately 10^{17} m^{-3} during the breakdown period (i.e., 10-20 us), while the number density of dominant ion He_2^+ is slighter higher than that of electron in the breakdown and reaches 10^{17} m^{-3} in its peak. The helium excimer He_2^* is the dominant neutral species with its value maintained at the level of $3x10^{18}$ m^{-3}, and the number density of helium metastable He_m^* is slightly lower than that of He_2^* with the level of 10^{18} m^{-3}.

Fig. 3-8 shows the spatial-averaged distribution of reaction rate of important channels for electron and dominant neutral species He_2^*. As shown in Fig. 3-8(a), most of the electrons are generated by the R17 that is a reaction between excited helium (He_{ex}^*) and helium background gas which produces electron and He_2^+ in the breakdown region. The high reaction rate of R17 also explains the high density of He_2^+ as the dominant ion and the low density level of He_{ex}^* since the He_{ex} is consumed through R17. It is noted that the reaction rate of R17 is higher than that of the direct ionization R8. The reaction rate of recombination between electron and He_2^+ is lower than those of generation mechanisms resulting in the high electron density (10^{17} m^{-3}) in the discharge. Most of the dominant neutral species He_2^* are generated from the high reaction rate of R21 between metastable helium and background helium, and most of the He_2^* are destructed by the dissociative reaction R26 of He_2^* and background helium.

3.4 Helium Discharge with Impurities

Table 3-1 summarizes the measured impurities of oxygen (~ 10 ppm) and nitrogen (~25 ppm) using GC. With the measuring uncertain level of water vapor, we take 1 ppm water vapor as the benchmark to compare with the helium discharge without impurity in this section. The effect of water vapor is examined in the next section.

10 ppm O_2, 25 ppm N_2, and 1 ppm H_2O

Fig. 3-9 shows the spatial-averaged distributions of number densities of helium discharge with impurities containing 10 ppm O_2, 25 ppm N_2, and 1 ppm H_2O. The electron density reaches the level of 10^{17} m^{-3} in the breakdown period, which is similar to that of helium discharge without considering impurity. The level of He_2^+ decreases tremendously to the level of $2x10^{16}$ m^{-3} during the breakdown period, while the N_2^+ becomes the dominant ion in the breakdown period with its level slightly lower than that of electrons. The He_2^+ remains the dominant ion in the post discharge (~ 20-30 μs). It is noted that the level of H_2O^+ reaches $3x10^{16}$ m^{-3} in the breakdown period though only 1 ppm water vapor considered in this case. In spite of containing only 10 ppm oxygen impurity, the ground-state atomic oxygen is the dominant neutral species with its number density reaches $2x10^{18}$ m^{-3}. The number densities of He_m and He_2 are still abundant with their levels lie between 10^{17} and 10^{18} m^{-3}. It is remarked that the density levels of N_2(A3), N(2D), and N(4s) are as high as ~10^{17} m^{-3} though the level of nitrogen impurity is only 25 ppm. The result shows that the species composition of discharge changes significantly with the consideration of trace amount of impurities in the helium discharge.

Fig. 3-10 shows the spatial-averaged distribution of reaction rate of important channels for electron, and dominant ion N_2^+, and neutral species O. Similarly, Most of

the electron are generated from the high reaction rate of R17 between excited helium He_{ex}^{*} and the background helium. Although the destruction rate of electrons increases due to the 3-body attachment (R29) with background oxygen coming from the impurities, the overall generation rates are still much higher than that of destruction rate. It is noted that two additional channels, which are Penning ionization R43 and R44 due to the high energy level of metastable helium (He_m^{*}) and helium excimer (He_2^{*}), for electron generation have comparable high reaction rates with that of direct ionization (R8) though the impurity of nitrogen is only 25 ppm. These two Penning ionization channels generate most of the dominant ion N_2^+, whereas the associative reaction R61 destroys most of the N_2^+ as shown in Fig. 3-10(b). Those reactions (R31, R41, and R118) with comparable reaction rates are responsible for the generation of ground-state atomic oxygen, while the R34 that is a reaction between metastable helium and ground-state atomic oxygen destructs most of the ground-state atomic oxygen as shown in Fig. 3-10(c).

3.5 Helium Discharges with Different Levels of Water Vapor

10 ppm O_2, 25 ppm N_2, with 1, 5, and 10 ppm H_2O

Fig. 3-11 and Fig. 3-12 show the spatial-averaged number densities of abundant species of helium discharge with impurities containing 5 and 10 ppm water vapor respectively. The number densities of electron reach approximately the same level as 10^{17} m^{-3} in the breakdown period with slightly decrease as the level of water vapor increases. The level of H_2O^+ increases and becomes the dominant charged species as the water vapor increases. The ground-state atomic oxygen (O) is the dominant neutral species as the level of water vapor increases up to 10 ppm. It can be observed that the density levels of hydroxyl (OH) and atomic hydrogen (H) increase rapidly as the water vapor increases from 1 ppm to 10 ppm. The increment of hydroxyl radical is

important for biomedical applications since it is shown that hydroxyl radicals enhance the effect of sterilization due to their high chemical reactivity [56][57]. The results obtained by Kong [47] with a global model show the similar trends as those found in this study.

3.6 Summary

We consider the helium discharge with and without impurities because of their importance in practical applications. The impurity composition of helium was obtained by gas chromatography (GC) and found that the impurity averagely contains 10 ppm O_2 and 25 ppm N_2. The impurity of water vapor is suspected because of the observation of OH(A) in the OES measurement though the amount of water vapor can not be determined by the GC because of experimental uncertainties. The plasma chemistry of helium discharge with and without considering impurities is compared, and the results of discharges with different levels of water vapor are presented and discussed.

Both discharges with and without impurities have similar levels of electron densities. He_2^+ is the dominant ion in the helium discharge without impurities, while N_2^+ is the dominant ion in the breakdown region in the helium discharge with impurities containing 1 ppm H_2O. The dominance of neutral species He_2^* in the helium discharge without impurities has been replaced by the ground-state atomic oxygen in the helium discharge with impurities.

The electron densities of helium discharges with different levels (1, 5, 10 ppm) of water vapor remain approximately the same level as the level of water vapor increases. However, H_2O^+ replaces the N_2^+ as the dominant ion as the amount of water vapor increases. Although the ground-state atomic oxygen is still the dominant neutral species, the densities of atomic hydrogen and hydroxyl increase significantly as the

water vapor increases.

The results show the importance of impurities for the helium discharges though the levels of impurities are typical several to tens ppm. It is important to realize the details of the discharge chemistry to deduce the correct conclusion from the experimental observation for applications. Therefore, it is crucial to include the impurities for simulating the helium discharge.

Chapter 4 Development of a Parallel Semi-Implicit 2D Plasma Fluid Modeling Using the Finite-Volume Method

4.1 Background and Motivation

Chapter 3 presents the results of one-dimensional fluid modeling, which is a good tool to understand the physics and chemistry of the discharge in a short turn-around time. However, it requires to employ the two-dimensional simulations to comprehend the afterglow region where is the most important region for several applications since the afterglow region can not be simplified as a one-dimensional problem.

Two major approaches, Particle-in-Cell with Monte-Carlo collision (PIC/MCC) and plasma fluid modeling (PFM hereafter), have been widely used for low-temperature plasma simulations. Generally, PFM requires less computational time than that of PIC/MCC under same test conditions if the pressure is not too low. However, the applications accompanied with large-scale (computational) domain and/or complex chemistry (species and reactions), which is not uncommon in practice, could lead to unacceptable computational time even using PFM. Acceleration of the fluid modeling is thus strongly required in simulating realistic gas discharges.

Thus, this chapter introduces the development of a parallel two-dimensional plasma fluid modeling code using the finite-volume method with the semi-implicit approach. The parallel performance of the small and large problems is presented in turn and the convergence characteristics of different types of equations are presented and discussed. The effect of different levels of ASM overlapping is compared. A demonstration of the large problem is given at the end of this chapter.

4.2 Problem Description

The computational domain is shown in Fig. 4-1. The electrodes are surrounded by Teflon, and the right-hand side domain is bounded by a substrate. The values of relative permittivity for each region employed in this study are $\varepsilon_{r,Discharge} = 1.0$, $\varepsilon_{r,Alumina} = 11.63$ (measured), $\varepsilon_{r,Teflon} = 2.1$ [58] and $\varepsilon_{r,Substrate} = 10.0$ for some dielectric material. Details of the experimental configuration can be found in Chiang *et al.* [39] and are not repeated here for brevity. Two problems with different sizes (501×310 cells and 1001×620 cells) are considered. Hereafter the former and the latter are referred to as the small and large problems respectively. The computational domain is decomposed with vertex-based partition [35] into several sub-domains along the Y direction as shown in Fig. 4-2 as an example of partition for four processors. The partition does not concern the existence of different physical regions such as electrodes, dielectric materials, and discharge region. Hence, each processor may contain the regions including electrodes, dielectric material, and discharge region. Since all the regions are meshed, the diagonal entries of matrices of linear systems belonging to the sections with Dirichlet conditions (such as electrodes of the Poisson equation, and the sections of solid materials of continuity equations) are filled with unity, and the corresponding right-hand side constants are filled with known values. In other words, the potential of electrode region is known for solving the Poisson equation. Similarly, the number densities of solid materials are known for solving the species continuity equations. The rest entries of matrices of the sections with Dirichlet conditions are filled with zero. The existence of Dirichlet conditions may lead to the issue of load balance since the unknowns of the Dirichlet conditions are given. The load balance is not discussed in this study, and it is possible to be implemented for future improvement.

The matrices resulting from the discretization are asymmetric because of the inclusion of sections with Dirichlet conditions, non-uniform cell size, and the implementation of SG scheme. We have employed GMRES due to its robustness for all cases tested. In addition, regarding preconditioning, we test the performance of additive Schwarz preconditioners, where either LU or incomplete LU decomposition without fill-in as a sub-domain solver. The effect of different levels overlapping of ASM is also tested and discussed in this study. Other preconditioners, for example, point Jacobi or Successive Over-Relaxation (SOR), are not efficient enough for the convergence of GMRES and thus excluded for further discussion. Note that GMRES without preconditioning is not worth to mention.

The data presented in the following are averaged from the results of 1,000 time steps unless otherwise specified. The employed time step in the test cases was fixed at 5×10^{-10} seconds. The relative tolerance for GMRES is set as small as 10^{-7} to guarantee the physical correctness of the computed solution. In general, except for the Poisson equation, GMRES for solving the continuity equations and the electron energy density equation converge to this criterion in less than 30 iterations. The typical number of iterations required for solving the Poisson equation is generally few hundreds. All simulations were performed on the IBM-1350 supercomputing system at the National Center for High-performance Computing (NCHC) of Taiwan with 3.0 GHz of CPU speed and 4 GB of RAM per processor.

4.2.1 Plasma Chemistry

For the case of parallel performance study, we consider a helium dielectric barrier discharge containing only trace (100 ppm) nitrogen impurity for simplicity. In the plasma chemistry, we consider 10 species (e^-, He^+, He_2^+, N^+, N_2^+, N_4^+, He_m^*, He_{ex}^{**}, He_2^*, and N) and 43 reaction channels (R0 ~ R26, R43 ~ R52, R54, and R59 ~

R63) as listed in Table 3-2. Reaction channels 0 to 26 consider chemistry for the pure helium discharge, and the rest reaction channels consider the effect of trace addition of N_2 and the interaction between helium and nitrogen as the mimics of impurity. The transport properties and rate constants are the same as those used in chapter 3.

4.2.2 Simulation Conditions

The simulation conditions are the same as those used in chapter 3. The discharge investigated here is driven by nearly sinusoidal voltages with a frequency of 25 kHz. Input temporal voltages are fitted using a Fourier series expansion of 25 kHz as fundamental frequency with 15 terms in total. The voltage waveform is the same as that used in chapter 3.

4.3 Small Problem Case

Fig. 4-3 shows the averaged runtimes required for each time step for each of the different equation types solved by GMRES with one-level overlapping ASM preconditioning by different numbers of processors for the small problem. Table 4-1 summarizes the average number of iterations required for convergence for all the equations solved. The presented results using two types of sub-domain solvers are also included, which consist of ILU and LU. Generally speaking, the computational expense associated with each component of the plasma simulation can be sorted (in order from most expensive to least expensive) as the Poisson equation, the electron energy density equation, the electron continuity equation and the neutral-species continuity equation. Despite its mathematical simplicity, solving the Poisson equation requires most of the computational resources because of the general difficulties associated with the elliptic PDEs with discontinuous jump coefficients. Although both the electron energy density equation and the electron continuity equation are

convection-diffusion-reaction types of PDEs, it requires further investigation to explain that GMRES for the former equation is more difficult to converge. GMRES for the neutral-species continuity equation converges fastest among all the equations and thus requires the lowest computational time. Note that the constant preconditioner of neutral species are constructed only at the first time step, which further reduces the computational time.

The cases with preconditioning using the LU method required fewer number of iterations than those using the ILU method since the LU method obtains more accurate solutions in each sub-domain than the ILU method. In addition, the number of iterations increases with increasing number of processors. This is mainly because the corresponding preconditioner is divided into more sub-domains while more processors are used. Although each sub-domain is solved correctly with the LU method or the ILU method, the overall performance of the ASM preconditioning is not as good as that when fewer processors are used. This is caused by more erroneous inter-processor boundary data because of domain decomposition. In other words, the domain decomposition of the preconditioner induces slower convergence for solving the linear algebraic systems when using an iterative method as more processors are used. Resulting performance characteristics of the Poisson equation show a dramatic increase of number of iterations as more processors are used, while only slight increases in number of iterations are experienced for the solution to the remaining equations, with increasing numbers of processors. The overall performance of the cases using the ILU and the LU methods are comparable and there is no advantage in time saving when more than 64 processors are employed for the small problem presented.

4.4 Large Problem Case

Fig. 4-4 shows the average runtime per time step for solving all the equations with sub-domain of one-level overlapping ASM preconditioner solved by the ILU and LU methods for the large problem. Table 4-2 summarizes the corresponding numbers of iterations for the same cases. Similar to the previous small problem, solving the Poisson equation takes most of the computational time. The solution of the electron energy density equation converges slower than the electron continuity equation, while the neutral-species continuity equation contributes the least computational time.

The number of iterations required for the convergence of the large problem is higher than that of the small problem, especially for the Poisson equation as shown in Table 4-2, because a much larger matrix system results from the former than the latter. The number of iterations of the large problem also increases while more processors are used. The overall parallel performance improves because of the increased grain size.

In brief summary, the computational time using the ILU method is faster than that using the LU method, mainly because the LU factorization is more costly in each sub-domain for the large problem.

4.5 Parallel Performance

Fig. 4-5 and Fig. 4-6 show the speedup of the one-level overlapping ASM preconditioning solved by the ILU and LU methods for the small and large problems respectively. In these two figures, we take timings using two processors as the baseline for calculating the speedup.

Results show the speedup achieves up to 50 times as 64 processors are used for the small problem (Fig. 4-5), and levels off afterwards with either ILU or LU solver for the sub-domain of ASM preconditioner for the small problem. For the large

problem, the performance of cases with sub-domain of ASM preconditioner solved by ILU with an increase in performance of up to 130 times using 128 processors, which is better than those with LU method (Fig. 4-6). The absolute runtime of cases with ILU method of ASM preconditioner are also less than those of cases with LU method, e.g., 0.68 second/step vs. 0.94 second/step using 128 processors. The above observations show that parallel computing using domain decomposition with MPI for a two-dimensional fluid modeling code can be very useful in practice in greatly reducing the computational time up to two orders of magnitude with a limited number of processors (e.g., 60-128).

4.6 Effect of ASM Overlapping

To further explore the performance of linear solver GMRES with ASM preconditioner, we increase the level of overlapping of ASM preconditioner. The results are shown in Table 4-3 and Table 4-4 for the sub-domain of ASM solved by ILU and LU methods on the large problem. The results of small problem are not shown here due to the similar trends as those of large problem. In general, the numbers of iterations of cases with the higher level overlapping for both the ILU and the LU methods are generally reduced for all the equations for the same number of processors as shown in Table 4-3(a) and Table 4-4(a) respectively. The higher level overlapping ASM preconditioning increases rate of information propagation among various sub-domains, which generally speeds up convergence (or reduces the number of iterations). However, this increase of convergence pays off with an increasing amount of data communication, which may in turn trade off the benefit of increasing rate of convergence. For most of the test cases, the increased level of overlapping does not reduce the runtime for all types of equations (not shown in this study). The relative overall runtime of test cases with different levels of overlapping are shown in

Table 4-3(b) and Table 4-4(b). It is noted that different runtime for the same test case is obtained (in the range of 10 % ~ 20 %) because of reasons such as system loading on the cluster. To avoid confusion with different runtime obtained from the test cases in same test conditions, the relative overall runtime is calculated on the basis of one-level overlapping.

4.7 Demonstration of the Results of the Large Problem in 5th Cycle

To demonstrate the capacity of the developed parallel fluid modeling code for predicting complex plasma phenomena, we have conducted a complete simulation of the large problem as sketched in Fig. 4-1. The helium discharge (with nitrogen impurity of 100 ppm) in this simulation is driven by a nearly sinusoidal voltage with 3.0 kV in amplitude and 25 kHz in frequency under atmospheric-pressure condition. As mentioned earlier, there are six charged species, four neutral species, and 43 reaction channels involved in this demonstration. The complete simulation run for 5 cycles took about 48 hours by using 128 processors with the time size of 5×10^{-10} second. It is noted that simulation of the small problem diverges after a half cycle due to the insufficient resolution to reach the convergence. It is also noted that the convergence and computational time required for solving equations are varied in different phases of one cycle; therefore, the runtime of this demonstration case may not be consistent with the runtime given in Fig. 4-6.

The breakdown of computational time consumed by the solution of different type of equations is shown in Fig. 4-7. It takes 87.7 % of the total time for solving all governing equations and 12.3 % of that for data communication and other calculation such as evaluation of transport properties and rate constants. Fig. 4-8 shows several typical cycle-averaged spatial distributions of plasma properties such as the potential, the electron temperature (T_e), the number density of electron, and the number density

of N_4^+, which is the dominant positive ion, near the exit of the parallel-plate DBD at the 5th cycle. The average plasma potential is calculated to be 140 volts in the bulk, which is higher than those of sheaths which are positively charged. The distribution of T_e shows that the average T_e is approximately 4~5 eV in both bulk and sheaths, which is generally high as compared to those driven by MHz-level atmospheric-pressure discharges. The electron number density is sustained at about 10^{16} m^{-3} and N_4^+ is sustained at the same order of magnitude (10^{16}). The detailed plasma physics and chemistry of this problem will be reported elsewhere in the near future.

4.8 Summary

In this chapter, we have presented a parallel two-dimensional fluid modeling solver using the cell-centered finite-volume method. The parallel performance of the four equation types present in these plasma simulations (the Poisson equation, the electron continuity equation, the neutral-species continuity equation, and the electron energy density equation) are presented for the cases solved by the parallel GMRES with parallel ASM preconditioning. Two problem sizes (small and large) are studied using the ILU and LU methods for sub-domain solution in parallel ASM preconditioning. The plasma chemistry investigated (helium with nitrogen impurity) includes 10 species and 43 reaction channels. A practical atmospheric-pressure discharge driven by a 25 kHz power source is also presented to demonstrate the capability of the developed parallel code.

In brief summary, the computational expense associated with each component of the plasma simulation can be sorted (in order from most expensive to least expensive) as the Poisson equation, the electron energy density equation, the electron continuity equation and the neutral-species continuity equation. Results show that an increase in performance of up to 50 times using 64 processors with either ILU or LU

method is applied for the sub-domain of ASM preconditioner for the small problem, while an increase in performance of up to 130 times with ILU method and 60 times with LU method using 128 processors for the large problem are obtained. The investigation of GMRES with different levels overlapping of ASM preconditioner shows that the increased level of ASM overlapping have no significant effect to reduce the runtime though the iteration numbers are reduced. The results demonstrate that parallel computing using domain decomposition with MPI for a two-dimensional fluid modeling code can be very useful in practice in greatly reducing the computational time up to two to three orders of magnitude with a limited number of processors.

Chapter 5 A Parallel Hybrid Numerical Algorithm for Simulating an Atmospheric-Pressure Plasma Jet

5.1 Background and Motivation

Despite the wide applications of APPJ, the understanding of the underlying physics and chemistry is limited because it is difficult and time-consuming to measure the properties of discharges in detail. Although the numerical simulation provides another way to realize the complex characteristics of discharge with the assistance of advanced numerical scheme and development of computing hardware, it is still very challenging to simulate the APPJ since the discharge interacts with the background gases governed by fluid dynamics.

The ignorance of fluid dynamics effect for gas discharge simulation is considered to be valid at the low-pressure condition. However, fluid dynamics is expected to be important and can not be neglected for the gas discharge at high pressure condition such as the APPJ. Thus, it is necessary to appropriately model and integrate the gas flow and gas discharge simultaneously for a better understanding of the APPJ.

This chapter presents the result of the developed efficient hybrid numerical algorithm for coupling weakly the PFM and GFM utilizing parallel computing for the practical complete simulation of helium APDBDJ which is a typical type of APPJ. The converged steady-state results of flow field are presented, and the proposed temporal multi-scale method (TMSM) to reduce dramatically the runtime of the PFM has been validated with its performance given. The simulation of realistic helium APDBDJ impinging onto a substrate is employed at the end of this chapter to demonstrate the developed numerical approach/solvers, and its computational

efficiency.

5.2 Problem Description

The helium APDBDJ with trace nitrogen (100 ppm) flowing through two parallel electrodes (5×50 mm^2) each covered by a ceramic layer (alumina, 1 mm thick) as shown in Fig. 5-1 is simulated for demonstration of the developed parallel coupling numerical algorithm and the TMSM for PFM. The test configuration is similar to that of the experimental study by Chiang *et al* [39], except that the length of the electrode becomes 5 mm from the original 50 mm. The helium (30 SLM) flows into the gap (1 mm wide) from the left to the right into an environment filled with air (78 % N_2 and 22 % O_2) and impinges on the substrate at the right. The resulting Reynolds number based on the gap distance and the average inlet flow speed is 90, which is a typical laminar flow. The Peclet number of mass diffusion is calculated as

$$Pe_{mass} = \mathrm{Re} \times Sc = 90 \times \frac{1.98 \times 10^{-5}}{0.163 \times \left(2.25 \times 10^{-4}\right)} = 48.6$$

and the Peclet number of thermal diffusion is written as

$$Pe_{thermal} = \mathrm{Re} \times \mathrm{Pr} = 90 \times 0.667 = 60.03$$

It is noted that both the Peclet numbers of mass diffusion and thermal diffusion are much larger than 1.0, which explains the importance of fluid dynamics. The background gas species considered in the GFM solver include helium, nitrogen, and oxygen since they determine the local discharge chemistry and their densities are determined by the flow field and the temperature distribution modeled in the GFM solver. A realistic nearly sinusoidal voltage with $V_{peak\text{-}to\text{-}peak}$ = 6.0 kV and a frequency of 25 kHz is applied to the electrodes. All simulations were performed on the ALPS supercomputing system at the National Center for High-performance Computing (NCHC) of Taiwan with 2.2 GHz of CPU speed and 2.67 GB of RAM per processor.

Table 5-1 and Table 5-2 summarize the boundary conditions applied to the PFM and the GFM respectively. The flux of species continuity equation at the flow inlet (*JA* in Fig. 5-1) is specified as zero since it is assumed no discharge species flows from the inlet flow, while the flux at the flow outlet (*CD*, and *GH* in Fig. 5-1) is calculated based on the convection because the species is carried away by the background gas flow for heavy species (i.e., ions and neutrals). The boundary conditions of PFM at the solid-discharge interface (*ALC*, *DG*, and *JKH* in Fig. 5-1) are similar to those boundary conditions applied in [59]. The inlet flow velocity and species fraction are calculated from the inlet flow conditions, and the inlet temperature is assumed as 300 K. The inlet pressure is calculated to balance the pressure difference between flow inlet (*JA* in Fig. 5-1) and flow outlet (*CD*, and *GH* in Fig. 5-1) since the pressure at the flow outlet is set as one atmosphere (760 torr). Neumann boundary condition is assumed for the flow outlet boundary. Conjugate heat transfer is considered at the solid-fluid interfaces (*ALC*, *DG*, and *JKH* in Fig. 5-1), and Neumann boundary condition is assumed for energy equation at the boundaries of computational domain.

5.2.1 Plasma Chemistry

In this study, we have employed a realistic dielectric barrier discharge (DBD) jet with helium consisting of nitrogen impurity (100 ppm) to verify and demonstrate the developed numerical approach and its computational efficiency. The helium gas flows through the gap between two parallel electrodes and impinges on the substrate with its surroundings filled with air. The simple chemistry set of air (the composition is simplified as 78% N_2 and 22% O_2) is also included for completeness since the surroundings is filled with air for most of APPJ applications. In the plasma chemistry, we considered 25 species (e^-, He^+, He_2^+, O_2^+, O^+, O^-,O_2^-, N^+, N_2^+, N_4^+, He_m^*, He_{ex}^*,

He_2^*, O_3, O, $O(^1D)$, $O(^1S)$, $O_2(a)$, NO, $N_2(A^3\Sigma_u^+)$, $N_2(B^3\Pi_g)$, $N_2(a'^1\Sigma_u^-)$, $N_2(C^3\Pi_u)$, $N(^2D)$, N) and 101 reaction channels (R0 ~ R100) as listed in Table 3-2. Reaction channels R0 to R26 consider chemistry for pure helium discharges. Reaction channels R27 to R42 describe the chemistry of oxygen and its interaction with helium, R43 to R63 model the chemistry of N_2 and its interaction with helium, and R64 to R100 consider the interaction between O_2 and N_2. No impurities of oxygen and water vapor considered for simplicity. The transport properties and rate constants are the same as those used in chapter 3.

5.3 Steady-State Results of Flow Field

Fig. 5-2 shows the converged steady-state results of temperature distribution and flow field obtained from the GFM solver after three iterations with the PFM solver. Iterating further with the PFM does not change the results of the GFM solver significantly as mentioned previously. As shown in Fig. 5-2(a), the neutral gas temperature rises from 300 K to 303 K caused by the gas heating through electron-neutral elastic collision and ionic Joule heating as it passes through the region of parallel electrodes since this region has the highest discharge intensity. The temperature increase is very small because of the short electrode length. In Fig. 5-2(b), the maximum flow speed reaches 16 m/s in the gap and the streamlines demonstrate that the flow produces several pairs of vortices above the substrate surface. The complex flow structure affects the distribution of charged and neutral species generated by the DBD, which will be shown later. Further investigation is definitely necessary to reveal the impact of flow structure on the substrate surface for APPJ applications. The converged steady-state results of the GFM solver are adopted for the fluid model simulations in this study.

5.4 Verification of TMSM

Fig. 5-3 shows the cycle-averaged number densities of electrons, dominant ion (N_4^+), and dominant neutral species (N_2(A3)) at the 10^{th} cycle for the cases without (a, c, e) and with (b, d, f) applying the TMSM. The number density of electron reaches $7\times10^{16}\ m^{-3}$ in the bulk region of discharge within the parallel electrodes, and the density level in the downstream above the substrate surface drops rapidly down to $10^{9}\sim10^{10}\ m^{-3}$. The maximum number density of N_4^+ is slightly higher than that of electron in the bulk region of discharge within the parallel electrodes, and the density level of N_4^+ in the downstream is also higher than that of electron. Abundant metastable state N_2(A3) is generated in the discharge region ($\sim 2\times10^{18}\ m^{-3}$). It is noted that current level of number density represents the "cycle-averaged snapshot" of transient process and the discharge requires much more time steps to reach the quasi-steady state. As shown in Fig. 5-3, almost identical distributions of species number densities are obtained for the cases with and without applying the TMSM. Similar results are also obtained for other species, but not shown here. The result clearly verifies the accuracy of the proposed TMSM applied to the PFM.

The simulation of plasma discharge in the PFM needs to solve the Poisson equation, the species continuity equations, and the electron energy density equation. Among these equations, solving the Poisson equation is the most expensive one because it requires the largest number of iterations to obtain the converged solution under the same convergence criteria due to the difficult convergence of elliptic partial differential equation as discussed in [59]. However, it takes usually most of the runtime for solving the species continuity equations since many species (25 in this case) are often considered for modeling realistic applications. Fig. 5-4 shows the breakdown of runtime for solving these equations and other computer operations

(such as calculating transport properties and rate constants, and communication among processors) for the cases with and without applying the TMSM. The runtime shown in Fig. 5-4 shows the fractions of runtime for different parts of the code in a typical cycle that is averaged from five cycles. The control case (without applying the TMSM) shows that it takes more than 6 hours for one cycle by using 192 processors and about 55% runtime for solving the species continuity equations. The case with the application of TMSM shows that the runtime for solving the species continuity equations is reduced to only 14%, and it takes about 3.5 hours for one cycle by using the same amount of processors (192 processors). The total reduction in runtime is 47% because of the use of the TMSM in this study. Of course, the reduction of runtime increases with an increase of the number of heavy species associated with discharge. Thus, the TMSM is especially useful for simulating discharge with very complex plasma chemistry which involves a large number of heavy species that is not uncommon in practice.

It is obvious that the runtime for solving the continuity equations of heavy species strongly depends upon the size of time factors for ions and neutral species when using the TMSM in PFM. The larger the time factors, the less the runtime is required for solving the continuity equations of heavy species. However, the increase of time factor also raises the numerical error. The allowed maximum time factor of the PFM for applications depends on the transport term of the species continuity equation. In fact, the runtime for solving the species continuity equations reduces close to its minimum as the time factor used is larger than several tens, (e.g. 50). It means that the runtime for solving the species continuity equations with tf = 50 is almost equal to that with tf = 500 since it takes a much larger portion of the runtime to solve the electron continuity equation at each time step, as compared to the direct time integration of the continuity equations of heavy species. In this study, $tf_i = 50$ and

$tf_{uc} = 50$ are used for the case presented in Fig. 5-4. Further increase of the time factor has little impact on the runtime reduction for solving the continuity equations. Based on some numerical experiments, the values of both tf_i and tf_{uc} can be as large as 1,000 without losing the accuracy though the required runtime is almost equal to that with $tf = 50$ as explained above.

5.5 Demonstration of APPJ Simulation

To demonstrate the developed hybrid numerical algorithm is capable of simulating realistic APPJ problems, the cycle-averaged spatial distributions of properties at 200th cycle are presented in Fig. 5-5. It is observed that the species number densities reach nearly a quasi-steady state in the region near the substrate. The electron temperature (Te) of the discharge in the gap between two electrodes is approximately 3 ~ 4 eV, which is slightly higher than that of discharges driven by MHz-level atmospheric-pressure discharges [43]. The electron density in the bulk region between electrodes is in the range of 10^{16} -10^{17} m^{-3}, while the density of dominant ion (N_4^+) has the same level as that of electron and reaches a maximum of 8.5×10^{16} m^{-3} in the gap. The density of N_4^+ within the gap decreases one order of magnitude from the edge of electrode (at x = 10mm) to the edge of Teflon (at x = 15 mm) due to the decrease of the electric field. After leaving the edge of Teflon, the N_4^+ is carried by the gas flow and impinges on the substrate surface with a density level of 10^{15} m^{-3} in the region near the stagnation point. The density of N_4^+ decreases slowly and maintains its level at 10^{14} ~ 10^{15} m^{-3} along the substrate. The density of N_4^+ within the recirculation zone is relatively lower (1×10^{14} ~ 5×10^{14} m^{-3}) than that right above the substrate. In addition, Fig. 5-5(d) shows the number density distribution of the metastable N_2(A3), which is also strongly correlated with the background gas flow pattern near the substrate. Note the number density level of long-lived N_2(A3) in the

region near the stagnation point can be more than 10^{18} m^{-3}, which is important in various APPJ applications, e.g., Chiang *et al* [39]. In other words, the gas flow pattern in the post-discharge region determines the distribution pattern of heavy species which is the most important region in several APPJ applications. It demonstrates the importance of background gas flow dynamics in APPJ simulations.

5.6 Summary

In this chapter, we have proposed a hybrid numerical algorithm which couples weakly the gas flow model (GFM) solver and the plasma fluid model (PFM) solver for simulating the gas flow and discharge of an atmospheric-pressure plasma jet (APPJ). We have employed two numerical approaches to accelerate the computation. The coupling of the GFM solver and the PFM solver is performed by exchanging the results obtained from the steady-state solution (velocities, temperature, and species densities of background gas flow) of the GFM solver with the cycle-averaged solution (the momentum and energy sources) of the PFM solver. Acceleration of the hybrid numerical algorithm include parallel computing of both solvers with domain decomposition using message passing interface on distributed-memory machines and the temporal multi-scale method (TMSM) for the PFM by taking advantage of the large timescale differences between electron and heavy species. A realistic helium APDBDJ problem, including trace nitrogen (100 ppm) driven by a power source of $V_{peak\text{-}to\text{-}peak}$ = 6.0 kV and frequency of 25 kHz and considering 25 species with 101 reaction channels, is simulated. The coupling starts with the calculation of the PFM, and then the converged solution of the GFM solver is obtained after three iterations between two solvers in the present study.

The TMSM takes advantage of the transport characteristic of heavy species in the PFM. Transport terms in the continuity equations of heavy species are included in the

calculations only at the time that is larger than an integer times of the electron time step without losing accuracy. Nearly identical results can be obtained for the cases with and without applying the TMSM. The total reduction in runtime is 47% of the TMSM is applied to the helium APDBDJ simulation presented in this study.

The nearly quasi-steady cycle-averaged results obtained at the 200^{th} cycle as presented. The electron and dominant ion (N_4^+) are sustained at the same density level (~10^{16} m^{-3}) in the discharge region between two parallel electrodes, while the dominant neutrals ($N_2(A3)$) reaches the density level of 10^{18} m^{-3}. It is shown that the distributions of heavy species near the substrate strongly depend upon gas fluid dynamics. The results demonstrate the importance of considering the background gas flow effect in the APPJ simulations. More details of the physical results will be presented elsewhere in the near future.

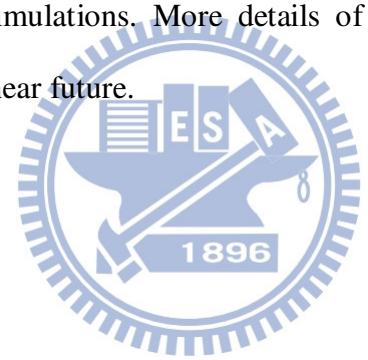

Chapter 6 Conclusion and Recommendations of Future Work

In this chapter, the major findings of the thesis are summarized as follows in turn as: 1) One-Dimensional Simulation of Helium Discharge with Impurities; 2) Development of a Parallel Semi-Implicit 2D Plasma Fluid Modeling Code Using Finite-Volume Method; 3) A Parallel Hybrid Numerical Algorithm for Simulating an Atmospheric-Pressure Plasma Jet. Some recommendations for future work that uses and extends the developed algorithm and code are given at the end of this chapter.

6.1 Summaries of the Thesis

6.1.1 One-Dimensional Simulation of Helium Discharge with Impurities

In this part of work, we consider the helium discharge with and without impurities because of their importance for applications. The impurity composition of helium was analyzed by gas chromatography (GC), which is a common method used in analytical chemistry for separating compounds, and found that the impurity averagely contains 10 ppm O_2 and 25 ppm N_2. The impurity of water vapor is suspected because of the observation of OH(A) in the OES measurement though the amount of water vapor can not be determined by the GC because the level of water vapor is smaller than (or equal to) that of water vapor within GC. The chemistry of helium discharge with and without impurities is compared, and the results of discharges with different levels of water vapor have been presented. The major findings are summarized as follows:

(1) Both discharges with and without impurities have similar levels of electron

densities. He_2^+ is the dominant ion in the helium discharge without impurities, while N_2^+ is the dominant ion in the breakdown region in the helium discharge with impurities containing 1 ppm H_2O. The dominance of neutral species He_2^* in the helium discharge without impurities has been replaced by the ground-state atomic oxygen.

(2) The electron densities of helium discharges with different levels (1, 5, 10 ppm) of water vapor remain at same level as the ingredient of water vapor increases. However, H_2O^+ replaces the N_2^+ as the dominant ion as the water vapor increases. Although the ground-state atomic oxygen is still the dominant neutral species, the densities of atomic hydrogen and hydroxyl increase significantly as the water vapor increases.

(3) The results show the importance of impurities for the helium discharges though the levels of impurities are typical few ppm. It is important to realize the details of the discharge chemistry to deduce the correct conclusion from the experimental observation for applications. Therefore, it is crucial to include the impurities to simulate the helium discharge.

6.1.2 Development of a Parallel Semi-Implicit 2D Plasma Fluid Modeling Using Finite-Volume Method

We have presented a parallel two-dimensional fluid modeling solver using the cell-centered finite-volume method in this section. The parallel performance of the four equation types present in these plasma simulations (the Poisson equation, the electron continuity equation, the neutral-species continuity equation, and the electron energy density equation) are presented for the cases solved by the parallel GMRES with parallel ASM preconditioning. Two problem sizes (small and large) are studied using the ILU and LU methods for sub-domain solution in parallel ASM

preconditioning. The plasma chemistry investigated (helium with nitrogen impurity) includes 10 species and 43 reaction channels. A practical atmospheric-pressure discharge driven by a 25 kHz power source is also presented to demonstrate the capability of the developed parallel code. The major findings are summarized as the follows:

(1) The computational expense associated with each component of the plasma simulation can be sorted (in order from most expensive to least expensive) as the Poisson equation, the electron energy density equation, the electron continuity equation and the neutral-species continuity equation.

(2) Results show that an increase in performance of up to 50 times using 64 processors with either ILU or LU method is applied for the sub-domain of ASM preconditioner for the small problem, while an increase in performance of up to 130 times with ILU method and 60 times with LU method using 128 processors for the large problem are obtained.

(3) The investigation of GMRES with different levels overlapping of ASM preconditioner shows that the increased level of ASM overlapping have no significant effect to reduce the runtime though the iteration numbers are reduced.

(4) The results demonstrate that parallel computing using domain decomposition with MPI for a two-dimensional fluid modeling code can be very useful in practice in greatly reducing the computational time up to two to three orders of magnitude with a limited number of processors.

6.1.3 A Parallel Hybrid Numerical Algorithm for Simulating an Atmospheric-Pressure Plasma Jet

A hybrid numerical algorithm which couples weakly the gas flow model (GFM) solver and the plasma fluid model (PFM) solver for simulating the gas flow and

discharge of an atmospheric-pressure plasma jet (APPJ) has been proposed. We have employed two numerical approaches to accelerate the computation. The coupling of the GFM solver and the PFM solver is performed by exchanging the results obtained from the steady-state solution (velocities, temperature, and species densities of background gas flow) of the GFM solver with the cycle-averaged solution (the momentum and energy sources) of the PFM solver. Acceleration of the hybrid numerical algorithm include parallel computing of both solvers with domain decomposition using message passing interface on distributed-memory machines and the temporal multi-scale method (TMSM) for the PFM by taking advantage of the large timescale differences between electron and heavy species. A realistic helium APDBDJ problem, including trace nitrogen (100 ppm) driven by a power source of $V_{peak\text{-}to\text{-}peak}$ = 6.0 kV and frequency of 25 kHz and considering 25 species with 101 reaction channels, is simulated. The major findings are summarized as follows:

(1) The coupling starts with the calculation of the PFM, and then the converged solution of the GFM solver is obtained after three iterations between two solvers in the present study.

(2) The TMSM takes advantage of the transport characteristic of heavy species in the PFM. Transport terms in the continuity equations of heavy species are included in the calculations only at the time that is larger than an integer times of the electron time step without losing accuracy. Nearly identical results can be obtained for the cases with and without applying the TMSM. The total reduction in runtime is 47% of the TMSM is applied to the helium APDBDJ simulation presented in this study.

(3) The nearly quasi-steady cycle-averaged results obtained at the 200th cycle as presented. The electron and dominant ion (N_4^+) are sustained at the same density level (~10^{16} m^{-3}) in the discharge region between two parallel electrodes, while the dominant neutrals (N_2(A3)) reaches the density level of 10^{18} m^{-3}. It is shown that the

distributions of heavy species near the substrate strongly depend upon gas fluid dynamics. The results demonstrate the importance of considering the background gas flow effect in the APPJ simulations. More details of the physical results will be presented elsewhere in the near future.

6.2 Recommendations for Future Work

The developed fluid model code has established the foundation for simulating realistic atmospheric-pressure plasma jets by weakly coupling the PFM and GFM with the efficient algorithm as presented earlier in the thesis. The bottleneck of runtime, which is the runtime of PFM, has been reduced significantly by the proposed TMSM and parallel computing on distributed-memory machines. The reduction in runtime leads to the possibility to treat discharge chemistry with large amount of species with an acceptable runtime. Based on these achievements, the directions of research recommended for further studies are summarized as follows:

(1) To validate the developed code and model with the well-studied phenomena (such as air plasmas, or the generation of O_3) found in the experiments.

(2) To simulate the helium APDBDJ with impurities including oxygen, nitrogen and water vapor for fully understanding the density distributions of species in the afterglow region.

(3) To study the plasma physics and chemistry of APPJ. APPJ with different gases leads to different discharge physics and chemistry. Most of the details of APPJ remain unclear due to the difficulties in detailed measurements. Using the developed tool to simulate these APPJ is useful to reveal the underlying complex physics. For example, the geometry effect, such as the stepped electrodes [60] that leads to higher concentration of oxygen addition into argon, in APPJ is still unclear. Moreover, the behavior of plasma bullet [61] is still vague since it is difficult to measure and

simulate. The developed code is a good tool to clarify those mechanisms.

(4) To further extend the capability of the code by coupling with the time-dependent Maxwell equation solver. This tool can be very useful in semiconductor fabrication industry. For example, this can be used for simulating the gas discharge in a PECVD chamber driven by very high-frequency power source and very large area of substrate that has a pronounced standing wave problem.

(5) To adopt the curvilinear coordinate transformation or unstructured grid for the plasma fluid modeling to extend the capability of the code in handling gas discharges having complex geometry.

(6) To extend the code from 2D to 3D for simulating the discharges with unsymmetrical behaviors.

References

[1] H. S. Park, S. J. Kim, H. M. Joh, T. H. Chung, S. H. Bae, and S. H. Leem, "Optical and electrical characterization of an atmospheric pressure microplasma jet with a capillary electrode," Phys. Plasmas 17, 033502 (2010).

[2] A. Grill, Cold Plasma in Materials Fabrication: From Fundamentals to Applications, IEEE Press, New York, 1994

[3] R. Hippler, H. Kersten, M. Schmidt, and K. H. Schoenbach, Low Temperature Plasmas Vol 1, 2nd Edition, Wiley-VCH, Berlin, (2008).

[4] S. Eliezer, and Y. Eliezer, The Fourth State of Matter, Institue of Physics Publishing, Philadelphia, 2001

[5] A. Fridman, Plasma Chemistry, Cambridge University Press, New York, 2008

[6] A. Fridman, and L. A. Kennedy, Plasma Physics and Engineering, Taylor and Francis, New York, 2004

[7] U. Kogelschatz, "Dielectric-Barrier Discharges," Plasma Chemistry and Plasma Processing 23, 2003

[8] T. Martens, doctoral thesis: Numerical Simulation of Dielectric Barrier Discharges, 2010

[9] http://www.freepatentsonline.com/6534423.html

[10] S. Z. Li, and J. P. Lim, "Comparison of sterilizing effect of nonequilibrium atmospheric-pressure He/O-2 and Ar/O-2 plasma jets," Plasma Science & Technology 10, 61 (2008).

[11] J. Y. Jeong, S. E. Babayan, V. J. Tu, J. Park, I. Henins, R. F. Hicks, and G. S. Selwyn, "Etching materials with an atmospheric-pressure plasma jet," Plasma Sources Science and Technology 7, 282 (1998).

[12] Y. Qiu, Y. J. Hwang, C. Zhang, B. L. Bures, and M. McCord, "Atmospheric

pressure helium plus oxygen plasma treatment of ultrahigh modulus polyethylene fibers," Journal of Adhesion Science and Technology 16, 449 (2002).

[13] S. Yang, and M. C. Gupta, "Surface modification of polyethyleneterephthalate by an atmospheric-pressure plasma source," Surface and Coating Technology 187, 172 (2004).

[14] C. H. Yi, Y. H. Lee, and G. Y. Yeom, "The study of atmospheric pressure plasma for surface cleaning, " Surface and Coatings Technology 171, 237 (2003).

[15] Y. F. Hong, J. G. Kang, H. Y. Lee, H. S. Uhm, E. Moon, and Y. H. Park, " Sterilization effect of atmospheric plasma on Escherichia coli and Bacillus subtilis endospores," Letters in Applied Microbiology 48, 33 (2009).

[16] F. Massines, A. Rabehi, P. Decomps, R. B. Gadri, P. Segur, and C. Mayoux, "Experimental and theoretical study of a glow discharge at atmospheric pressure controlled by dielectric barrier," Journal of Applied Physics 83, 2950 (1998).

[17] X. H. Yuan, and L. L. Raja, "Role of trace impurities in large-volume noble gas atmospheric-pressure glow discharges," Applied Physics Letters 81, 814 (2002)

[18] Y. B. Golubovskii, V. A. Maiorov, J. Behnke, J. F. Behnke, "Modelling of the homogeneous barrier discharge in helium at atmospheric pressure," Journal of Physics D: Applied Physics 36, 39 (2003)

[19] L. Mangolini, C. Aderson, J. Heberlein, and U. Kortshagen, " Effects of current limitation through the dielectric in atmospheric pressure glows in helium," Journal of Physics D: Applied Physics 37, 1021 (2004)

[20] T. Martens, A. Bogaerts, W. J. M. Brok, and J. V. Dijk, "The dominant role of impurities in the composition of high pressure noble gas plasmas," Applied Physics Letters 92, 041504 (2008)

[21] J. van Dijk, K. Peerenboom, M. Jimenez, D. Mihailova, J. van der Mullen, "The plasma modelling toolkit Plasimo," Journal of Physics D: Applied Physics 42, 194012

(2009).

[22] C. T. Hung, M. H. Hu, J. S. Wu, and F. N. Hwang, " A new paradigm for solving plasma fluid modeling equations," Computer Physics Communications 177, 138 (2007).

[23] C. T. Hung, Y. M. Chiu, F. N. Hwang, and J. S. Wu, "Development of a parallel implicit solver of fluid modeling equations for gas discharges," Computer Physics Communications 182, 161 (2011).

[24] P. L. G. Ventzek, T. J. Sommerer, R. J. Hoekstra, and M. J. Kushner, "Two-dimensional hybrid model of inductively-coupled plasma sources for etching," Applied Physics Letters 63, 605 (1993).

[25] G. J. M. Hagelaar, and G. M. W. Kroesen, " Speeding up fluid models for gas discharges by implicit treatment of the electron energy source term," Journal of Computational Physics 159, 1 (2000).

[26] Y. Saad, M. H. Schultz, "Gmres – a generalized minimal residual algorithm for solving nonsymmetric linear-systems," Siam Journal on Scientific and Statistical Computing 7, 856 (1986).

[27] X. C. Cai, W. D. Gropp, D. E. Keyes, R. G. Melvin, and D. P. Young, "Parallel Newton-Krylov-Schwarz algorithms for the transonic full potential equation," Siam Journal on Scientific Computing 19, 246 (1998).

[28] Y. Sakiyama, and D. B. Graves, "Neutral gas flow and ring-shaped emission profile in non-thermal RF-excited plasma needle discharge at atmospheric pressure," Plasma Sources Science and Technology 18, 025022 (2009)

[29] M. J. Kushner, "Modelling of microdischarge devices - plasma and gas dynamics," Journal of Physics D: Applied Physics 38, 1633 (2005).

[30] G. K. Grubert, M. M. Becker, and D. Loffhagen, "Why the local-mean-energy approximation should be used in hydrodynamic plasma descriptions instead of the

local-field approximation," Physics Review E 80, 036405 (2009).

[31] G. J. M. Hagelaar, and L. C. Pitchford, "Solving the Boltzmann equation to obtain electron transport coefficients and rate coefficients for fluid models," Plasma Sources Science and Technology 14, 722 (2005).

[32] R. J. Leveque, "Finite-Volume Methods for Hyperbolic Problems, Cambridge University Press, Cambridge, 2002.

[33] D. L. Scharfetter, and H. K. Gummel, IEEE Trans. Electron Devices 16, 64 (1969).

[34] Balay S, Buschelman K, Gropp W D, Kaushik D, Knepley M G, McInnes L C, Smith B F and Zhang H, PETSc library, http://www.mcs.anl.gov/petsc 2011.

[35] Y. Saad, Iterative Methods for Sparse Linear Systems, 2nd ed., pp. 453, (Society for Industrial and Applied Mathematics, Philadelphia, 2003).

[36] M. H. Hu, J. S. Wu, and Y. S. Chen, "Development of a parallelized 2D/2D-axisymmetric Navier-Stokes equation solver for all-speed gas flows," Computers and Fluids 45, 241 (2011).

[37] A. P. Papadakis, G. E. Georghiou, A. C. Metaxas, "Simulation for the transition from non-thermal to thermal discharges," Plasma Sources Science and Technology 14, 250 (2005).

[38] J. P. Boeuf, and L. C. Pitchford, "Electrohydrodynamic force and aerodynamic flow acceleration in surface dielectric barrier discharge," Journal of Applied Physics 97, 103307 (2005).

[39] M. H. Chiang, K. C. Liao, I. M. Lin, C. C. Lu, H. Y. Huang, C. L. Kuo, J. S. Wu., C. C. Hsu, and S. H. Chen, "Effects of Oxygen Addition and Treating Distance on Surface Cleaning of ITO glass by a Non-Equilibrium Nitrogen Atmospheric-Pressure Plasma Jet," Plasma Chem. Plasma Process. 30, 553 (2010).

[40] T. Martens, A. Bogaerts, W. Brok, and J. V. Dijk, "Computer simulations of a

dielectric barrier discharge used for analytical spectrometry," Analytical and Bioanalytical Chemistry 388, 1583 (2007).

[41] D. Lee, J. M. Park, S. H. Hong, and Y. Kim, "Numerical simulation on mode transition of atmospheric dielectric barrier discharge in helium-oxygen mixture," IEEE Trans. Plasma Sci. **33**, 949 (2005).

[42] F. Tochikubo, S. Uchida, H. Yasui, and K. Sato, "Numerical Simulation of NO Oxidation in Dielectric Barrier Discharge with Microdischarge Formation," Jpn. J. Appl. Phys. **48**, 076507 (2009)

[43] X. H. Yuan, and L. L. Raja, "Computational study of capacitively coupled high-pressure glow discharges in helium," IEEE Trans. Plasma Sci. **31**, 495 (2003)

[44] T. Martens, A. Bogaerts, W. J. M. Brok, and J. V. Dijk, "The dominant role of impurities in the composition of high pressure noble gas plasmas," Appl. Phys. Lett. **92**, 041504 (2008).

[45] I. A. Kossyi, A. Y. Kostinsky, A. A. Matveyev, and V. P. Silakov, "Kinetic scheme of the non-equilibrium discharge in nitrogen-oxygen mixtures," Plasma Sources Sci. Technol. **1**, 207 (1992).

[46] M. Capitelli, C. M. Ferreira, B. F. Gordiets, and A. I. Osipov, Plasma Kinetics in Atmospheric Gases, Springer, **2000**, pp. 157.

[47] D. X. Liu, P. Bruggeman, F. Iza, M. Z. Rong, and M. G. Kong, "Global model of low-temperature atmospheric-pressure He + H(2)O plasmas," Plasma Sources Science and Technology 19, 025018 (2010).

[48] L. Mangolini, C. Anderson, J. Heberlein, and U. Kortshagen, J. Phys. D: Appl. Phys. **37**, 1021 (2004).

[49] J. Waskoenig, K. Niemi, N. Knake, L. M. Graham, S. Reuter, V. Schulz-von der Gathen, and T. Gans, Plasma Sources Sci. Technol. **19**, 045018 (2010)

[50] H. W. Ellis, R. Y. Pai, and E. W. McDaniel, At. Data Nucl. Data Tables, **17**, 177

(1976).

[51] L. A. Viehland, and E. A. Mason, At. Data Nucl. Data Tables, **60**, 37 (1995).

[52] H. W. Ellis, E. W. McDaniel, D. L. Albritton, L. A. Viehland, S. L. Lin, and E. A. Mason, "Transport Properties of Gaseous Ions Over a Wide Energy Range Part II," Atomic Data and Nuclear Data Tables 22, 179 (1978).

[53] A. V. Ivanov, S. Trakhtenberg, A. K. Bertram, Y. M. Gershenzon, and M. J. Molina, "OH, HO_2, and Ozone Gaseous Diffusion Coefficients," J. Phys. Chem. A 111, 1632 (2007).

[54] R. B. Bird, W. E. Stewart, and E. N. Lightfoot, Transport Phenomena, pp. 525, (John Wiley & Sons, New York, 2007).

[55] B. E. Poling, J. M. Prausnitz, and J. P. O'Connell, The Properties of Gases and Liquids, pp. B1, (McGraw-Hill, New York, 2001).

[56] D. Dobrynin, G. Fridman, Y. V. Mukhin, M. A. Wynosky-Dolfi, J. Rieger, R. F. Rest, A. F. Gutsol, and A. Fridman, "Cold Plasma Inactivation of Bacillus cereus and Bacillus anthracis (Anthrax) Spores, IEEE Trans. On Plasma Science 38, 1878 (2010).

[57] F. Sohbatzadeh, A. H. Colagar, S. Mirzanejhad, and S. Mahmodi, "E. coli, P. aeruginosa, and B. cereus Bacteria Sterilization Using Afterglow of Non-Thermal Plasma," Appl. Biochem. Biotechnol. 160, 1978 (2010).

[58] H. F. Mark, D. F. Othmer, and C. G. Overberger, Encyclopedia of chemical technology, vol. 11, 3rd ed., pp. 14, (Wiley, New York, 1978).

[59] K. M. Lin, C. T. Hung, F. N. Hwang, M. R. Smith, Y. W. Yang, and J. S. Wu, "Development of a Parallel Semi-Implicit Two-Dimensional Plasma Fluid Modeling Code Using Finite-Volume Method," Comput. Phys. Commun. **183**, 1225 (2012), DOI: 10.1016/j.cpc.2012.02.001

[60] J. P. Lim, H. S. Uhm, and S. Z. Li, "Atmospheric-pressure argon/oxygen plasma-discharge source with a stepped electrode", Applied Physics Letters 90,

051504 (2007).

[61] J. L. Walsh, F. Iza, N. B. Janson, V. J. Law, and M. G. Kong, “Three distinct modes in a cold atmospheric pressure plasma jet,” Journal of Physics D-Applied Physics 43, 075201 (2010).

Tables

Table 1-1 Classification of plasmas with their temperatures [3].

Low-temperature plasma (LTP)		High-temperature plasma (HTP)
Thermal LTP	Nonthermal LTP	
$T_e \approx T_i \approx T \lesssim 2 \times 10^4$ K	$T_i \approx T \approx 300$ K $T_i \ll T_e \lesssim 10^5$ K	$T_i \approx T_e \gtrsim 10^7$ K
e.g., arc plasma at normal pressure	e.g., low-pressure glow discharge	e.g., fusion plasmas

Table 3-1 Measured impurities of helium gas in Taiwan using a gas chromatographer.

	O_2 (ppm)	N_2 (ppm)
Bottle 1	5.57	23.66
Bottle 2	7.07	16.09
Bottle 3	8.26	26.02
Average	6.97	21.92

Table 3-2 Summary of helium plasma chemistry considering impurities

No	Reaction channels	Rate constant or cross- section	Threshold (eV)	Ref.
R00	$e + He \rightarrow e + He$	BOLSIG+	0	40
R01	$e + He \rightarrow e + He_m^*$	BOLSIG+	19.82	40
R02	$e + He \rightarrow e + He_m^*$	BOLSIG+	20.61	40
R03	$e + He \rightarrow e + He_{ex}^*$	BOLSIG+	20.96	40
R04	$e + He \rightarrow e + He_{ex}^*$	BOLSIG+	21.21	40
R05	$e + He \rightarrow e + He_{ex}^*$	BOLSIG+	22.97	40
R06	$e + He \rightarrow e + He_{ex}^*$	BOLSIG+	23.7	40
R07	$e + He \rightarrow e + He_{ex}^*$	BOLSIG+	24.02	40
R08	$e + He \rightarrow 2e + He^+$	BOLSIG+	24.58	40
R09	$e + He_m^* \rightarrow 2e + He^+$	BOLSIG+	4.78	40
R10	$e + He_m^* \rightarrow e + He$	2.9×10^{-15} m^3 s^{-1}	-19.8	40
R11	$e + He_2^* \rightarrow e + 2He$	3.8×10^{-15} m^3 s^{-1}	-17.9	40
R12	$He^+ + 2e \rightarrow e + He_m^*$	6×10^{-32} m^6 s^{-1}	-4.78	40
R13	$He_2^+ + 2e \rightarrow He_m^* + He + e$	2.8×10^{-32} m^6 s^{-1}	0	40
R14	$He_2^+ + e + He \rightarrow He_m^* + 2He$	3.5×10^{-39} m^6 s^{-1}	0	40
R15	$He_2^+ + 2e \rightarrow He_2^* + e$	1.2×10^{-33} m^6 s^{-1}	0	40
R16	$He_2^+ + e + He \rightarrow He_2^* + He$	1.5×10^{-39} m^6 s^{-1}	0	40
R17	$He_{ex}^* + He \rightarrow He_2^+ + e$	1.5×10^{-17} m^3 s^{-1}	0	40
R18	$He_m^* + He_m^* \rightarrow He_2^+ + e$	2.03×10^{-15} m^3 s^{-1}	-18.2	40
R10	$He_m^* + He_m^* \rightarrow He^+ + He + e$	8.7×10^{-16} m^3 s^{-1}	-15.8	40
R20	$He^+ + 2He \rightarrow He_2^+ + He$	6.5×10^{-44} m^6 s^{-1}	0	40

R21	$He_m^* + 2He \rightarrow He_2^* + He$	1.9×10^{-46} m^6 s^{-1}	0	40
R22	$He_m^* + He_2^* \rightarrow He^+ + 2He + e$	5×10^{-16} m^3 s^{-1}	-13.5	40
R23	$He_m^* + He_2^* \rightarrow He_2^+ + He + e$	2×10^{-15} m^3 s^{-1}	-15.9	40
R24	$He_2^* + He_2^* \rightarrow He^+ + 3He + e$	3×10^{-16} m^3 s^{-1}	-11.3	40
R25	$He_2^* + He_2^* \rightarrow He_2^+ + 2He + e$	1.2×10^{-15} m^3 s^{-1}	-13.7	40
R26	$He_2^* + He \rightarrow 3He$	4.9×10^{-22} m^3 s^{-1}	0	40
R27	$e + O_2 \rightarrow e + O_2$	BOLSIG+	0	41
R28	$e + O_2 \rightarrow 2e + O_2^+$	BOLSIG+	12.06	41
R29	$e + 2O_2 \rightarrow O_2^- + O_2$	BOLSIG+	0	41
R30	$O_3 + O \rightarrow 2O_2$	8.3×10^{-21} m^3 s^{-1}	0	41
R31	$e + O_2^+ \rightarrow 2O$	4.8×10^{-13} m^3 s^{-1}	0	41
R32	$O^+ + O_2 \rightarrow O_2^+ + O$	2.0×10^{-17} m^3 s^{-1}	0	41
R33	$He_m^* + O_2 \rightarrow e + O_2^+ + He$	2.4×10^{-16} m^3 s^{-1}	0	41
R34	$He_m^* + O \rightarrow e + O^+ + He$	4.3×10^{-16} m^3 s^{-1}	0	41
R35	$2O + He \rightarrow He + O_2$	1.04×10^{-45} m^6 s^{-1}	0	41
R36	$O + He + O_2 \rightarrow O_3 + He$	6.27×10^{-46} m^6 s^{-1}	0	41
R37	$O_3 + He \rightarrow O + He + O_2$	2.28×10^{-32} m^3 s^{-1}	0	41
R38	$e + O_2 \rightarrow O + O^-$	BOLSIG+	0	42
R39	$e + O_2 \rightarrow e + O_2(a)$	BOLSIG+	0.977	42
R40	$e + O_2 \rightarrow e + 2O$	BOLSIG+	6.0	42
R41	$e + O_2 \rightarrow e + O + O(^1D)$	BOLSIG+	8.4	42
R42	$e + O_2 \rightarrow e + O + O(^1S)$	BOLSIG+	10.0	42
R43	$He_m^* + N_2 \rightarrow e + N_2^+ + He$	7.0×10^{-17} m^3 s^{-1}	0	43
R44	$He_2^* + N_2 \rightarrow e + N_2^+ + 2He$	7.0×10^{-17} m^3 s^{-1}	0	43

R45	$He^+ + N_2 \rightarrow N_2^+ + He$	5.0×10^{-16} m^3 s^{-1}	0	43
R46	$He^+ + N_2 \rightarrow N^+ + N + He$	7.0×10^{-16} m^3 s^{-1}	0	43
R47	$He_2^+ + N_2 \rightarrow N_2^+ + 2He$	5.0×10^{-16} m^3 s^{-1}	0	43
R48	$He_2^+ + N_2 \rightarrow N^+ + N + 2He$	7.0×10^{-16} m^3 s^{-1}	0	43
[a]R49	$2e + N_2^+ \rightarrow e + N_2$	$5.651\times10^{-39} T_e^{-0.8}$ m^6 s^{-1}	0	43
[a]R50	$e + N_2^+ \rightarrow 2N$	$2.540\times10^{-12} T_e^{-0.5}$ m^3 s^{-1}	0	43
[a]R51	$e + N_2 \rightarrow e + 2N$	$1.959\times10^{-12} T_e^{-0.7} \exp\left(-\frac{1.132\times10^5}{T_e}\right)$ m$^3 s^{-1}$	9.757	43
[a]R52	$e + N \rightarrow 2e + N^+$	$8.401\times10^{-11} \exp\left(-\frac{1.682\times10^5}{T_e}\right)$ m$^3 s^{-1}$	14.5	43
R53	$e + N_2 \rightarrow e + N_2$	BOLSIG+	0.0	42
R54	$e + N_2 \rightarrow 2e + N_2^+$	BOLSIG+	15.581	42
R55	$e + N_2 \rightarrow e + N_2(A^3\Sigma_u^+)$	BOLSIG+	6.169	42
R56	$e + N_2 \rightarrow e + N_2(B^3\Pi_g)$	BOLSIG+	7.353	42
R57	$e + N_2 \rightarrow e + N_2(C^3\Pi_u)$	BOLSIG+	11.032	42
R58	$e + N_2 \rightarrow e + N_2(a'^1\Sigma_u^-)$	BOLSIG+	8.399	42
[a]R59	$e + N_4^+ \rightarrow 2N_2$	$2.0\times10^{-12}\left(\frac{T_g}{T_e}\right)^{0.5}$ m$^3 s^{-1}$	0.0	44
R60	$N_2^+ + 2N_2 \rightarrow N_4^+ + N_2$	1.9×10^{-41} m^6 s^{-1}	0.0	44
R61	$N_2^+ + He + N_2 \rightarrow N_4^+ + He$	1.9×10^{-41} m^6 s^{-1}	0.0	44
R62	$N_4^+ + N_2 \rightarrow N_2^+ + 2N_2$	2.5×10^{-21} m^3 s^{-1}	0.0	44
R63	$N_4^+ + He \rightarrow N_2^+ + He + N_2$	2.5×10^{-21} m^3 s^{-1}	0.0	44
R64	$N_2(A^3\Sigma_u^+) + N_2(a'^1\Sigma_u^-) \rightarrow e + N_4^+$	5.0×10^{-17} m^3 s^{-1}	0.0	45
R65	$2N_2(a'^1\Sigma_u^-) \rightarrow e + N_4^+$	2.0×10^{-16} m^3 s^{-1}	0.0	45
R66	$e + N_2^+ \rightarrow N(^2D) + N$	3.7×10^{-13} m^3 s^{-1}	0.0	42
R67	$e + O_2^+ \rightarrow O + O(^1D)$	2.1×10^{-13} m^3 s^{-1}	0.0	42

R68	$O_2^+ + O_2^- \rightarrow 2O_2$	7.8×10^{-12} m^3 s^{-1}	0.0	42
R69	$O^- + N_2^+ \rightarrow O + N_2$	7.8×10^{-12} m^3 s^{-1}	0.0	42
R70	$O_2^+ + O^- \rightarrow O + O_2$	7.5×10^{-12} m^3 s^{-1}	0.0	42
R71	$O_2^- + O_2(a) \rightarrow e + 2O_2$	2.0×10^{-16} m^3 s^{-1}	0.0	42
R72	$O_2^- + N_2(A^3\Sigma_u^+) \rightarrow e + O_2 + N_2$	2.1×10^{-15} m^3 s^{-1}	0.0	42
R73	$O_2^- + N_2(B^3\Pi_g) \rightarrow e + O_2 + N_2$	2.5×10^{-15} m^3 s^{-1}	0.0	45
R74	$O^- + O_2(a) \rightarrow e + O_3$	3.0×10^{-16} m^3 s^{-1}	0.0	45
R75	$O^- + N_2(A^3\Sigma_u^+) \rightarrow e + O + N_2$	2.2×10^{-15} m^3 s^{-1}	0.0	42
R76	$O^- + N_2(B^3\Pi_g) \rightarrow e + O + N_2$	1.9×10^{-15} m^3 s^{-1}	0.0	45
R77	$O_2^- + O \rightarrow e + O_3$	1.5×10^{-16} m^3 s^{-1}	0.0	42
R78	$O^- + O \rightarrow e + O_2$	5.0×10^{-16} m^3 s^{-1}	0.0	42
R79	$O^- + N \rightarrow e + NO$	2.6×10^{-16} m^3 s^{-1}	0.0	42
R80	$O^- + O_2 \rightarrow e + O_3$	5.0×10^{-21} m^3 s^{-1}	0.0	45
R81	$O + N + N_2 \rightarrow NO + N_2$	$1.76\times10^{-43}\times T_g^{-0.5}$ m^6 s^{-1}	0.0	45
R82	$O + O_2 + N_2 \rightarrow O_3 + N_2$	5.6×10^{-46} m^6 s^{-1}	0.0	42
R83	$N_2(A^3\Sigma_u^+) + O_2 \rightarrow 2O + N_2$	1.7×10^{-18} m^3 s^{-1}	0.0	42
R84	$N_2(A^3\Sigma_u^+) + O_2 \rightarrow O_2(a) + N_2$	7.5×10^{-19} m^3 s^{-1}	0.0	42
R85	$O + N_2(A^3\Sigma_u^+) \rightarrow NO + N(^2D)$	7.0×10^{-19} m^3 s^{-1}	0.0	42
R86	$O + N_2(A^3\Sigma_u^+) \rightarrow O(^1S) + N_2$	2.3×10^{-17} m^3 s^{-1}	0.0	42
R87	$N_2(B^3\Pi_g) + N_2 \rightarrow N_2(A^3\Sigma_u^+) + N_2$	3.0×10^{-17} m^3 s^{-1}	0.0	42
R88	$N_2(B^3\Pi_g) + O_2 \rightarrow 2O + N_2$	1.1×10^{-16} m^3 s^{-1}	0.0	42
R89	$N_2(a'^1\Sigma_u^-) + O_2 \rightarrow 2O + N_2$	2.8×10^{-17} m^3 s^{-1}	0.0	42
R90	$NO + N_2(a'^1\Sigma_u^-) \rightarrow O + N + N_2$	3.6×10^{-16} m^3 s^{-1}	0.0	42
R91	$N_2(C^3\Pi_u) + N_2 \rightarrow N_2(a'^1\Sigma_u^-) + N_2$	1.0×10^{-17} m^3 s^{-1}	0.0	42
R92	$N_2(C^3\Pi_u) + O_2 \rightarrow O + O(^1S) + N_2$	3.0×10^{-16} m^3 s^{-1}	0.0	42

R93	$N(^2D) + O_2 \rightarrow O + NO$	$1.5\times10^{-18}\times(T_g/300)^{0.5}$ m^3 s^{-1}	0.0	45
R94	$N(^2D) + O_2 \rightarrow O(^1D) + NO$	6.0×10^{-18} m^3 s^{-1}	0.0	42
R95	$O(^1D) + O_2 \rightarrow O + O_2(a)$	3.4×10^{-17} m^3 s^{-1}	0.0	42
R96	$O(^1D) + O_2 \rightarrow O + O_2$	$6.4\times10^{-18}\times\exp(67/T_g)$ m^3 s^{-1}	0.0	45
R97	$N_2(a'^1\Sigma_u^-) \rightarrow N_2 + h\nu(177nm)$	1.0×10^{2} s^{-1}	0.0	46
R98	$N_2(A^3\Sigma_u^+) \rightarrow N_2 + h\nu(293nm)$	0.5 s^{-1}	0.0	46
R99	$N_2(B^3\Pi_g) \rightarrow N_2(A^3\Sigma_u^+) + h\nu(1045nm)$	1.34×10^{5} s^{-1}	0.0	46
R100	$N_2(C^3\Pi_u) \rightarrow N_2(B^3\Pi_g) + h\nu(336nm)$	2.45×10^{7} s^{-1}	0.0	46
R101	$e + H_2O \rightarrow e + H_2O$	Cross Section	0.0	47
R102	$e + H_2O \rightarrow 2e + H_2O^+$	Cross Section	12.61	47
R103	$e + H_2O \rightarrow H + OH + e$	Cross Section	7.0	47
R104	$e + H_2O \rightarrow H_2 + O(^1D) + e$	Cross Section	7.4	47
R105	$e + H_2O \rightarrow H + OH(A) + e$	Cross Section	9.15	47
[b]R106	$e + O \rightarrow e + O(^1D)$	$4.5\times10^{-15}\times\exp(-2.29/T_e)$ m^3 s^{-1}	0.0	47
[b]R107	$e + OH \rightarrow e + O + H$	$2.08\times10^{-13}\times T_e^{-0.76}\times\exp(-6.9/T_e)$ m^3 s^{-1}	0.0	47
R108	$OH^+ + H_2O \rightarrow H_3O^+ + O$	1.3×10^{-15} m^3 s^{-1}	0.0	47
R109	$H_2O^+ + H_2O \rightarrow H_3O^+ + OH$	1.85×10^{-15} m^3 s^{-1}	0.0	47
R110	$H_3O^+ + H_2O + M \rightarrow H_5O_2^+ + M$	$3.2\times10^{-39}\times(T_g/300)^{-4}$ m^6 s^{-1}	0.0	47
R111	$H_5O_2^+ + H_2O + M \rightarrow H_7O_3^+ + M$	$7.4\times10^{-39}\times(T_g/300)^{-7.5}$ m^6 s^{-1}	0.0	47
R112	$H_7O_3^+ + H_2O + M \rightarrow H_9O_4^+ + M$	$2.5\times10^{-39}\times(T_g/300)^{-8.1}$ m^6 s^{-1}	0.0	47
R113	$H_9O_4^+ + M \rightarrow H_7O_3^+ + H_2O + M$	$2.0\times10^{12}\times T_g^{-8.1}\times\exp(-8360/T_g)$ m^3 s^{-1}	0.0	47
R114	$He_m^* + H_2O \rightarrow He + H_2O^+ + e$	6.6×10^{-16} m^3 s^{-1}	0.0	47
R115	$He_m^* + H_2O \rightarrow He + OH^+ + H + e$	1.5×10^{-16} m^3 s^{-1}	0.0	47
R116	$He_m^* + H_2O_2 \rightarrow He + OH^+ + OH + e$	7.8×10^{-16} m^3 s^{-1}	0.0	47

R117	$He_2^* + H_2O \rightarrow H_2O^+ + 2He + e$	6.0×10^{-16} m^3 s^{-1}	0.0	47
R118	$He + O(^1D) \rightarrow O + He$	1.0×10^{-19} m^3 s^{-1}	0.0	47
R119	$2OH \rightarrow H_2O_2$	$1.5\times10^{-17}\times(T_g/300)^{-0.37}$ m^6 s^{-1}	0.0	47
R120	$OH(A) \rightarrow OH + h\nu(306.4nm)$	1.25×10^{6} s^{-1}	0.0	47

[a]T_e is the electron temperature in Kevin;

[b]T_e is the electron temperature in eV;

T_g is the background temperature in Kevin.

Table 4-1 Averaged iteration number per time step of equations with sub-domain of ASM preconditioner solved by ILU and LU methods for small problem case (501 ×310 cells).

Poisson			Electron		
CPU	**ILU**	**LU**	**CPU**	**ILU**	**LU**
2	167.4	25.9	**2**	4.0	2.6
4	204.9	36.9	**4**	4.0	2.6
8	216.9	85.5	**8**	4.9	4.0
16	233.0	117.2	**16**	5.1	4.8
32	229.2	131.9	**32**	6.0	5.0
64	237.8	136.7	**64**	6.9	6.0
128	253.1	184.8	**128**	9.7	9.6
Neutral			**Te**		
CPU	**ILU**	**LU**	**CPU**	**ILU**	**LU**
2	2.0	2.0	**2**	8.5	4.4
4	2.0	2.0	**4**	8.5	4.3
8	2.0	2.0	**8**	10.0	7.9
16	2.0	2.0	**16**	11.4	9.2
32	2.0	2.0	**32**	13.5	11.7
64	2.0	2.0	**64**	15.6	13.6
128	2.1	2.4	**128**	24.6	24.5

Table 4-2 Averaged iteration number per time step of equations with sub-domain of ASM preconditioner solved by ILU and LU methods for large problem case (1001 ×620 cells).

Poisson			Electron		
CPU	**ILU**	**LU**	**CPU**	**ILU**	**LU**
2	311.0	32.9	**2**	4.9	3.0
4	339.7	48.7	**4**	4.9	3.0
8	400.8	94.2	**8**	5.9	4.7
16	292.6	137.9	**16**	6.4	5.3
32	349.0	169.5	**32**	8.4	7.1
64	402.4	172.2	**64**	9.1	8.0
128	373.4	213.5	**128**	11.5	10.0
Neutral			**Te**		
CPU	**ILU**	**LU**	**CPU**	**ILU**	**LU**
2	2.2	2.0	**2**	12.3	5.6
4	2.1	2.0	**4**	12.3	5.6
8	2.1	2.0	**8**	13.7	10.0
16	2.1	2.0	**16**	15.0	11.5
32	2.1	2.0	**32**	19.5	16.1
64	2.1	2.0	**64**	22.4	19.6
128	2.1	2.0	**128**	29.2	26.6

Table 4-3 The parallel performance of different level of overlapping ASM preconditioner with sub-domain solved by ILU method on the large problem (1001 ×620 cells) (a) Averaged iteration number per time step of equations (b) The relative runtime per time step. “OL 1”, “OL 2”, and “OL 3” represent one-, two-, and three-level overlapping, respectively.

Poisson				Electron			
CPU	**OL1**	**OL2**	**OL3**	**CPU**	**OL1**	**OL2**	**OL3**
2	311.0	340.2	340.4	**2**	4.9	5.4	5.6
4	339.7	366.8	330.9	**4**	4.9	5.4	5.6
8	400.8	354.1	439.6	**8**	5.9	5.6	5.7
16	292.6	384.2	355.6	**16**	6.4	6.0	6.0
32	349.0	384.7	379.6	**32**	8.4	7.1	6.6
64	402.4	360.9	335.3	**64**	9.1	8.0	7.0
128	373.4	362.8	349.7	**128**	11.5	9.6	8.7
Neutral				**Te**			
CPU	**OL1**	**OL2**	**OL3**	**CPU**	**OL1**	**OL2**	**OL3**
2	2.2	2.2	2.1	**2**	12.3	12.9	13.2
4	2.1	2.2	2.1	**4**	12.3	12.9	13.2
8	2.1	2.1	2.1	**8**	13.7	13.0	13.4
16	2.1	2.1	2.1	**16**	15.0	13.8	13.8
32	2.1	2.2	2.2	**32**	19.5	16.7	15.3
64	2.1	2.2	2.2	**64**	22.4	19.0	17.1
128	2.1	2.2	2.6	**128**	29.2	24.0	20.4

(a)

CPU	**OL 1**	**OL 2**	**OL3**
2	1.00	1.13	1.84
4	1.00	1.08	1.00
8	1.00	0.91	1.10
16	1.00	1.24	1.18
32	1.00	1.12	1.19
64	1.00	1.07	1.06
128	1.00	1.14	1.30

(b)

Table 4-4 The parallel performance of different level of overlapping ASM preconditioner with sub-domain solved by LU method on the large problem (1001 ×620 cells) (a) Averaged iteration number per time step of equations (b) The relative runtime per time step. “OL 1”, “OL 2”, and “OL 3” represent one-, two-, and three-level overlapping, respectively.

Poisson				Electron			
CPU	**OL1**	**OL2**	**OL3**	**CPU**	**OL1**	**OL2**	**OL3**
2	32.9	29.1	24.7	**2**	3.0	2.8	2.0
4	48.7	40.9	31.7	**4**	3.0	2.5	2.0
8	94.2	85.2	77.8	**8**	4.7	4.0	3.1
16	137.9	117.6	98.7	**16**	5.3	4.1	3.6
32	169.5	149.0	132.5	**32**	7.1	5.6	4.9
64	172.2	144.5	128.6	**64**	8.0	6.1	5.1
128	213.5	205.0	155.2	**128**	10.0	8.0	7.9
Neutral				**Te**			
CPU	**OL1**	**OL2**	**OL3**	**CPU**	**OL1**	**OL2**	**OL3**
2	2.0	2.0	2.0	**2**	5.6	4.2	3.6
4	2.0	2.0	2.0	**4**	5.6	4.5	3.6
8	2.0	2.0	2.0	**8**	10.0	8.1	6.6
16	2.0	2.0	2.0	**16**	11.5	8.7	7.2
32	2.0	2.0	2.0	**32**	16.1	12.4	10.3
64	2.0	2.0	2.0	**64**	19.6	15.0	12.4
128	2.0	2.0	2.6	**128**	26.6	20.6	18.6

(a)

CPU	**OL 1**	**OL 2**	**OL3**
2	1.00	1.09	0.91
4	1.00	0.92	0.92
8	1.00	0.98	0.99
16	1.00	0.95	0.91
32	1.00	0.98	0.99
64	1.00	1.05	1.12
128	1.00	1.34	1.50

(b)

Table 5-1. Boundary conditions for the plasma fluid model. The symbols (*A*-*L*) correspond to the vertexes in Fig. 5-1.

	n_e	n_i	n_{uc}	n_ε	ϕ
Solid external domain					
ABC, *DEFG*, *HIJ*	$n_e = 0$	$n_i = 0$	$n_{uc} = 0$	$n_\varepsilon = 0$	$\frac{\partial \phi}{\partial x} = 0$ *or* $\frac{\partial \phi}{\partial y} = 0$
Flow outlet					
CD, *GH*	$\Gamma_e = 0$	$\Gamma_i = n_i v$	$\Gamma_{uc} = n_{uc} v$	$\Gamma_\varepsilon = 0$	$\frac{\partial \phi}{\partial y} = 0$
Flow inlet					
JA	$\Gamma_e = 0$	$\Gamma_i = 0$	$\Gamma_{uc} = 0$	$\Gamma_\varepsilon = 0$	$\frac{\partial \phi}{\partial x} = 0$
Solid-discharge interface					
ALC, *DG*, *JKH*	Eq. 2-13	Eq. 2-12	Eq. 2-14	Eq. 2-16	(a)

(a) $\varepsilon_{dielectric} \vec{E}_{dielectric} \cdot \hat{n} - \varepsilon_{discharge} \vec{E}_{discharge} \cdot \hat{n} = \sigma_f$ where $\hat{n}$ is the unit vector pointing to the wall. σ_f is the surface charge density on the dielectric, which is calculated from the charge species flux on the surface.

Table 5-2. Boundary conditions for the gas flow model. The symbols (*A*-*L*) correspond to the vertexes in Fig 5-1.

	u	v	P	T	Y
Solid external domain					
ABC, DEFG, HIJ	0	0	0	$\frac{\partial T}{\partial X_i}=0$	0
Flow outlet					
CD, GH	$\frac{\partial u}{\partial y}=0$	$\frac{\partial v}{\partial y}=0$	$P=760$ torr	$\frac{\partial T}{\partial y}=0$	$\frac{\partial Y}{\partial y}=0$
Flow inlet					
JA	$u=u_{ini}$ (a)	0	$P=P_{extrapolation}$ (b)	$T=300\ K$	$Y=Y_{ini}$ (a)
Solid-fluid interface					
ALC, DG, JKH	0	0	$\frac{\partial P}{\partial X_i}=0$	$k_f \frac{\partial T}{\partial X_i}\Big\vert_f = k_s \frac{\partial T}{\partial X_i}\Big\vert_s$	$\frac{\partial Y}{\partial X_i}=0$

(a) The initial velocity u_{ini} and species fraction Y_{ini} are calculated from the specified inlet flow conditions (30 SLM helium gas with 100 ppm nitrogen).

(b) $P_{extrapolation}$ is extrapolated linearly from the pressure of next two cells.

Figures

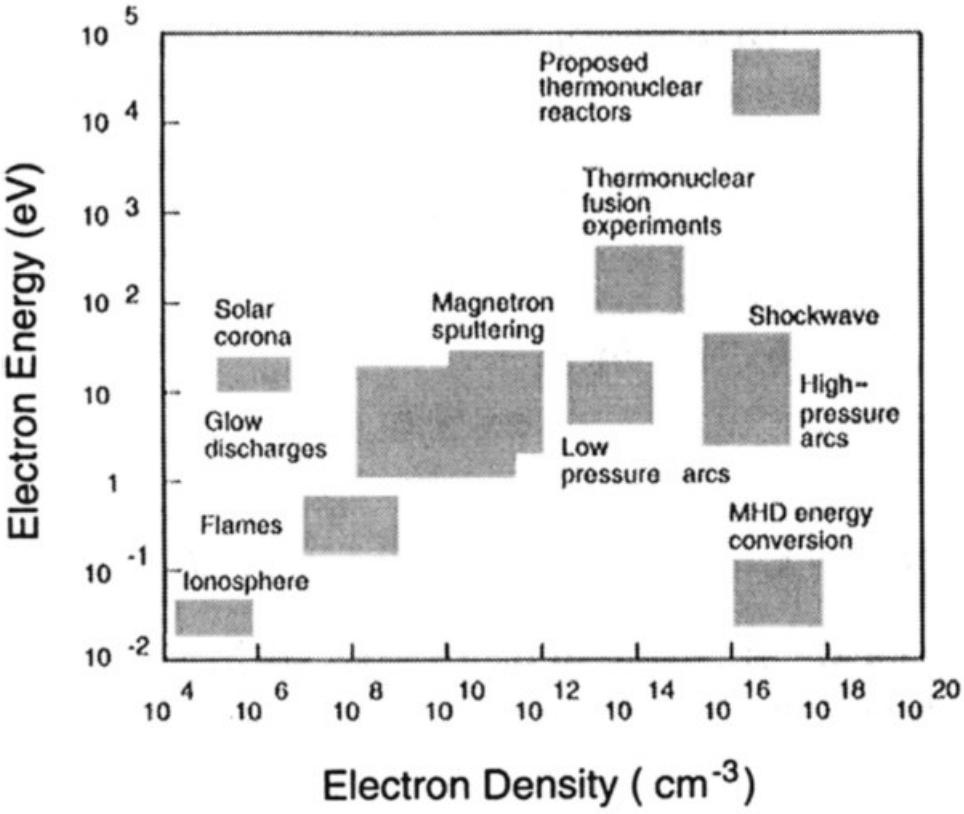

Fig. 1-1 Plasmas classified with the electron density and temperature.

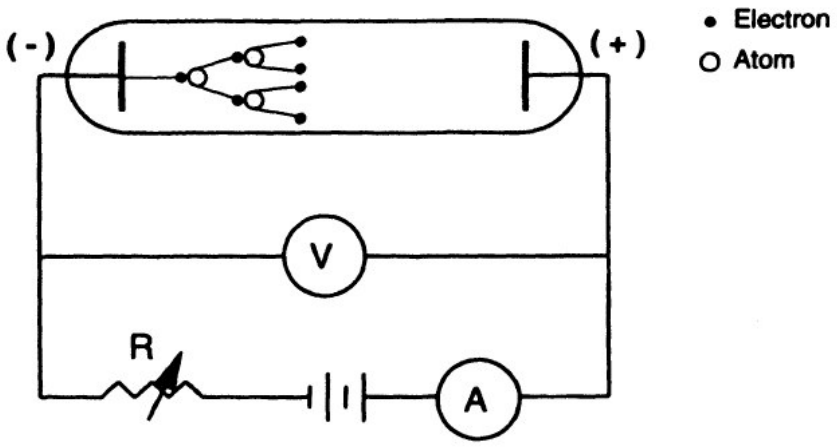

Fig. 1-2 The setup of direct current discharge

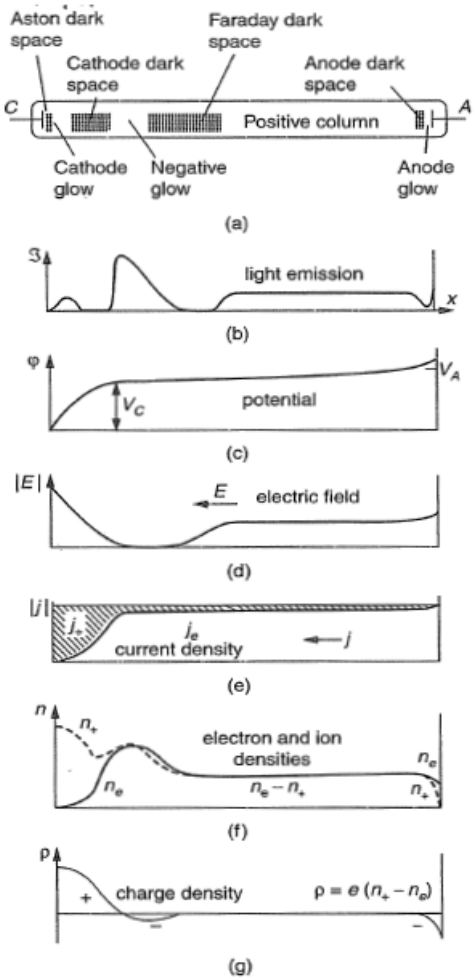

Fig. 1-3 Distributions of physical properties in a direct current discharge

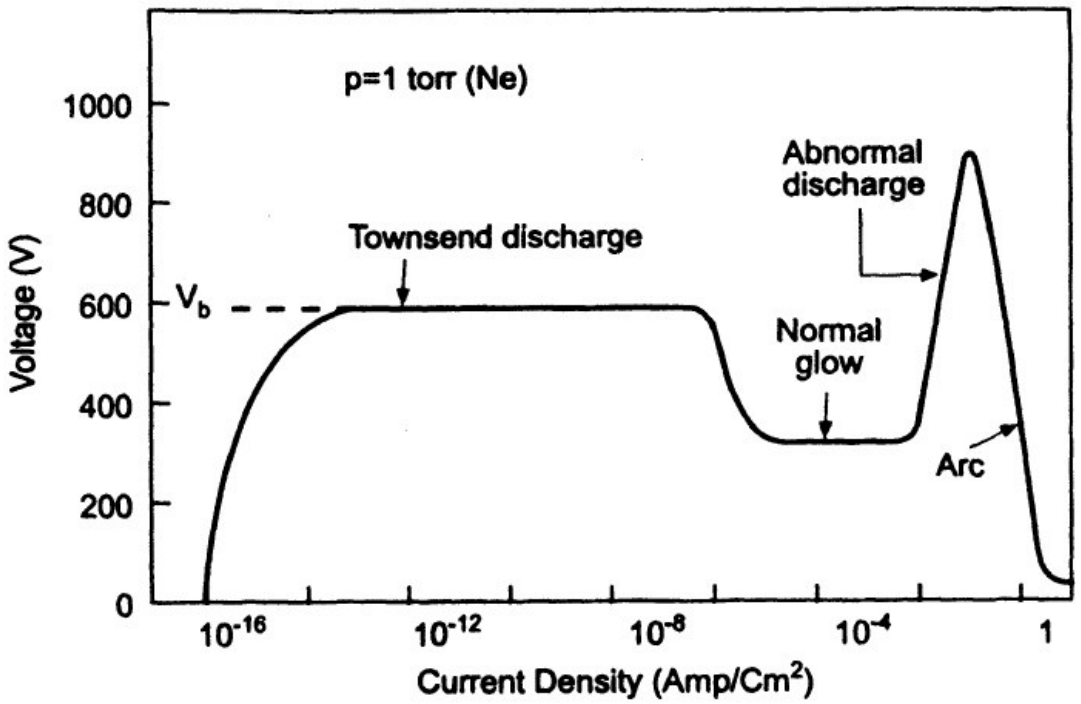

Fig. 1-4 The I-V characteristic of a direct current discharge

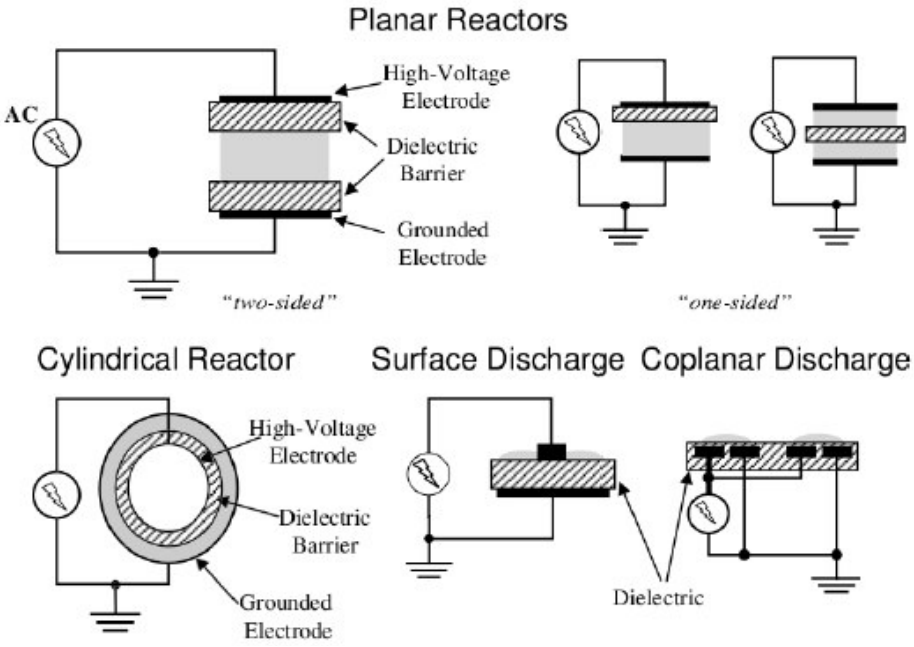

Fig. 1-5 Typical arrangements for electrodes and dielectrics in dielectric-barrier discharges.

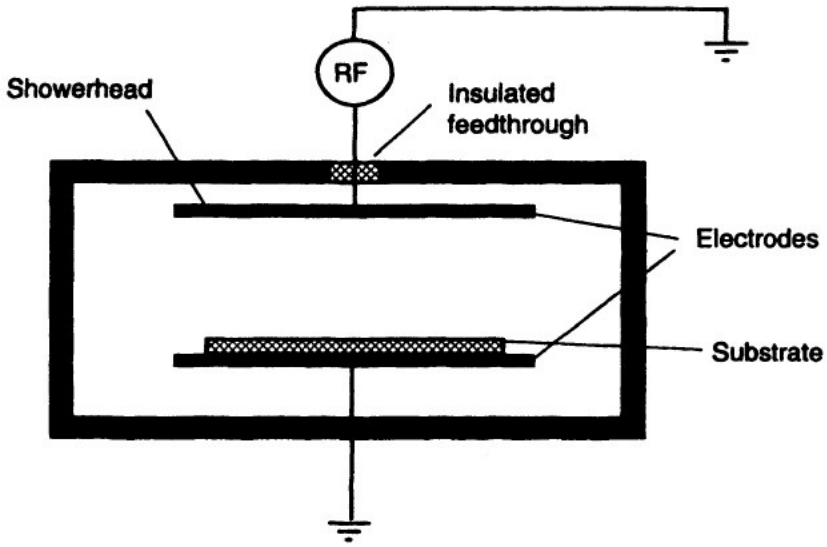

(a)

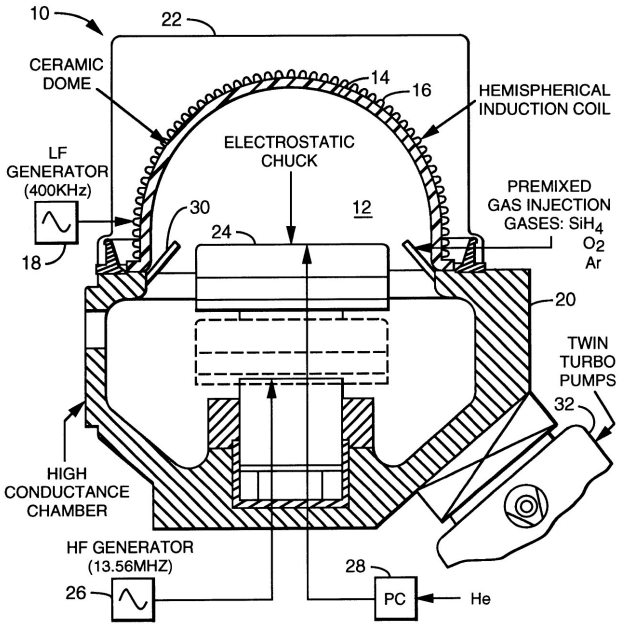

(b)

Fig. 1-6. Reactor of (a) capacitively coupled plasma (b) inductively coupled plasma

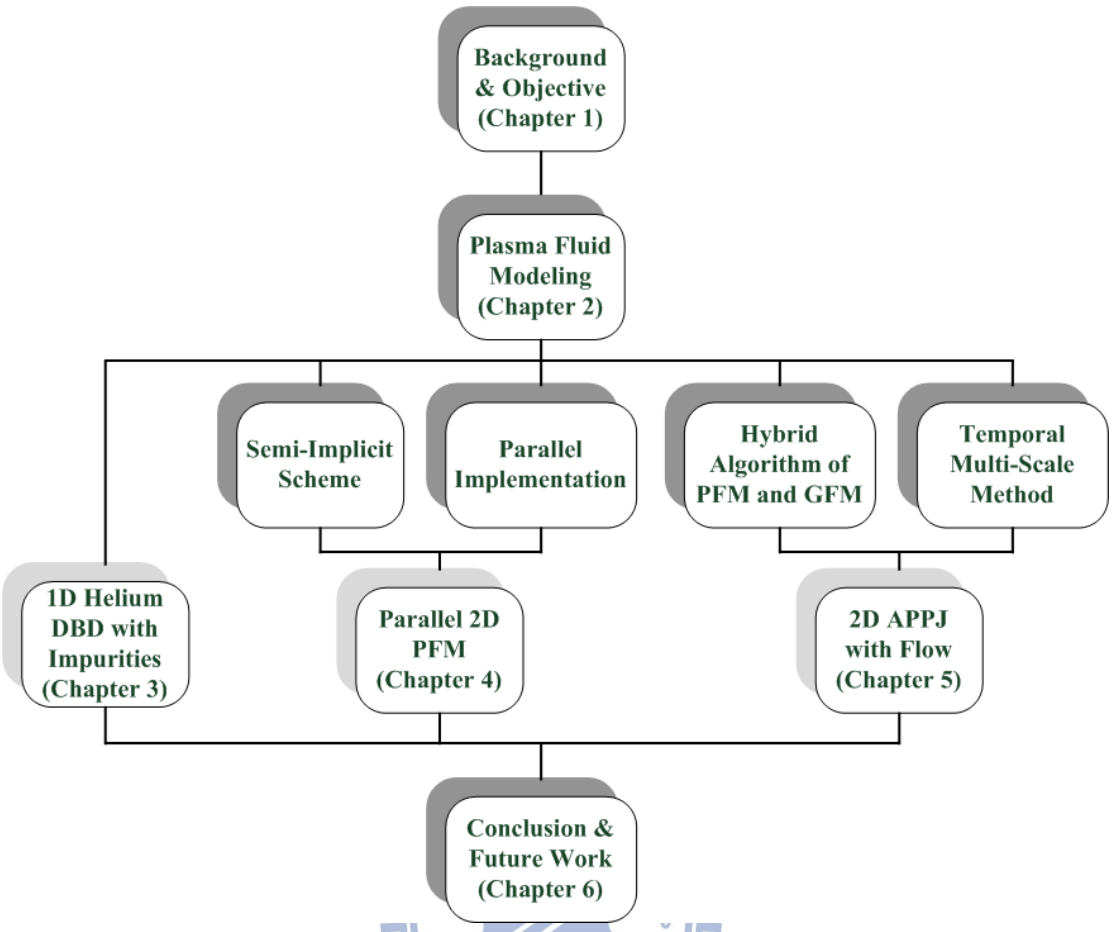

Fig. 1-7. Research structure of the thesis.

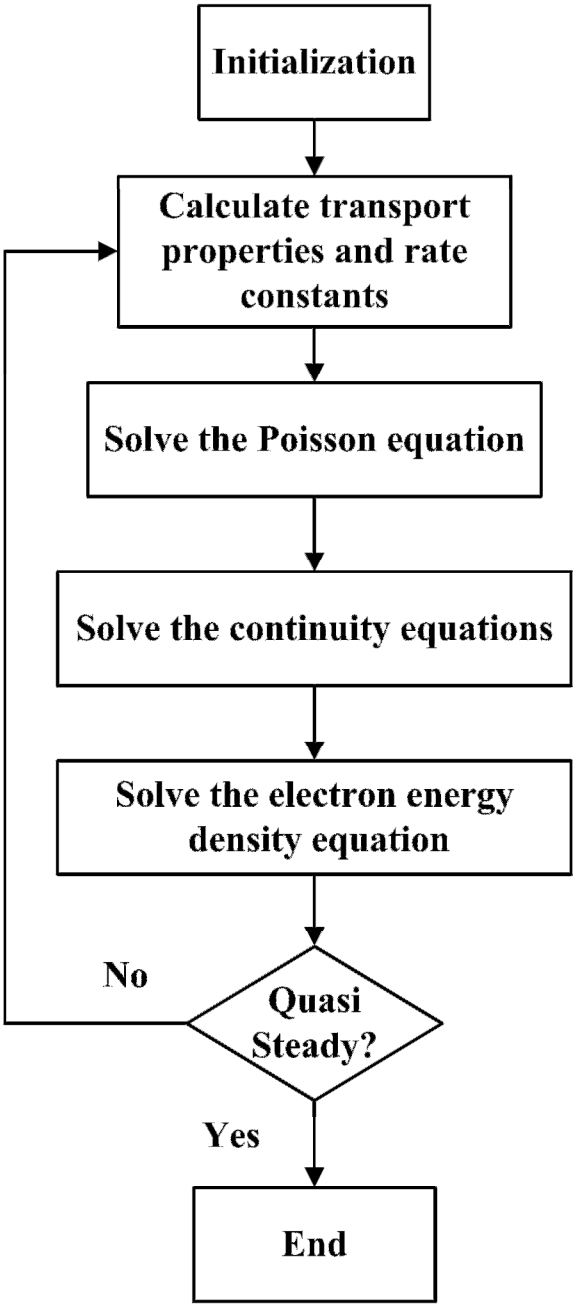

Fig. 2-1 Flowchart of fluid modeling simulation

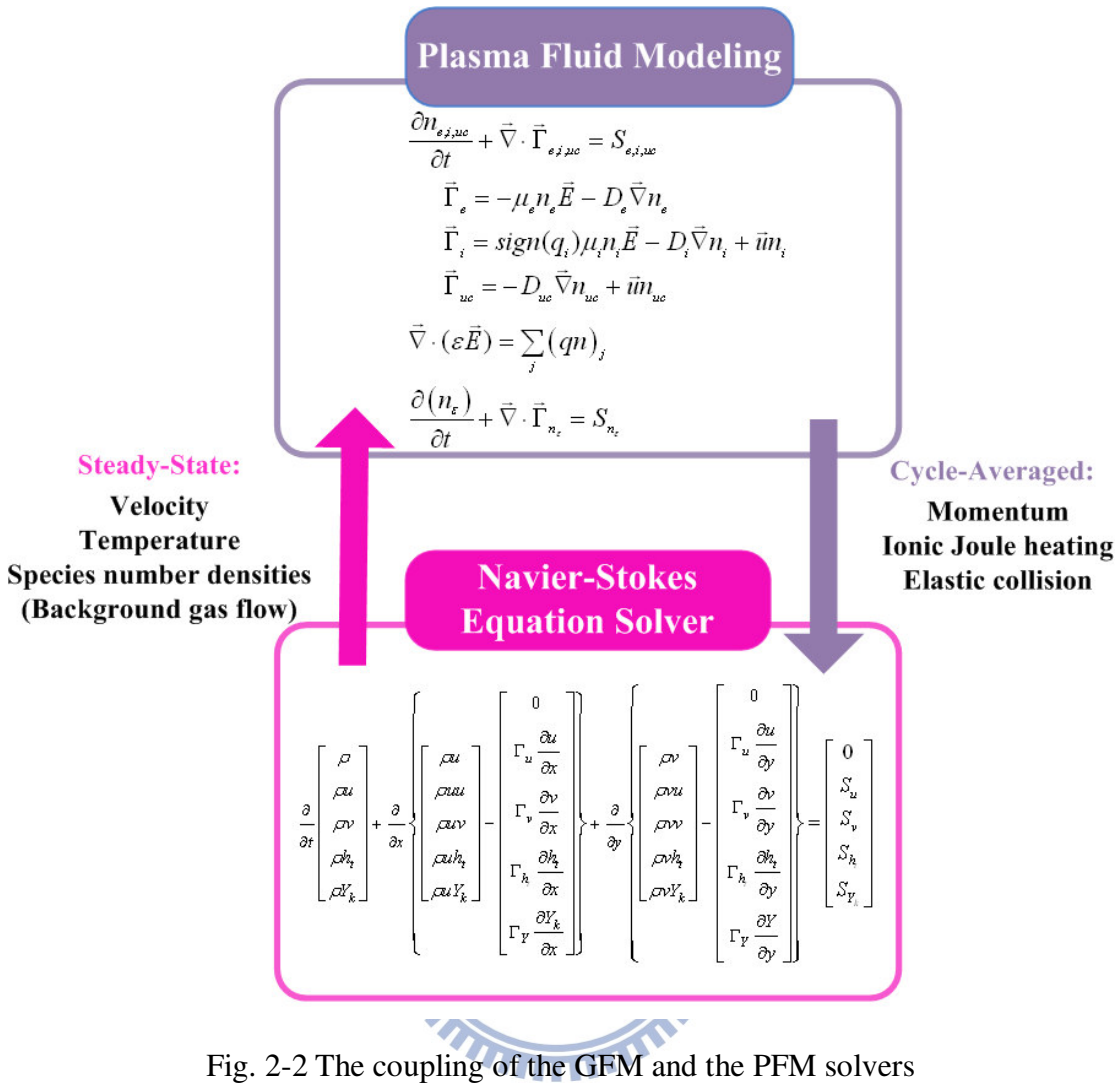

Fig. 2-2 The coupling of the GFM and the PFM solvers

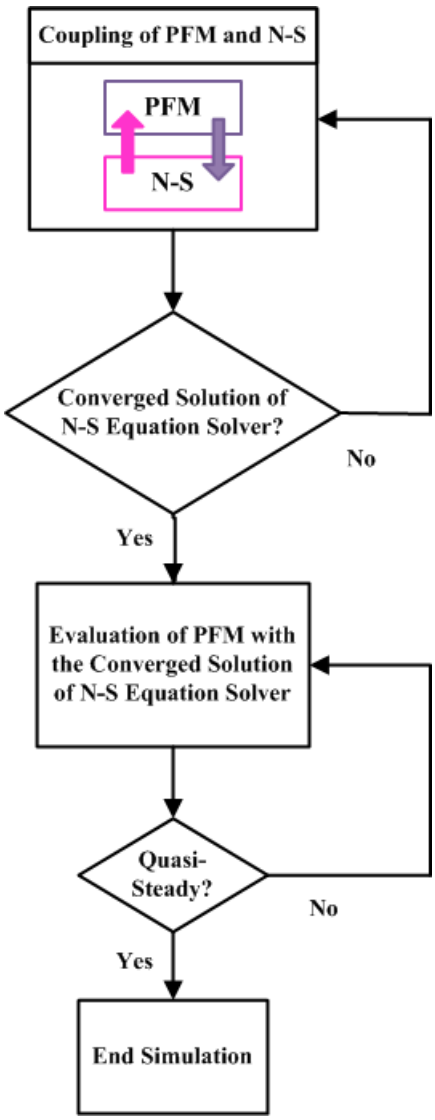

Fig. 2-3 The flowchart of complete APPJ simulation

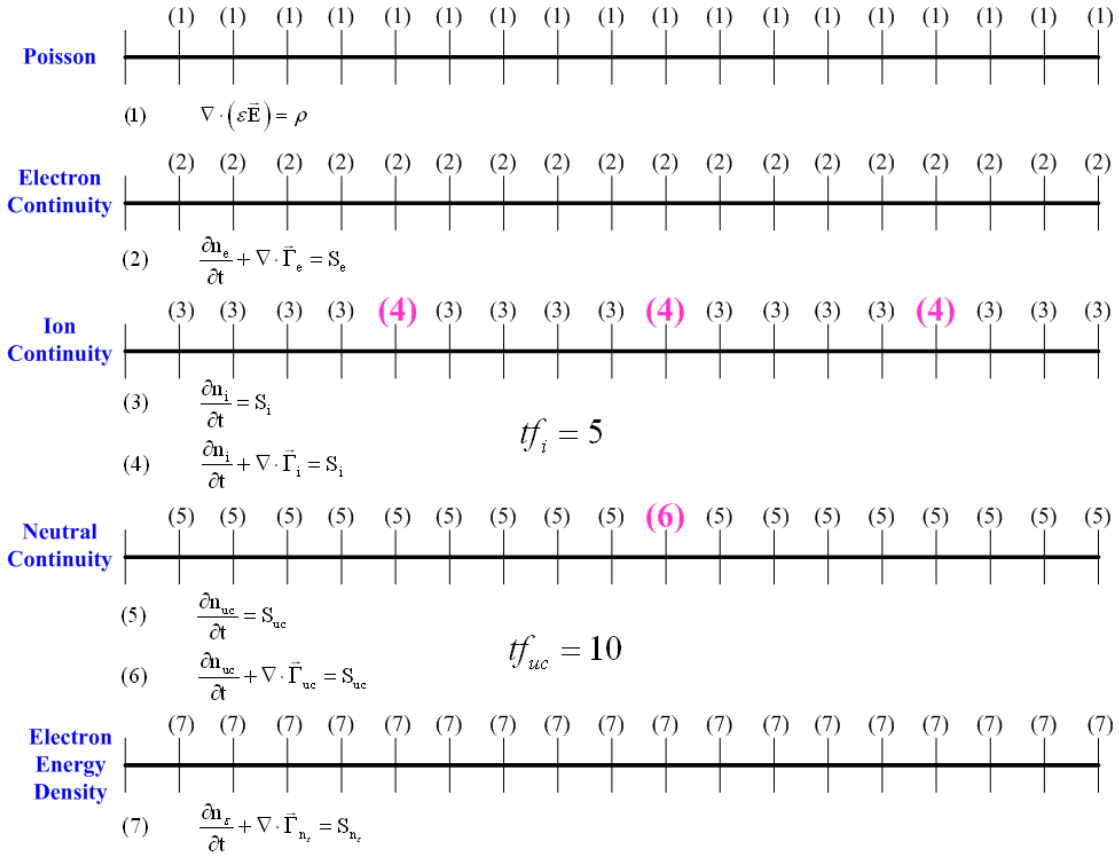

Fig. 2-4 Time sequence of the temporal multi-scale method

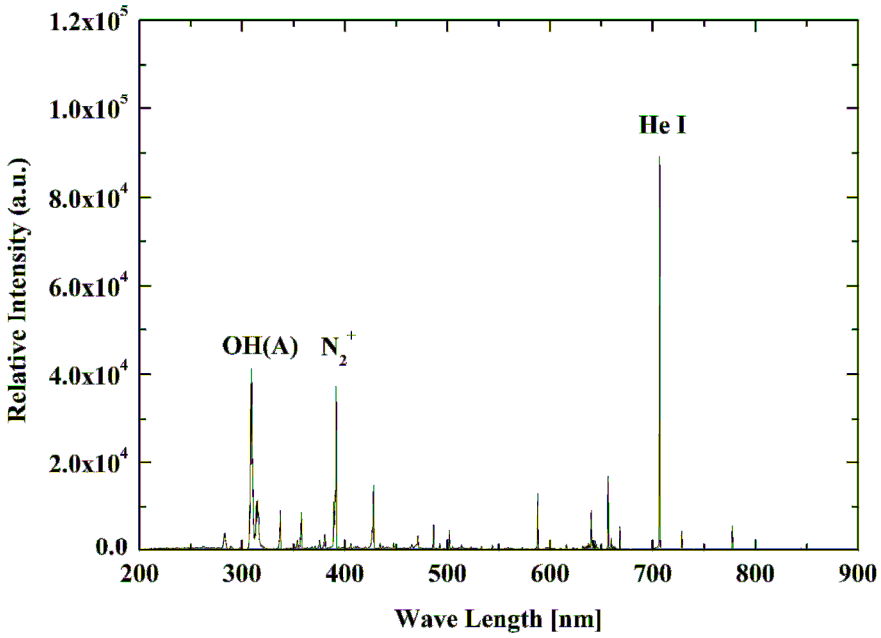

Fig. 3-1 Optical emission spectroscopy measurement of helium APDBDJ.

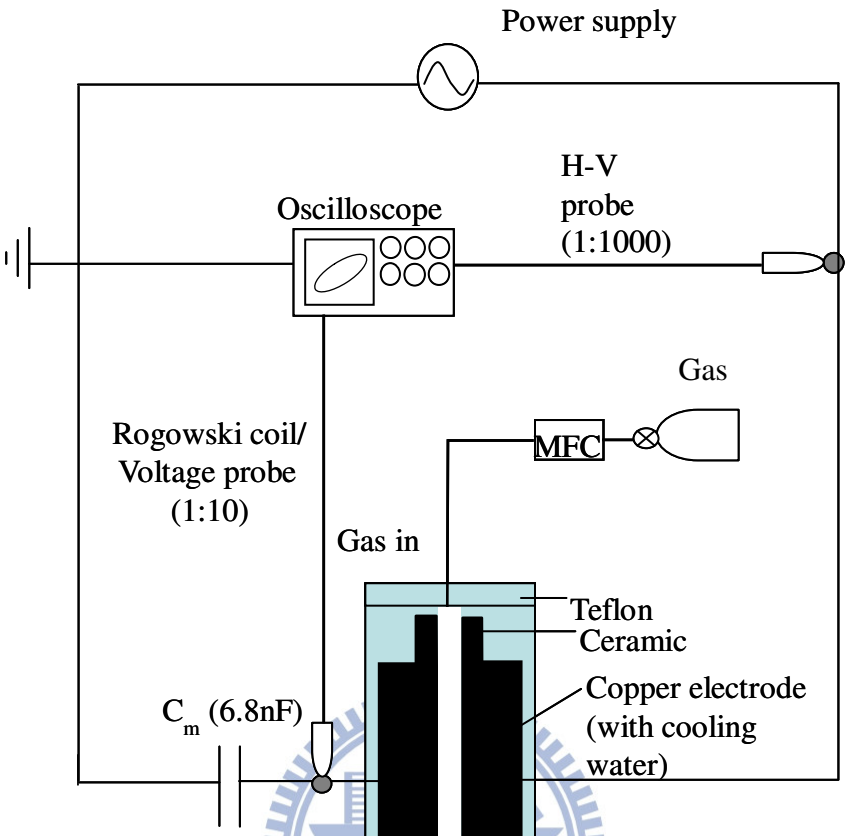

Fig. 3-2 Sketch of the planar helium APDBDJ system [39]

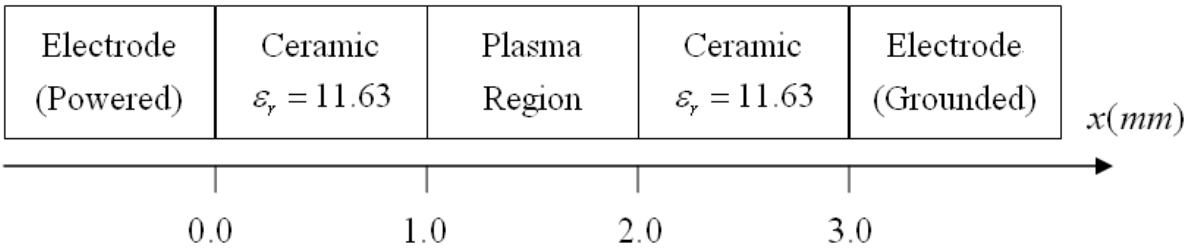

Fig. 3-3 Schematic diagram of the one-dimensional simulation model of a helium DBD.

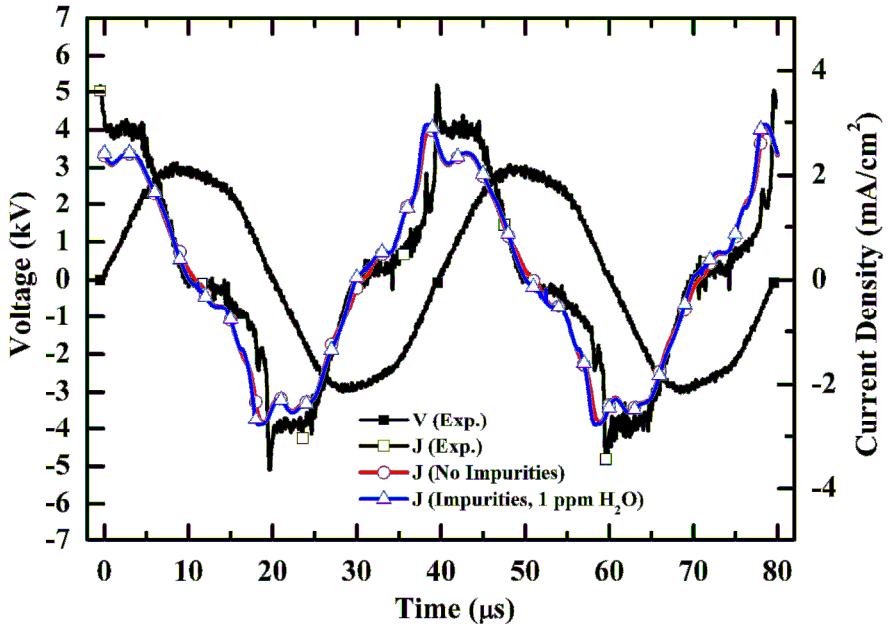

Fig. 3-4 Simulated and experimental discharge current densities for helium discharges with and without impurities driven by V_{pp} = 6.0 kV (peak-to-peak voltage). The frequency of power source is 25 kHz

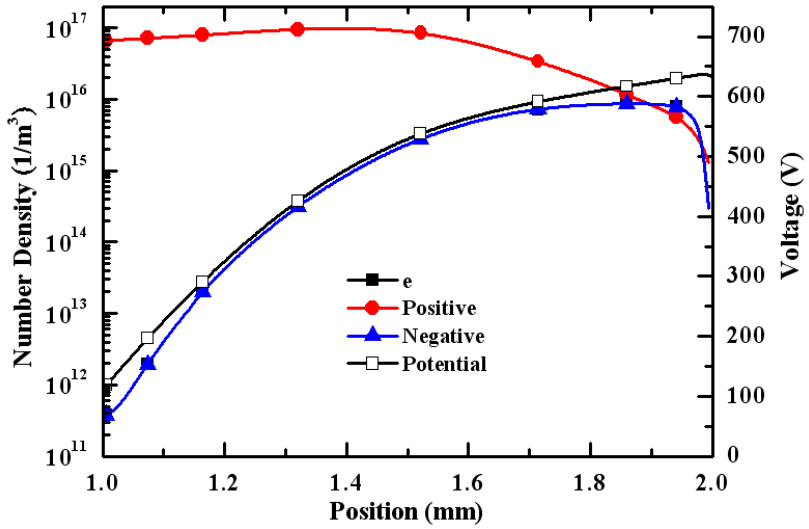

(a)

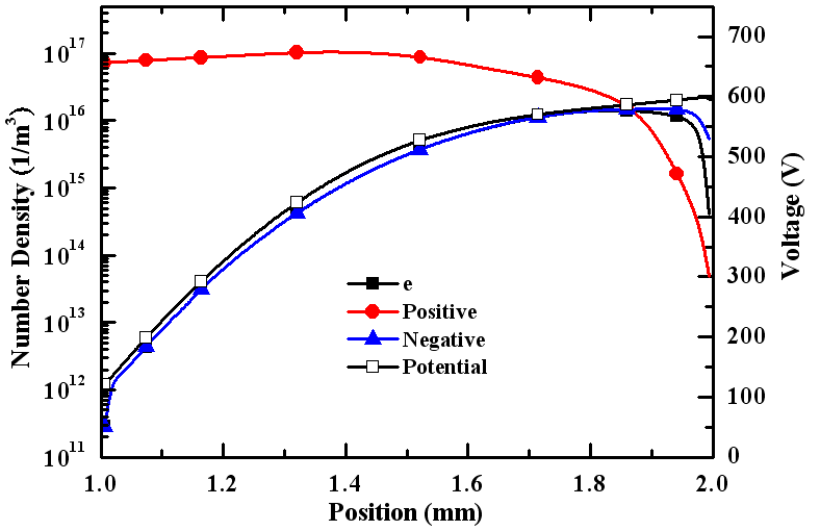

(b)

Fig. 3-5. Discharge structure at the instant of maximum current density. (a) Case without impurity; (b) Case with impurity (10 ppm O_2, 25 ppm N_2, and 1 ppm H_2O). The legend "Positive" represents the density of all species with positive charge, and the "Negative" represents the density of all species with negative charge.

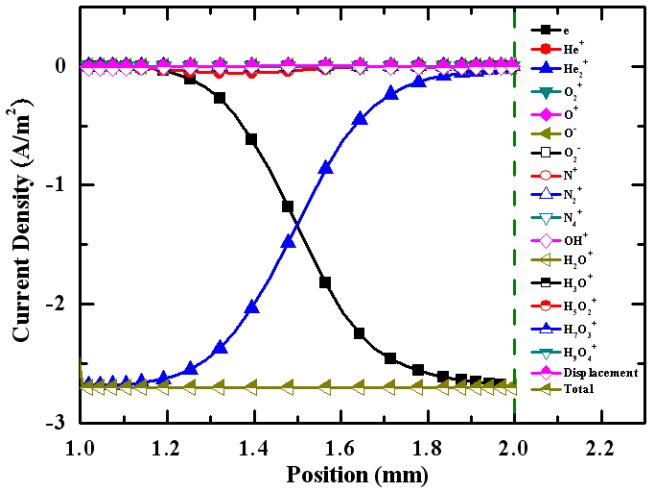

(a)

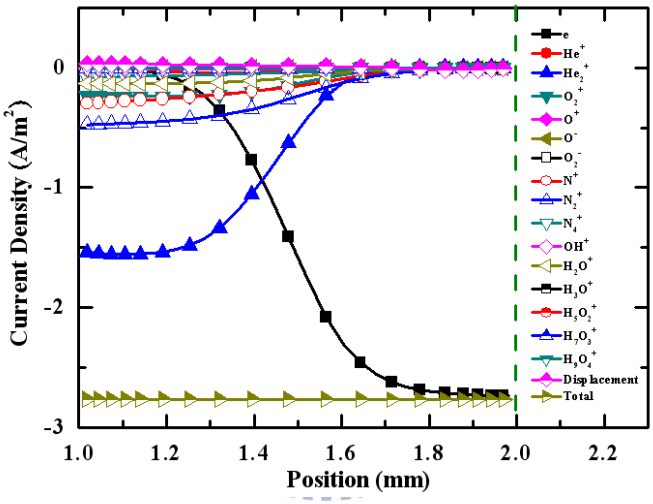

(b)

Fig. 3-6. The distribution of conduction (of each species), displacement, and total current density at the instant of maximum discharge current density for cases without (a) and with (b) impurities.

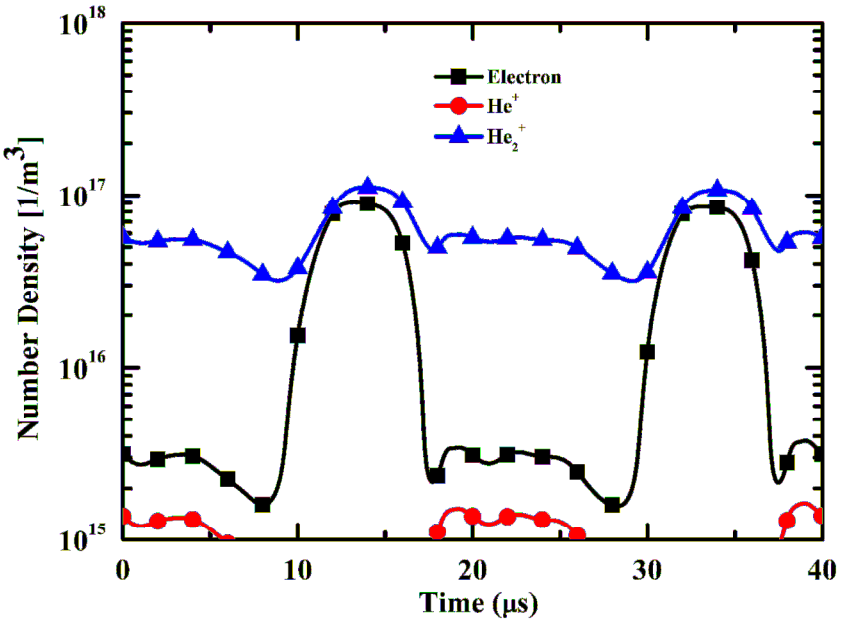

(a)

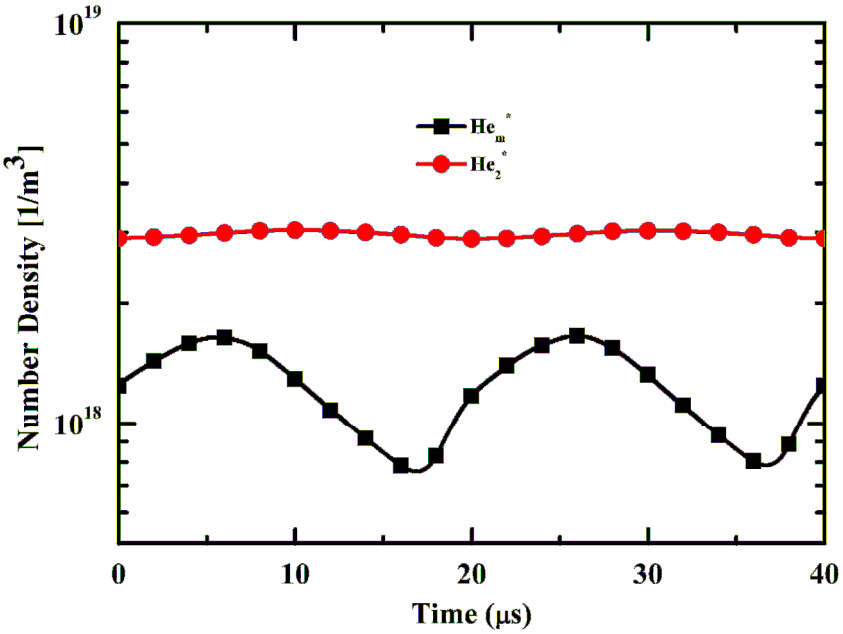

(b)

Fig. 3-7 Distributions of spatial-averaged number densities of helium discharge without impurity of abundant (a) charged species; (b) neutral species.

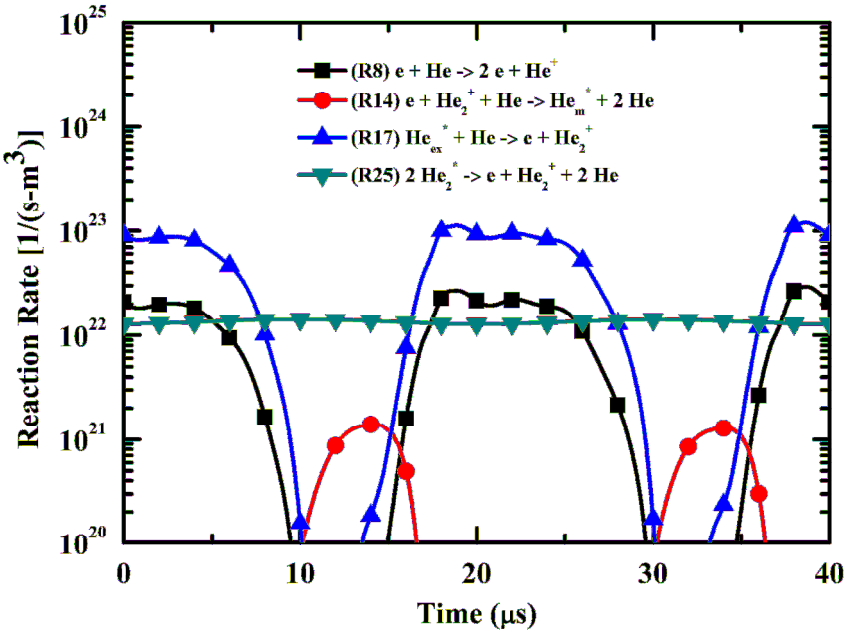

(a)

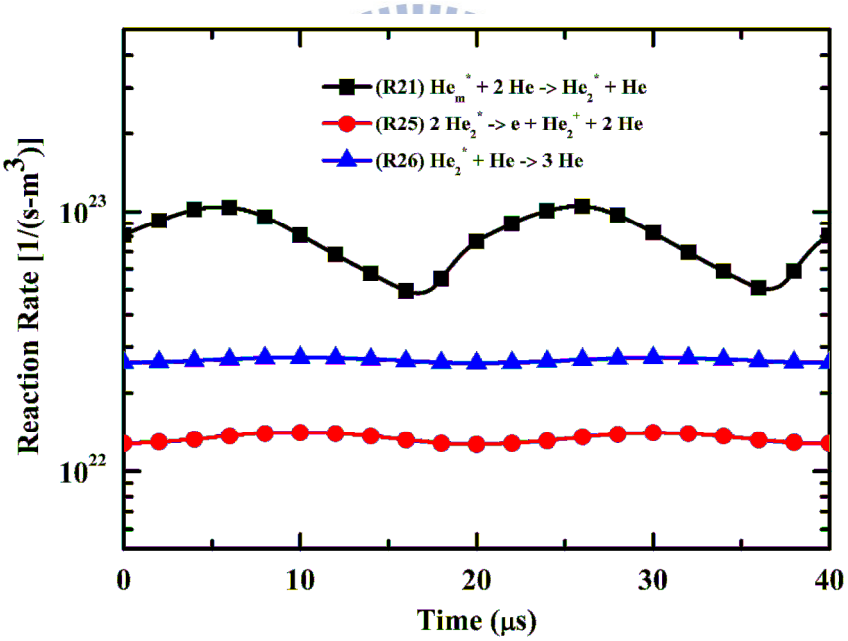

(b)

Fig. 3-8 Distributions of spatial-averaged reaction rates of important channels (a) electron; (b) He_2^*. The helium discharge contains no impurity.

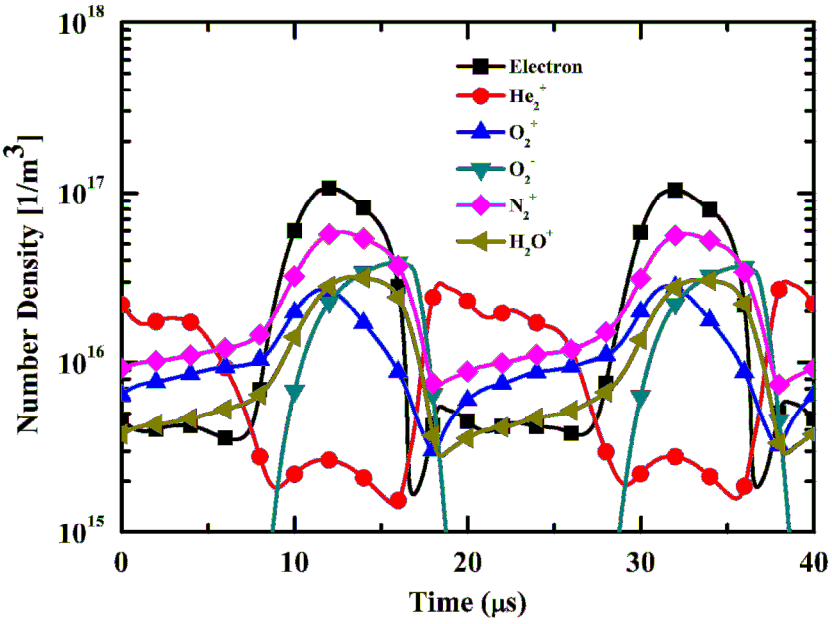

(a)

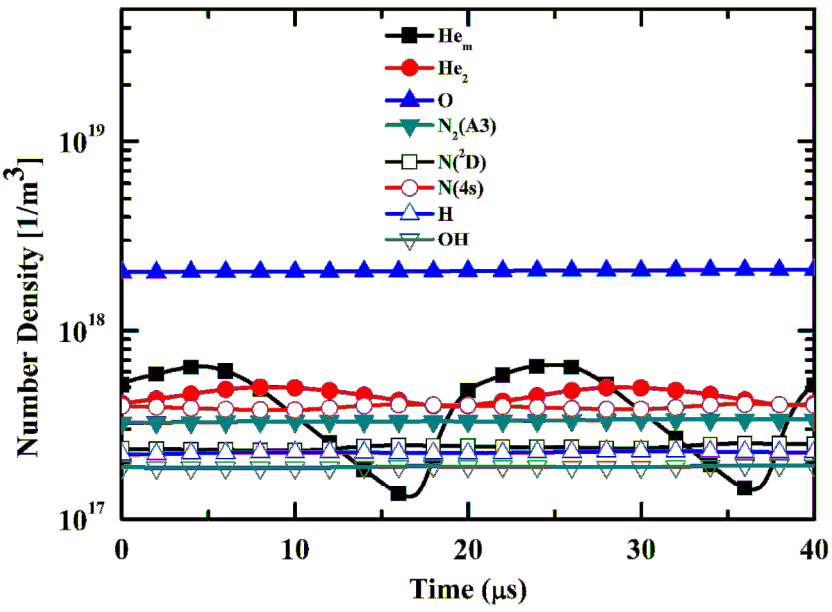

(b)

Fig. 3-9 Distributions of spatial-averaged number densities of helium discharge with impurities (10 ppm O_2, 25 ppm N_2, and 1 ppm H_2O) of abundant (a) charged species; (b) neutral species.

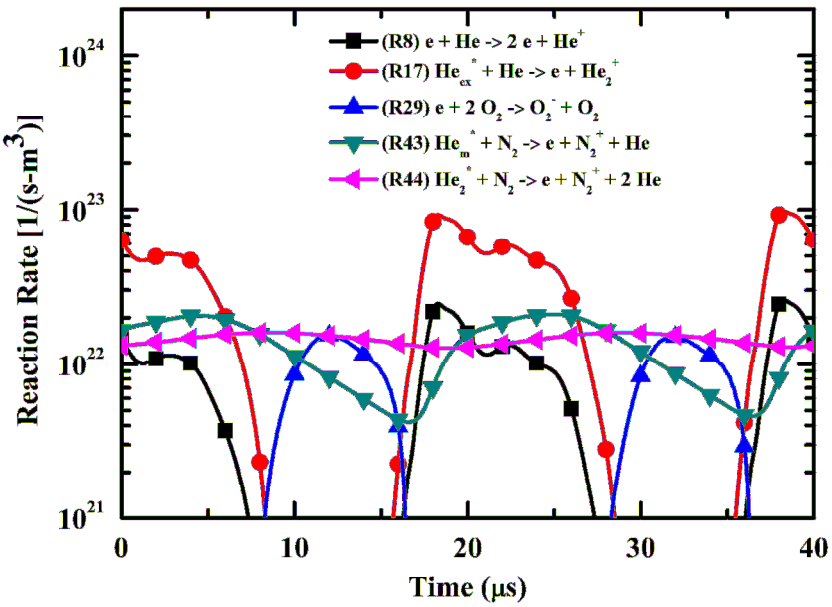
(R8) e + He -> 2 e + He+
(R17) Hex* + He -> e + He2+
(R29) e + 2 O2 -> O2- + O2
(R43) Hem* + N2 -> e + N2+ + He
(R44) He2* + N2 -> e + N2+ + 2 He
Reaction Rate [1/(s-m3)]
Time (μs)

(a)

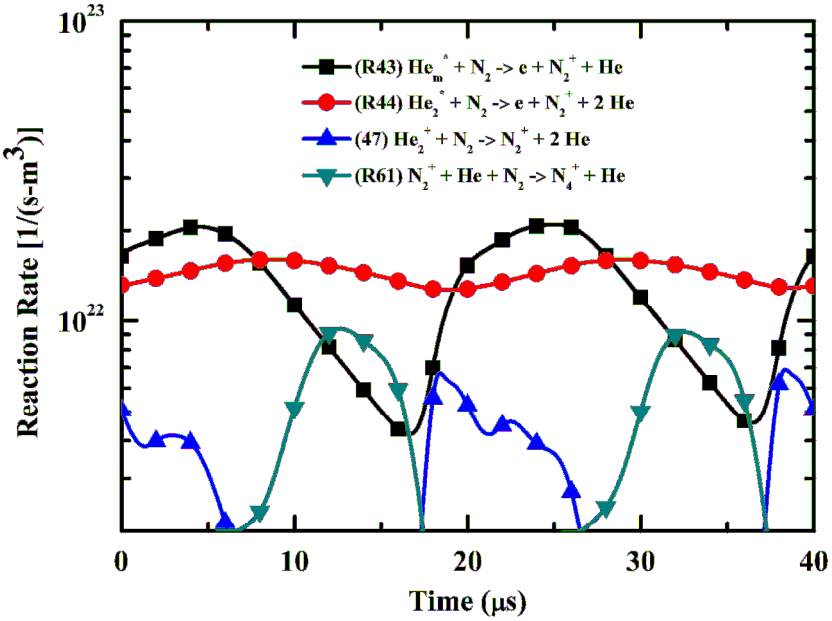
(R43) Hem* + N2 -> e + N2+ + He
(R44) He2* + N2 -> e + N2+ + 2 He
(47) He2+ + N2 -> N2+ + 2 He
(R61) N2+ + He + N2 -> N4+ + He
Reaction Rate [1/(s-m3)]
Time (μs)

(b)

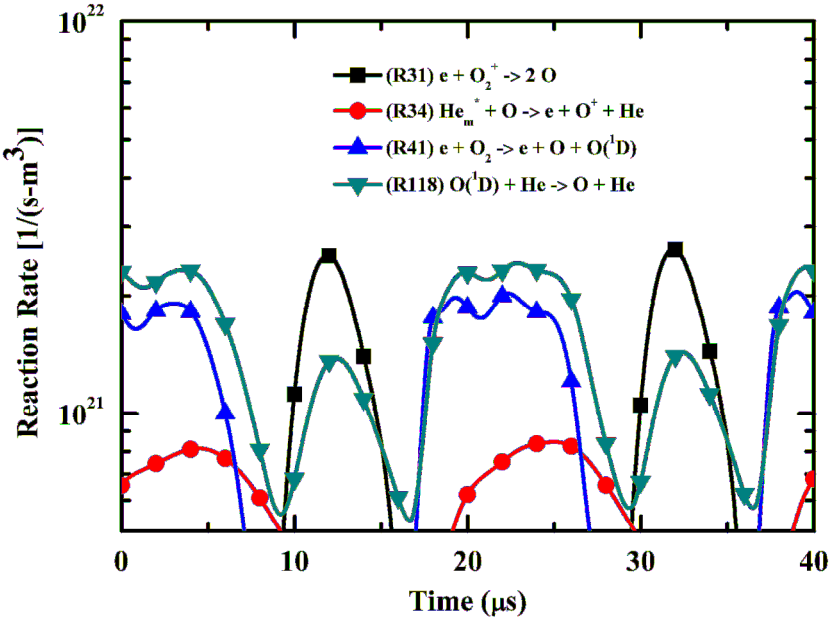

(c)

Fig. 3-10 Distributions of spatial-averaged reaction rates of important channels (a) electron; (b) N_2^+; (c) O. The helium discharge contains 10 ppm O_2, 25 ppm N_2, and 1 ppm H_2O.

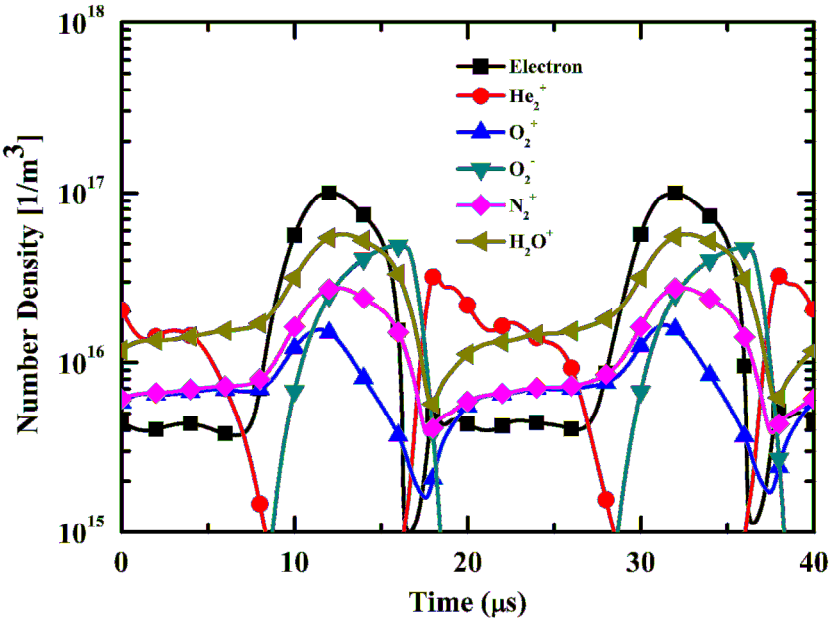

(a)

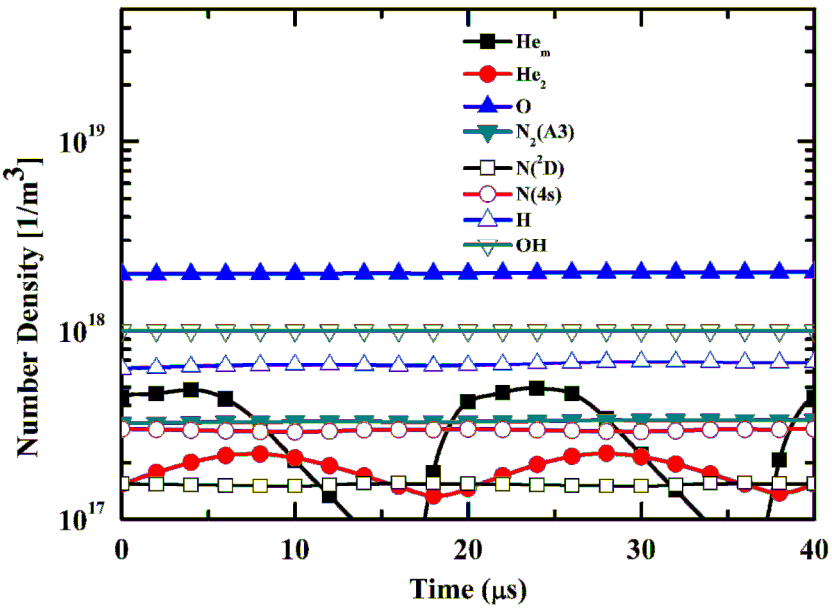

(b)

Fig. 3-11 Distributions of spatial-averaged number densities of helium discharge with impurities (10 ppm O_2, 25 ppm N_2, and 5 ppm H_2O) of abundant (a) charged species; (b) neutral species.

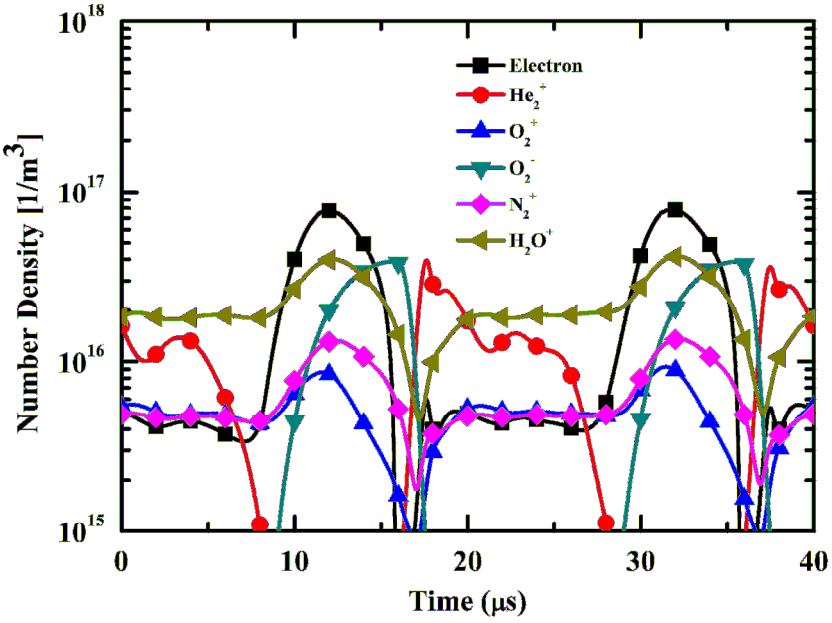

(a)

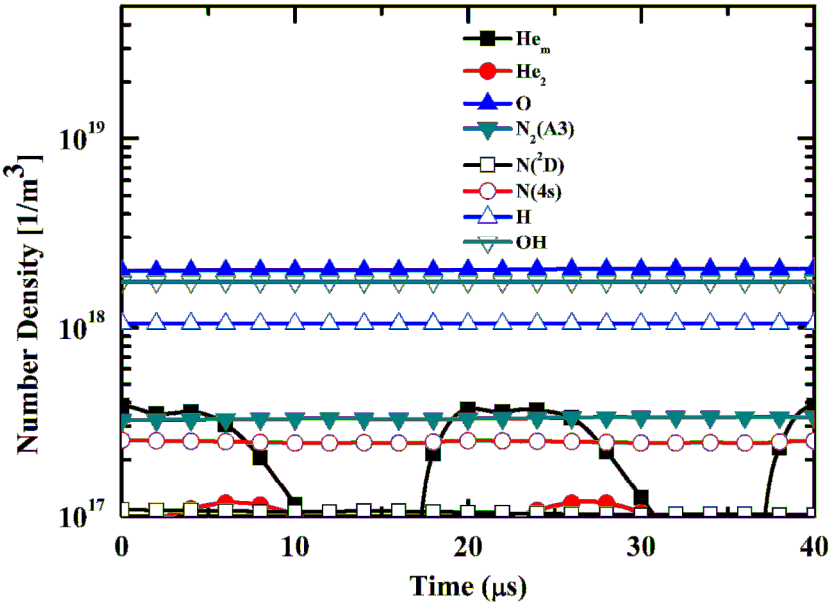

(b)

Fig. 3-12 Distributions of spatial-averaged number densities of helium discharge with impurities (10 ppm O_2, 25 ppm N_2, and 10 ppm H_2O) of abundant (a) charged species; (b) neutral species.

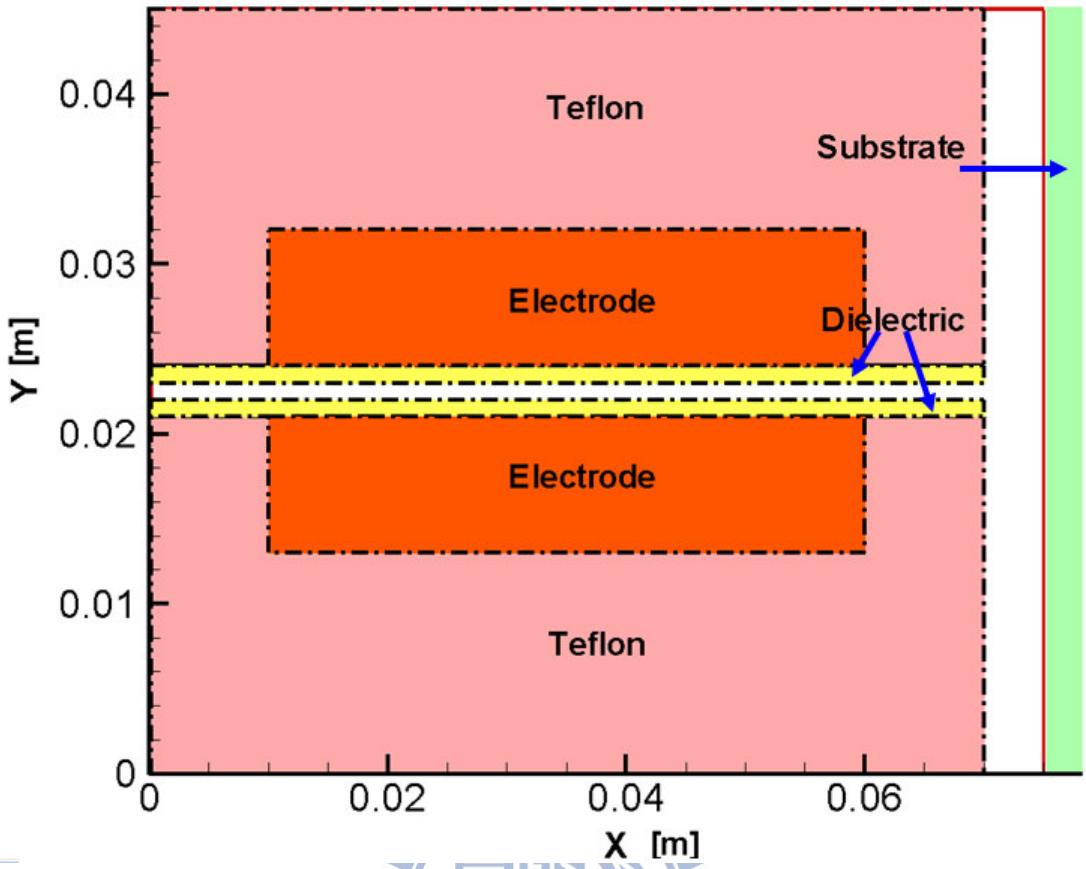

Fig. 4-1 Sketch of the simulation domain.

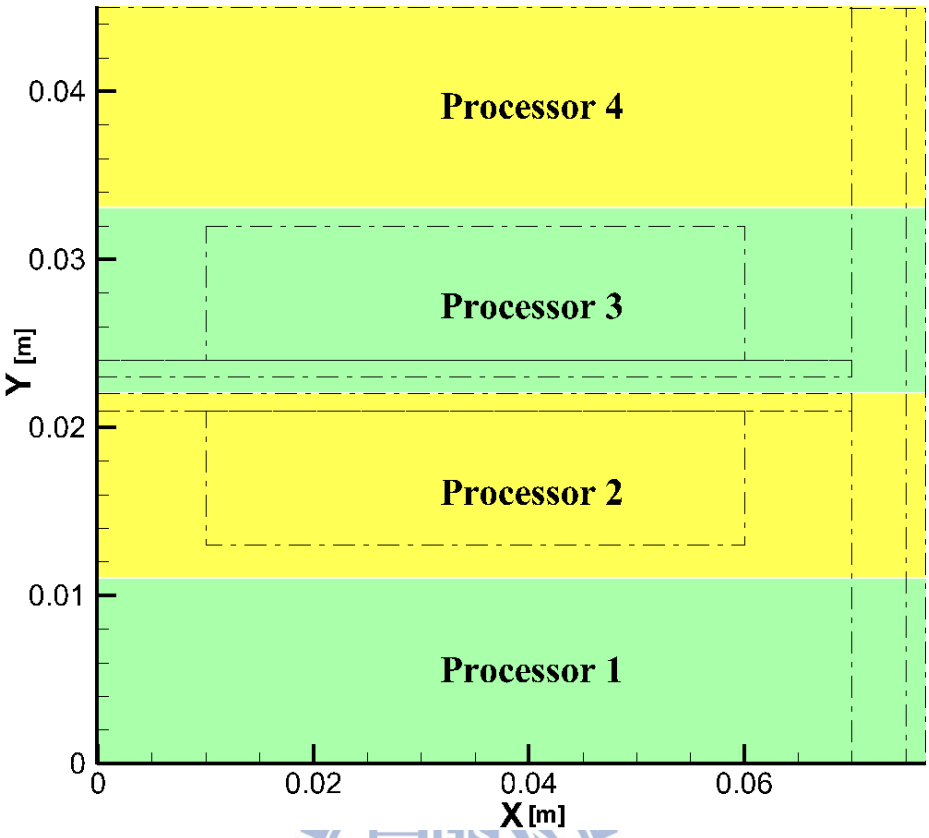

Fig. 4-2 The partition of computational domain.

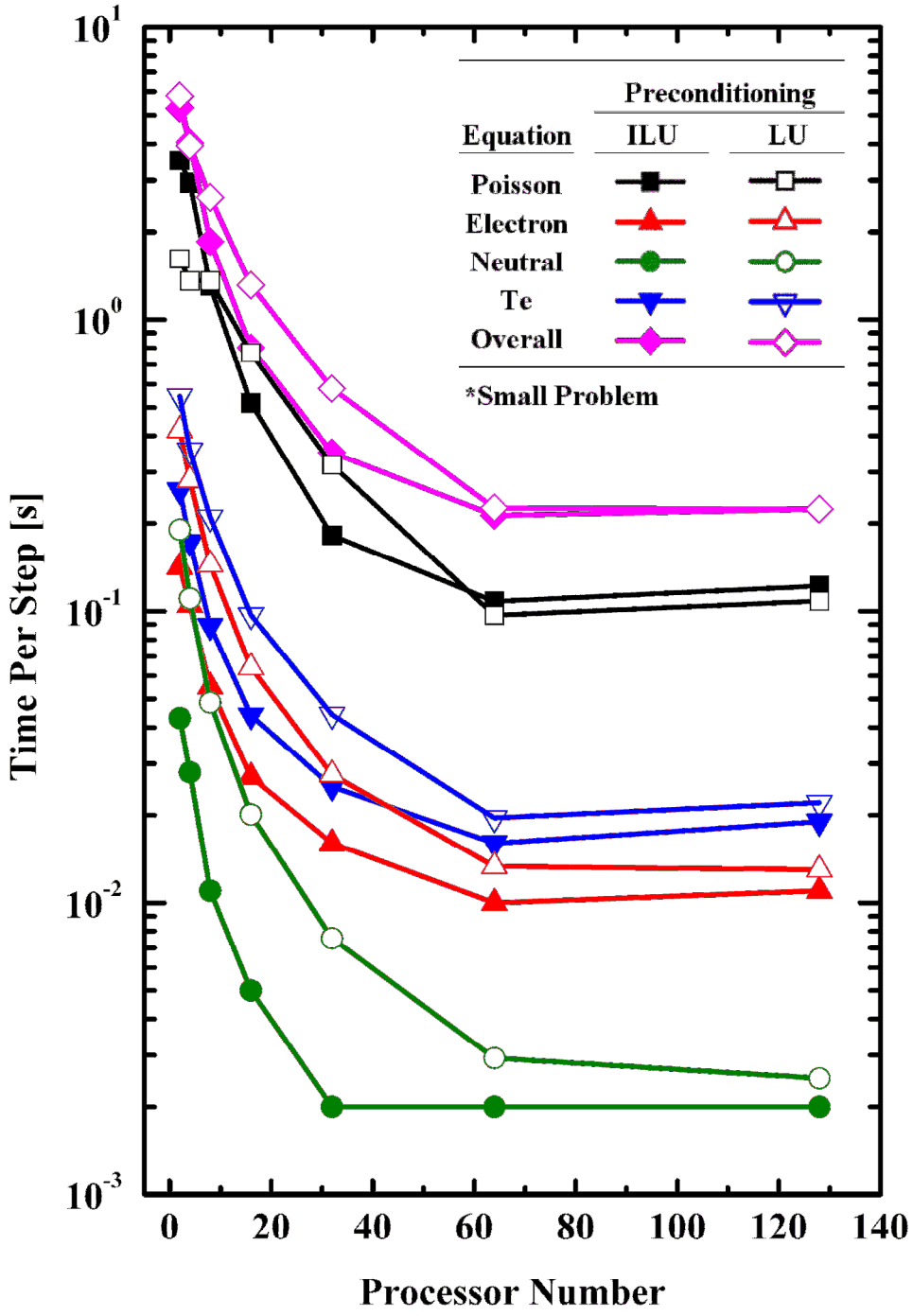

Fig. 4-3 Averaged time per time step of equations with sub-domain of ASM preconditioner solved by ILU and LU methods for small problem case (501 ×310 cells)

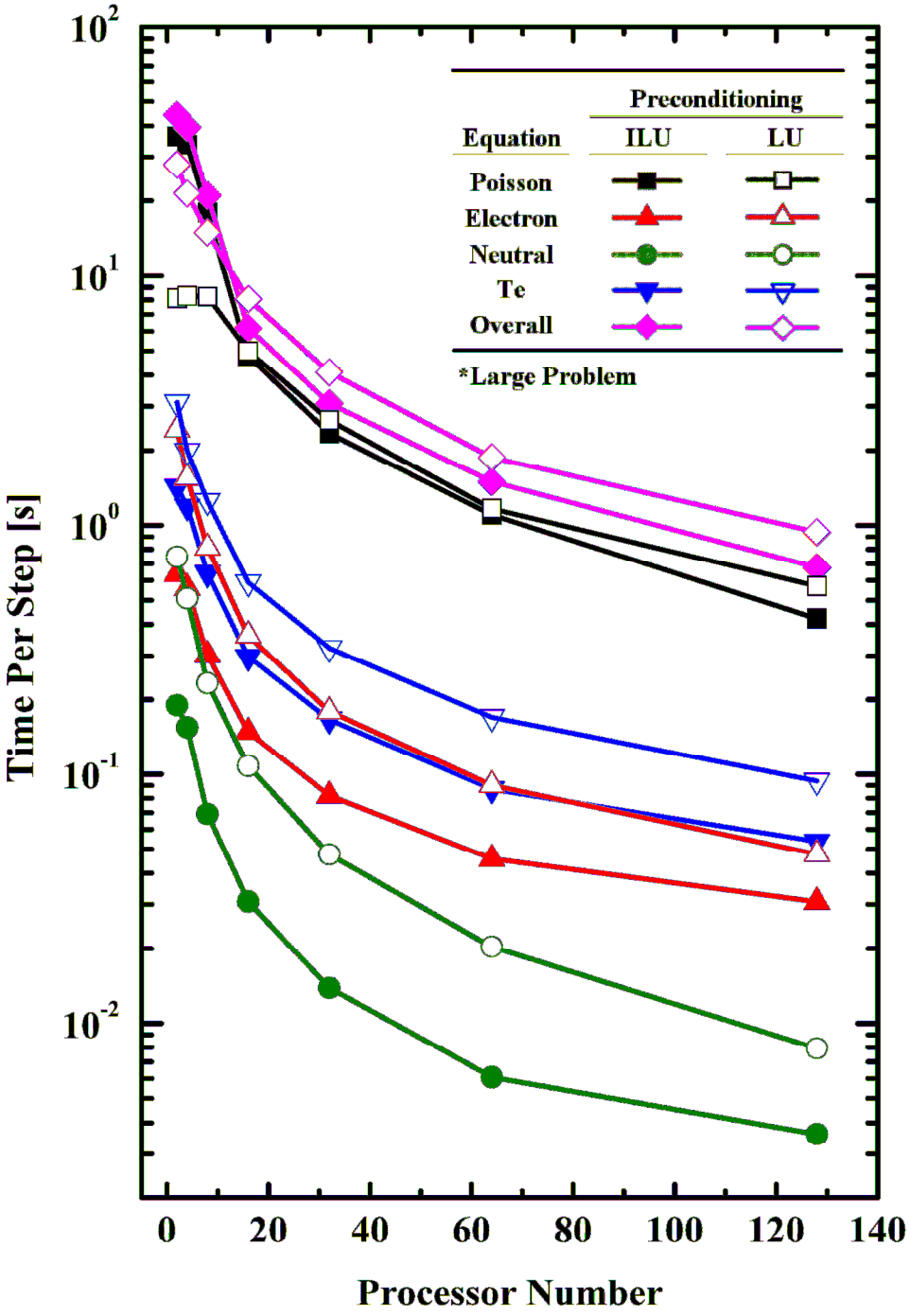

Fig. 4-4 Averaged time per time step of equations with sub-domain of ASM preconditioner solved by ILU and LU methods for large problem case (1001 ×620 cells).

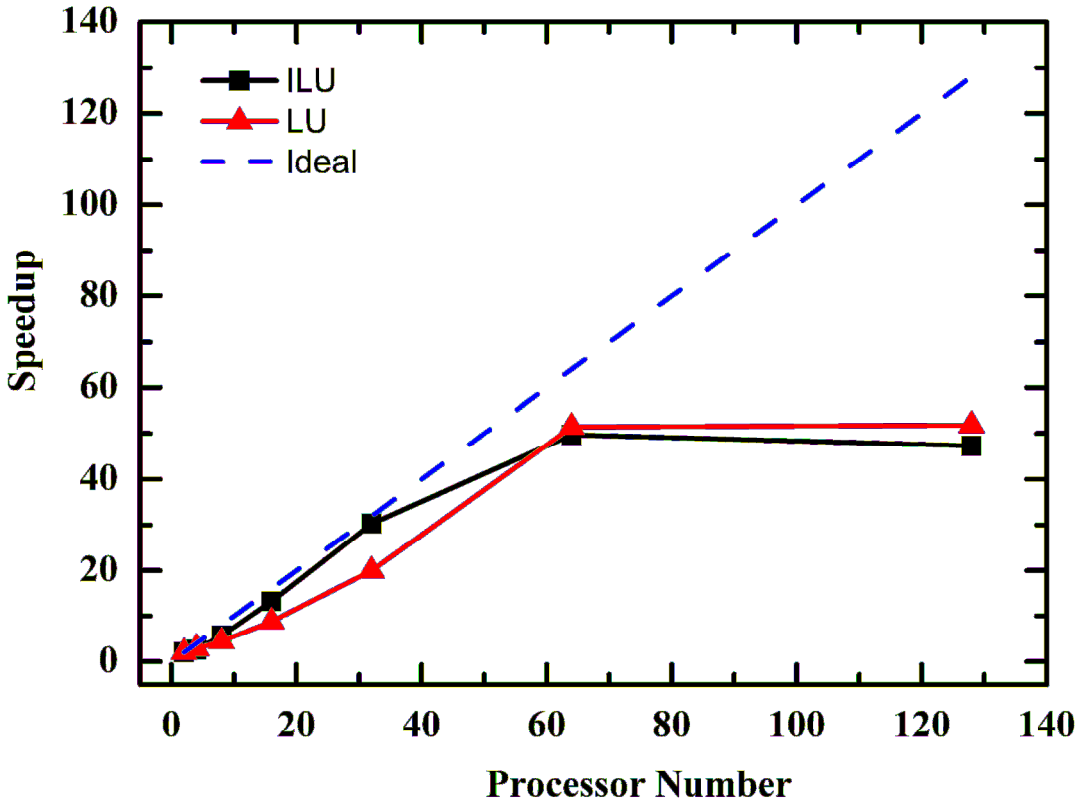

Fig. 4-5 Speedup of cases with sub-domain of ASM preconditioner solved by ILU and LU methods for small problem case (501 ×310 cells).

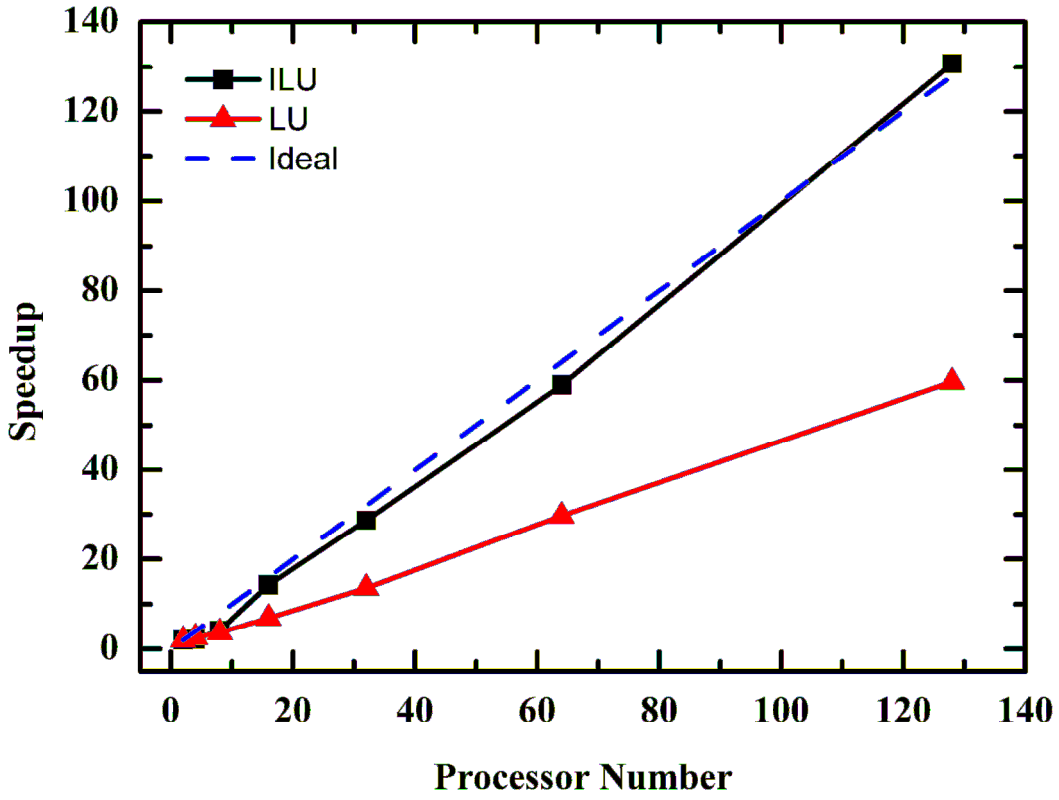

Fig. 4-6 Speedup of cases with sub-domain of ASM preconditioner solved by ILU and LU methods for large problem case (1001 ×620 cells).

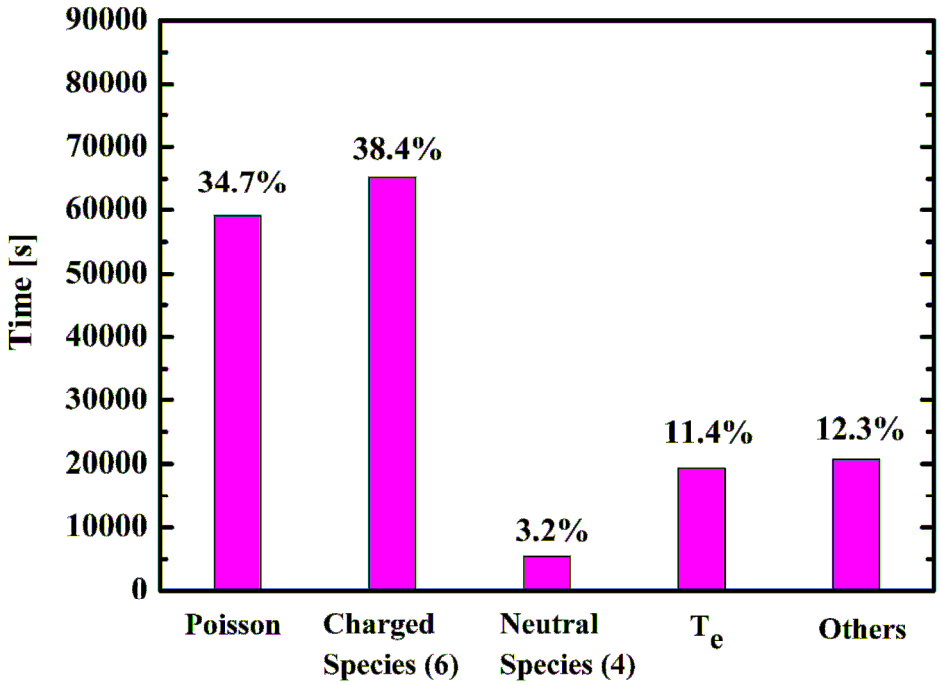

Fig. 4-7 Proportions of time consumed by different types of equations of the demonstration case (1001 ×620 cells). Note that "others" includes evaluation of transport properties and data communication among processors.

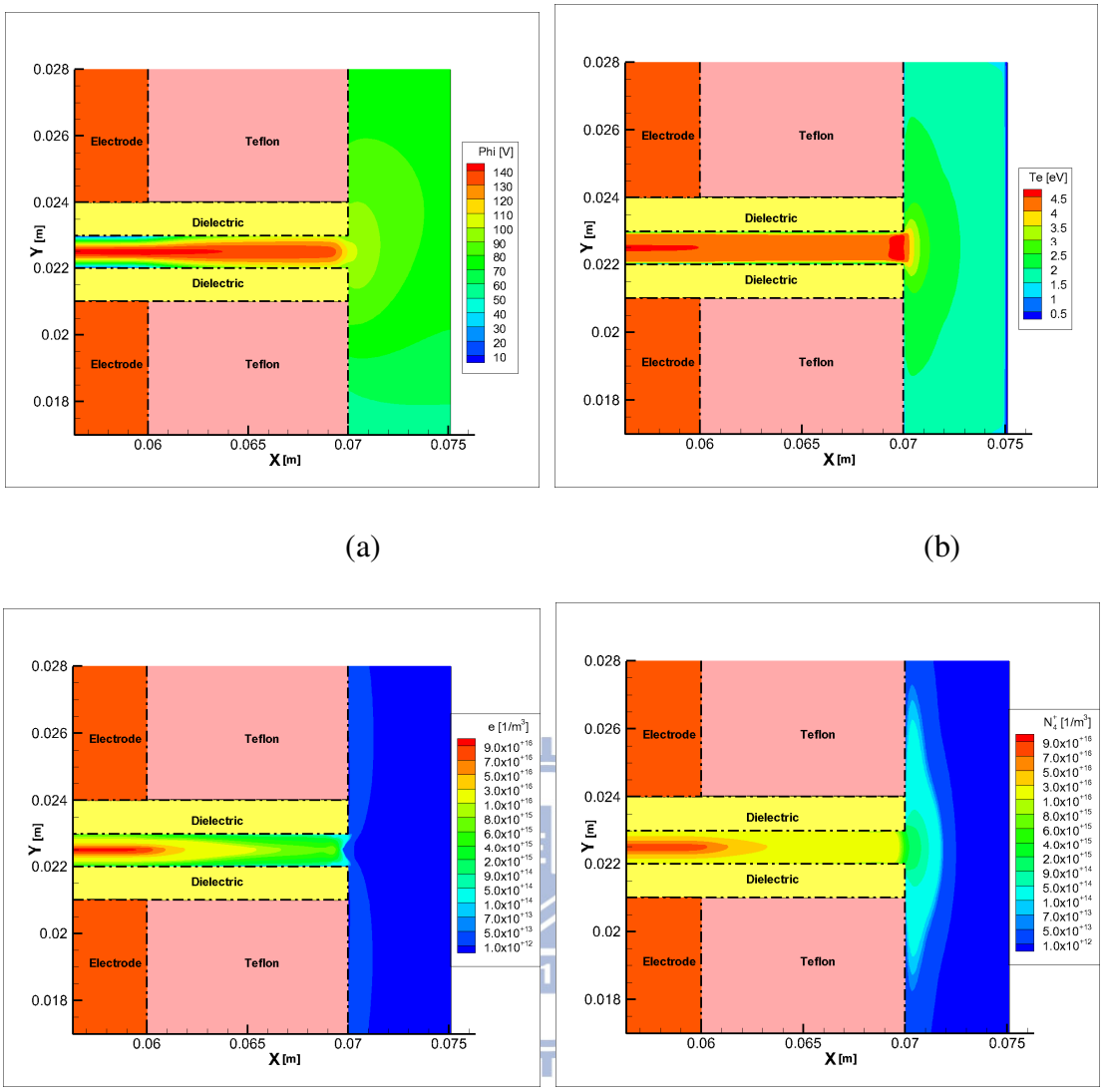

(a) (b)

(c) (d)

Fig. 4-8 Cycle-averaged spatial distributions of (a) potential (b) electron temperature (c) number density of electron (d) number density of N_4^+ in the 5th cycle.

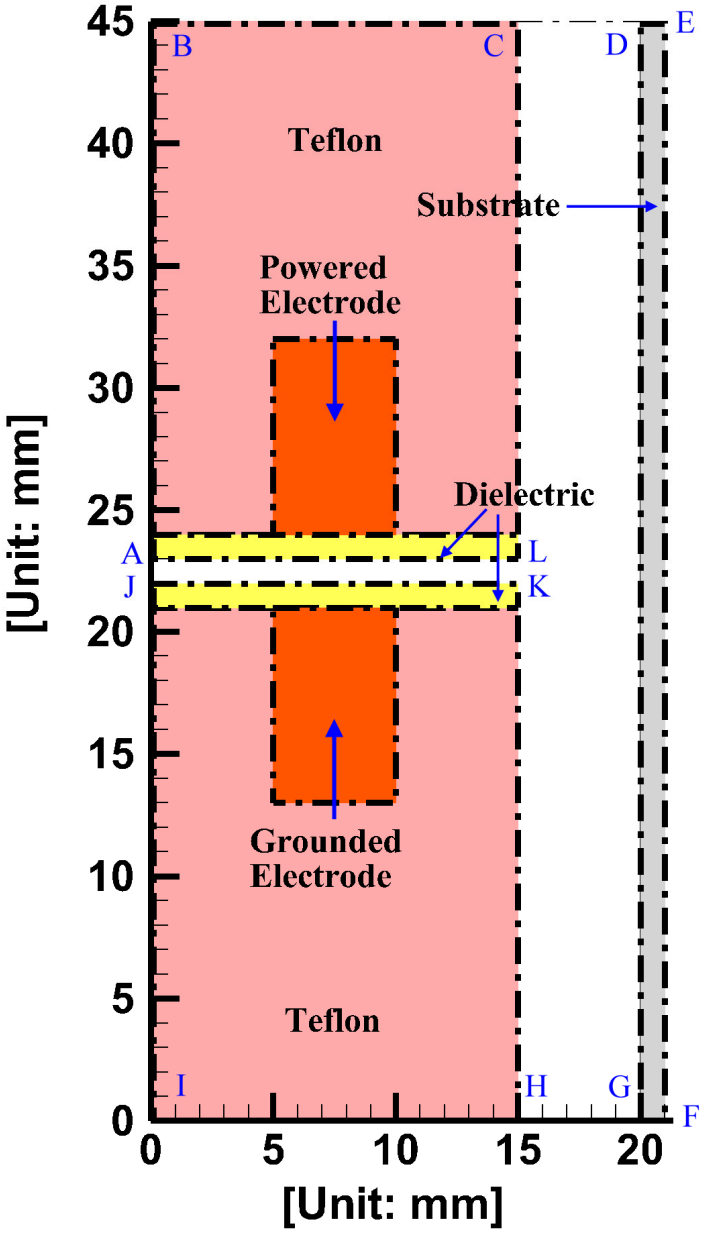

Fig. 5-1 Sketch of the computational domain

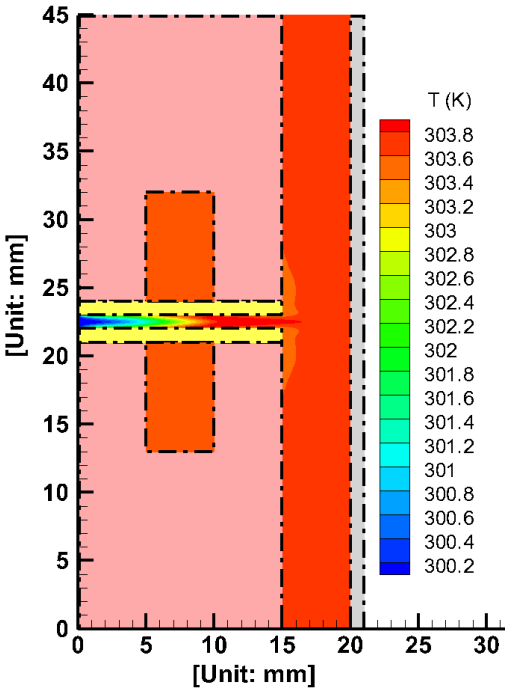

(a)

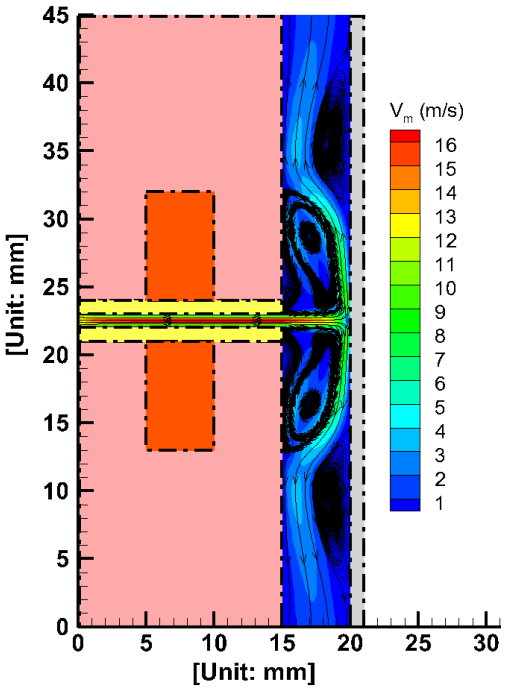

(b)

Fig. 5-2 The converged results of the GFM solver after three interactions with the PFM. (a) Temperature (b) The $V_m = \sqrt{u^2 + v^2}$ and the streamlines, where u and v are the velocity in the x and y direction respectively.

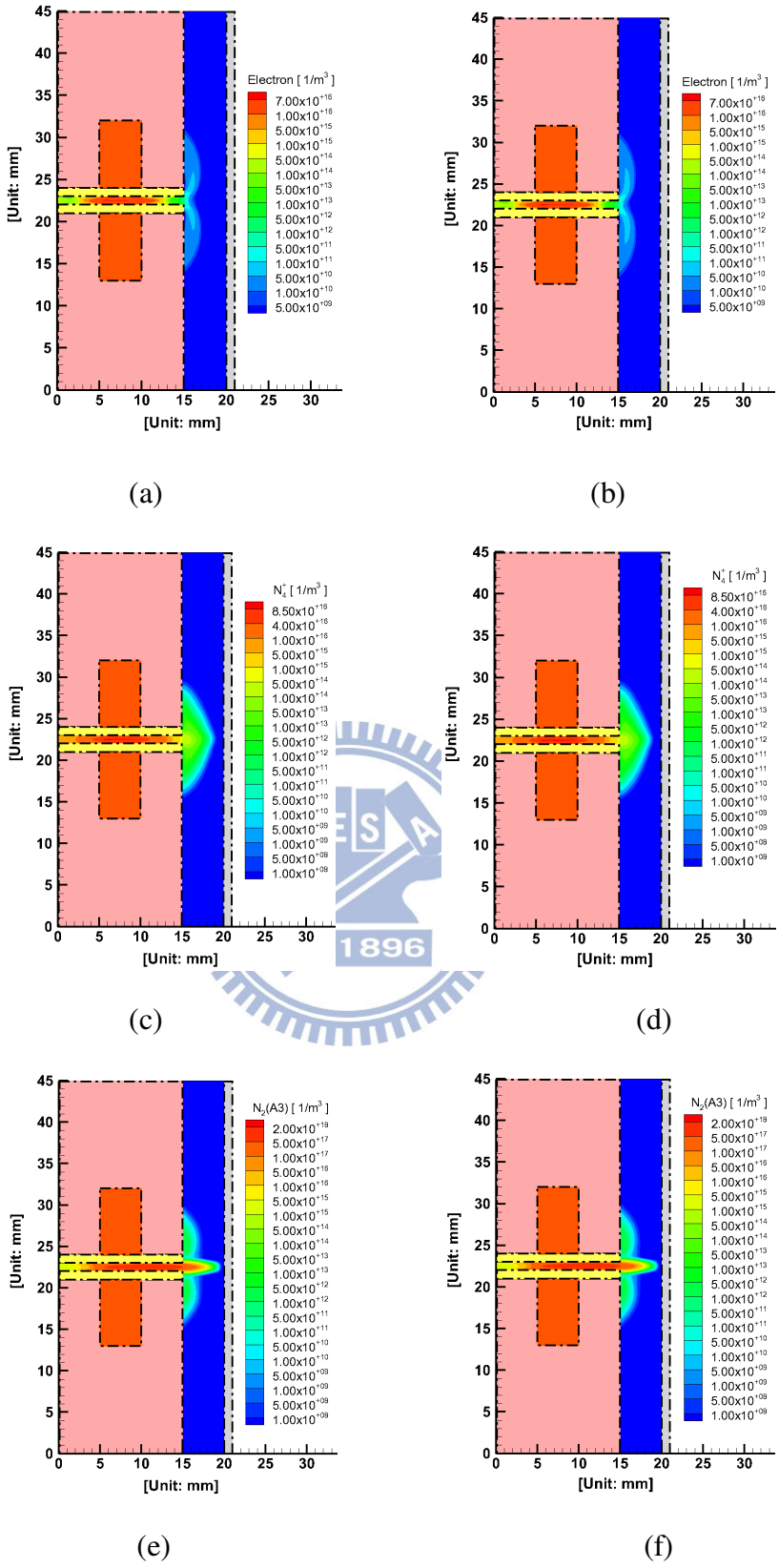

Fig. 5-3 The cycle-averaged number densities of species at 10th cycle simulated without (w/o) and with (w) the temporal multi-scale method (a) Electron (w/o), (b) Electron (w), (c) N_4^+ (w/o), (d) N_4^+ (w), (e) $N_2(A3)$ (w/o), (e) $N_2(A3)$ (w).

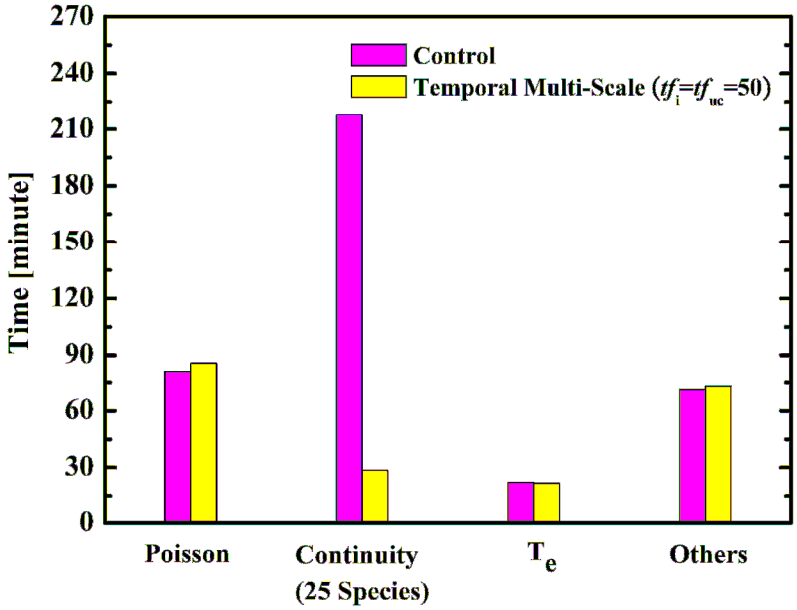

Fig. 5-4 Breakdown of runtime for solving equations and other computer operations in one cycle. Note that "Poisson", "Continuity", and "Te" represent the Poisson equation, species continuity equations, and the electron energy density equation respectively. The "Others" includes evaluation of transport properties and MPI transmission among processors.

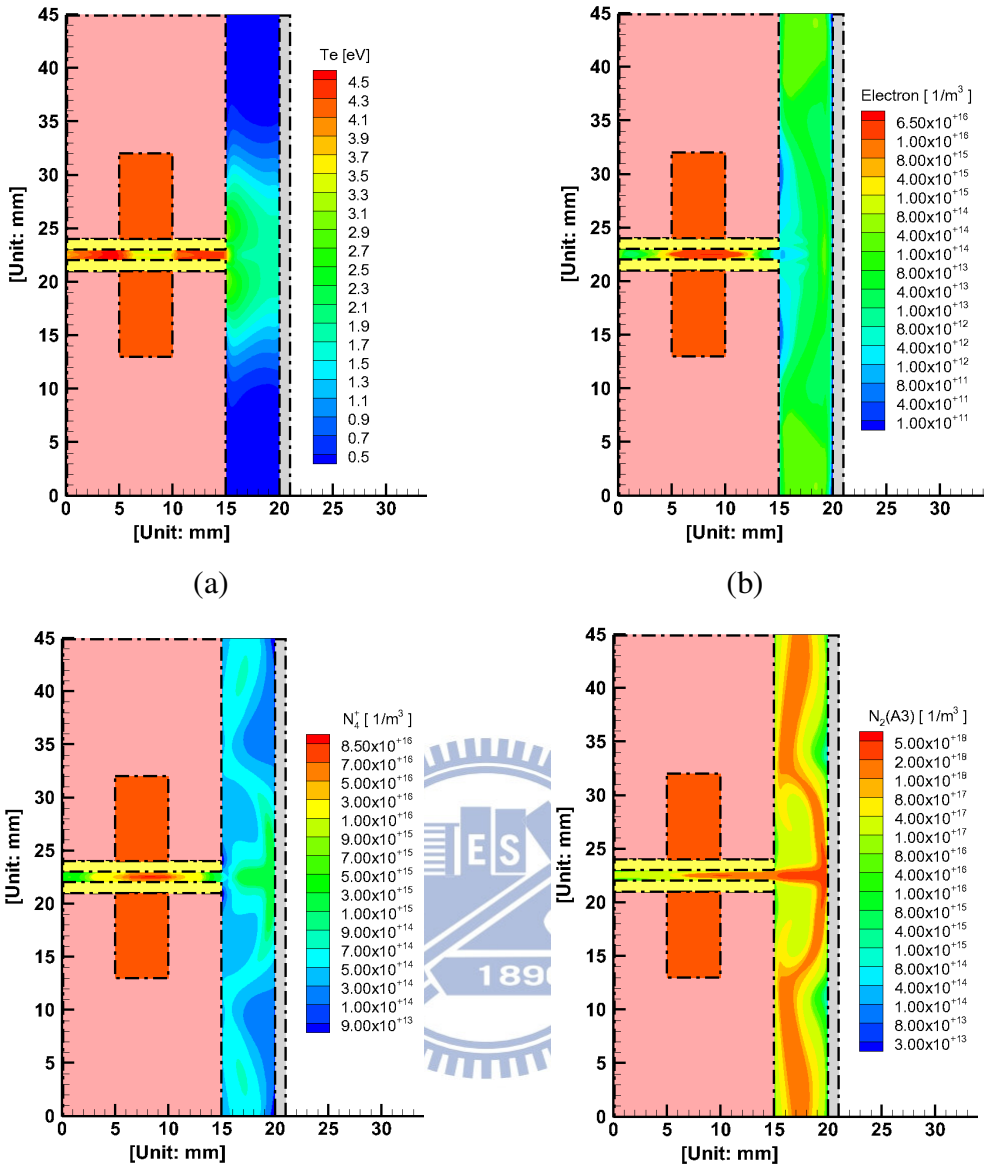

Fig. 5-5 Cycle-averaged spatial distributions of (a) electron temperature (Te), (b) number density of electron, (c) number density of N_4^+, (d) number density of $N_2(A3)$ at the 200th cycle.

Publication List of Kun-Mo Lin

Journal Papers：

"+" represents those papers related to my Ph. D. degree

+1. M. R. Smith, **K.-M. Lin**, C.-T. Hung, Y.-S. Chen, and J.-S. Wu*, "Development of an improved spatial reconstruction technique for the HLL method and its applications", Journal of Computational Physics, Vol. 230, pp. 477-493, 2011.

+2. M. R. Smith, C.-T. Hung, **K.-M. Lin**, J.-S. Wu*, and J.-P. Yu, "Development of a semi-implicit fluid modeling code using finite-volume method based on Cartesian grids," Computer Physics Communications, Vol. 182, pp. 170-172, 2011

+3. **K.-M. Lin**, C.-T. Hung, F.-N. Hwang, M. R. Smith, Y.-W. Yang, and J.-S. Wu, "Development of a Parallel Semi-Implicit Two-Dimensional Plasma Fluid Modeling Code Using Finite-Volume Method", Computer Physics Communication, 183 (2012), pp. 1225-1236.

+4. **K.-M. Lin**, M.-H. Hu, C.-T. Hung, J.-S. Wu, F.-N. Hwang, Y.-S. Chen, and G. Cheng, "A Parallel Hybrid Numerical Algorithm for Simulating Gas Flow and Gas Discharge of an Atmospheric-Pressure Plasma Jet", Computer Physics Communication, 2012 (submitted).

5. F.-L. Li, **K.-M. Lin**, Y.-W. Yang, C.-T. Hung, J.-S. Wu, and J.-P. Yu, "Numerical Investigation of a Parallel-Plate Atmospheric-Pressure Nitrogen/Ammonia Dielectric Barrier Discharge," Plasma Chemistry and Plasma Processing, Vol. 31, Number 3, pp. 547-564, 2012.

6. F.-L Li, **K.-M. Lin**, Y.-W. Yang, C.-T. Hung, J.-S. Wu* and J.-P. Yu, "Fluid Modeling of Planar Atmospheric-Pressure Nitrogen Dielectric Barrier Discharge Mixed with Ammonia," Advanced Science Letters, 2012 (submitted).

7. K.-W. Cheng, C.-T. Hung, **K.-M. Lin**, Y.-M. Chiu, J.-S. Wu* and J.-P. Yu, "Fluid Modeling of a Nitrogen Atmospheric-Pressure Planar Dielectric Barrier Discharge Driven by a Realistic Distorted Sinusoidal AC Power Source," Japan Journal of Applied Physics, 2012 (under revision).
8. K-W. Cheng, C.-T. Hung, **K.-M. Lin**, Y.-M. Chiu and J.-S. Wu*, "One-dimensional Fluid Modeling of a Nitrogen/Oxygen Atmospheric-Pressure Planar Dielectric Barrier Discharge," Journal of Physics D – Applied Physics, 2012 (submitted).

International Conference Papers：

1. M. R. Smith, C.-T. Hung, **K.-M. Lin**, J.-S. Wu, and J.-P. Yu, "Development of a semi-implicit fluid modeling code using finite-volume method based on Cartesian grids," Conference on Computational Physics (CCP) 2009, Kaohsiung, Taiwan, December 15-19, 2009
2. C.-T. Hung, M.-H. Hu, Y.-M. Chiu, **K.-M Lin**, Y.-C. Wang, and J.-S. Wu, "Non-Thermal Plasma Simulation Using Parallel Fluid Modeling Code," HPC-Asia 2009, March 2-5 (2009), Kaohsiung, Taiwan
3. **K.-M. Lin**, M. R. Smith, and J.-S. Wu*, "Development of a large scale parallel fluid modeling code using finite-volume method based on Cartesian grids", Conference on Computational Physics (CCP) 2009, Kaohsiung, Taiwan, December 15-19, 2009.
4. **K.-M Lin**, C.-T. Hung, M. R. Smith, and J.-S. Wu*, "One-dimensional Fluid Modeling of Helium/Oxygen Gas Discharges Driven by a Nearly Sinusoidal AC Power Source", 7th International Conference on Flow Dynamics, Sendai, Japan, November 1-3, 2010.
5. J.-S. Wu*, **K.-M. Lin**, M.-H. Hu, C.-T. Hung and Y.M. Chiu, "Progress in Developing Fluid Modeling and Gas Flow Simulation Codes for General

Gas-Discharge Application," 2011 American Vacuum Society International Plasma Workshop, Taipei, Taiwan, March 22-25, 2011

6. **K.-M. Lin**, M.-H. Hu, C.-T. Hung, and J.-S. Wu*, "Numerical Investigation of Atmospheric Pressure Plasma Jet Using Helium Discharge Driven by a Radio-Frequency Power Source", American Vacuum Society (AVS) International Plasma Workshop, Taipei, Taiwan, March 22-25, 2011
7. **K.-M. Lin**, M.-H. Hu, C.-T. Hung and J.-S. Wu*, "Development of Parallel Hybrid Simulation Tools for Modeling Atmospheric-Pressure Gas Discharges," 8th EU-Japan Joint Symposium on Plasma Processing (JSPP2012), Nara, Japan, January 16-18, 2012.
8. **K.-M. Lin**, M.-H. Hu, C.-T. Hung, and J.-S. Wu, "Development of a Parallel 2-D Hybrid Gas Flow and Plasma Fluid Modeling Algorithm and Its Application in Atmospheric-Pressure Plasma Jets", The 7th Asia-Pacific International Symposium on the Basics and Applications of Plasma Technology, Taiwan, April 14-16, 2012

Domestic Conference Papers:

1. A. Aliat, **K.-M. Lin**, M.-H. Hu, and J.-S. Wu, "Numerical Investigation of an Anode Supported Intermediate Temperature Solid Oxide Button Fuel Cell by Considering Feed Tubes Positioning", 2010 CFD Taiwan, Jhongli, July, 2010
2. C.-T. Hung, **K.-M. Lin**, Y.-M. Chiu, F.-N. Hwang, and J.-S. Wu*, "Parallel Fluid Modeling of Plasma-Enhanced Chemical Vapor Deposition for Amorphous Silicon (a-Si) Thin Film Growth," 18th Computational Fluid Dynamics Conference in Taiwan, Yilan, Taiwan, August 3-5,
3. **K.-M. Lin**, C.-T. Hung, J.-P. Yu, F.-N. Hwang, M. R. Smith, Y.-W. Yang and J.- S. Wu*, "Development and Validation of a Parallel Semi-Implicit Two-Dimensional

Plasma Fluid Modeling Code Using Finite-Volume Method," 18th Computational Fluid Dynamics Conference in Taiwan, Yilan, Taiwan, August 3-5, 2011